Chaotic Hamiltonian Ratchets with Cold Atoms

by

Nicolas Hutchings

September 2003

A thesis submitted to

THE UNIVERSITY OF LONDON

for the degree of

DOCTOR OF PHILOSOPHY

ProQuest LLC
789 East Eisenhower Parkway
P.O. Box 1346
Ann Arbor, MI 48106-1346

Abstract

Currently there is a great amount of scientific research directed at ratchet devices and mechanisms. Initially stimulated by a need to understand biological systems, the field has widened to encompass mesoscopic and atomic physics as well as quantum effects. The great majority of this effort has been directed at systems which include noise (Brownian ratchets). Comparatively little work has been undertaken on deterministic ratchets (i.e. with no noise but possibly including dissipation). Prior to our work there had only been two studies of Hamiltonian ratchets (no noise or dissipation) which concluded that only mixed-phase space mechanisms were feasible. However, the work in this thesis proposes a new fully chaotic, noise-free, Hamiltonian ratchet. This ratchet system is studied in both the quantum and classical regimes and is found to produce, reversible, non-zero currents for well chosen parameter values.

The ratchet mechanism proposed in this thesis is has now been implemented experimentally with ultra-cold cesium atoms in a pulsed optical lattice. Optimum system parameters are suggested to produce the best experimental signature for the ratchet. The work presented here has inspired further experimental work for the specific Hamiltonian of the system.

Contents

List of Figures

List of Tables

Acknowledgements

The completion of this thesis would not have been possible without the valuable guidance of my supervisor T. Monteiro. I would also like to thank my collaborators P. Dando, T. Jonckheere and M. Isherwood for their many helpful discussions. Thanks also to Phil Jones for very helpful advice regarding my thesis. Financial support is gratefully acknowledged from the EPSRC.

On a personal note, unending thanks to my parents for all their love, encouragement and support. Also, thank you Ozzy for all your patience and understanding. To my *family of choice*, I hope you all enjoy reading this. Finally, Skid, CU!

Chapter 1

Introduction

The last few years have seen enormous progress in the areas of cold atom physics and atom optics. Nobel prizes were awarded in 1997 and 2001 for laser-cooling of atoms and the experimental implementation of Bose-Einstein condensation.

There is much current interest in atom optics techniques to coherently manipulate the transport of atoms. Inspired by recent experimental developments using lasers and optical lattices, in this thesis a new type of ratchet is presented: in the past ratchets were not associated with coherent transport since most research was in noisy and dissipative ratchets. The level of control now possible over trapped, ultra-cold, atoms makes it possible for these atoms to generate ratchet transport when the correct symmetries are broken. Here, a system which fulfils these symmetry requirements, as well as having a new, generic, ratchet mechanism is presented and analysed (both classically and quantum mechanically). A full parameter range is explored for both the classical and quantum system with optimum ratchet parameters suggested for both regimes. This work is believed to be of importance as the system proposed is fully chaotic, noise free, quantum enhanced and experimentally realisable. As such, the model, or models of the same type, should provide ground for much future research and offer potential for use in optical devices. It should also be noted that previously noise free Hamiltonian ratchets have only been shown to exist in the regime of mixed phase space. A very brief overview of the contents of each chapter is now given.

Chapter 2: Quantum Chaos and Dynamical Localisation

An introduction to chaos and quantum chaos is given, with the important, relevant, discoveries in the field explained. An introduction to dynamical localisation in terms of the kicked rotor and a brief explanation of the optical lattice, with related important experimental work, forms the mainstay of the chapter.

Chapter 3: Ratchets

This chapter gives a summary of the important work to date in the field of ratchet systems. Motivations are given for the study of ratchet systems as well as definitions for each type of ratchet. The key thought experiment of the Smoluchowski-Feynman ratchet and the recent work on deterministic ratchets are explored in more detail.

Chapter 4: Classical Theory

The ratchet proposed in this thesis is presented classically. The system Hamiltonian is given and a discrete mapping derived. System symmetries, phase space plots and the ratchet mechanism (in terms of the diffusion constant) are all explained.

Chapter 5: Classical Calculations

In this chapter the system is modelled classically. The evolution of a Gaussian distribution of trajectories is explored for a wide parameter space. Important trends seen in the system for varying parameter values are explained physically and with reference to the diffusion constant.

Chapter 6: Quantum Theory

The system is presented in the quantum regime with the system Hamiltonian derived from and atom-optics stand point. The time evolution operator, in matrix form, in a plain wave basis, is derived.

Chapter 7: Quantum Results

The system's quantum parameter space is explored in detail. Special attention is given to the localisation length for varying parameter values. Results for quantum ratchet current are presented with a modified Shepelyanski relationship for the ratchet. Also, optimal experimental parameters are suggested.

Chapter 8: Conclusions

A summary of all the results presented in the thesis is given. The importance of the work is again highlighted with suggestions for future work and possible applications.

Chapter 2

Quantum Chaos and Dynamical Localisation

2.1 Chaos and Non-Linear Systems

The study of chaotic dynamics can be traced back to the turn of the 20th century and to the work of Henri Poincaré, the French mathematician. His interest was in planetary orbits around a star, where all bodies experience gravitational forces acting on each other. He considered sets of starting conditions and was able to show that extremely complex orbits are possible. There was more important work on chaos in dynamical systems in the early and middle 20th century, including the KAM theory of Kolmogorov, Arnold and Moser, [1]. However, it wasn't until relatively recently that much of this work has been brought over to the analysis of real physical systems. Much of the reason behind this was the invention of the computer which has allowed large scale simulations of these complex systems to be possible, for example, the great improvement in our ability to predict the weather. With extended use of computers, many of the complexities in chaotic systems could be shown to be real effects rather than being blamed on experimental errors and short-fallings. Chaotic motion has been seen in many different and surprisingly simple systems, even the dripping of water from a tap can be argued to exhibit chaotic motion at a sufficiently large inflow rate.

Deterministic chaotic motion is understood in terms of unstable orbits characterised by exponential sensitivity to changes in initial conditions, i.e. a small change in initial conditions can lead to dramatic changes in system behaviour. Despite the fact that, over short time intervals, the motion of these systems seems smooth and flowing, typically they will never reach a reasonable fixed state with a recognisable pattern, as over long times unpredictable jumps are made in their position, momenta and state. It is because of the high degree of the complexity of the dynamics that, theoretically, chaotic systems are understood in terms of statistical concepts such as system entropies and diffusion rates. Some of the phenomena seen in chaotic systems are quite universal and have dependencies on just a limited number of the parameters of the system.

2.2 Quantum Chaos

Over the last twenty five years or so, the study of the quantum dynamics of systems with chaotic classical behaviour has been one of considerable interest and activity in the scientific community. It is the study of these systems that has become generally known as quantum chaos. Chaotic classical dynamics require an infinite amount of detail in phase-space, which is excluded by the Heisenberg Uncertainty principle of quantum mechanics. However, these systems often have signatures of the classical chaos (such as *quantum scars* or Wigner-Dyson spectral statistics) in the quantum dynamics. It is this, which has spurred much of the active research. Conversely, quantum effects such as tunnelling, which is allowed in the quantum regime but not in the classical regime, provide an interesting range of additional phenomena at moderate values of $\hbar$. In fact, this difficulty in explaining the absence of chaos in the quantum dynamics, even in the small $\hbar$ limit, made the field of quantum chaos, at first, somewhat controversial. The initial apparent contradiction with the correspondence principle, which requires a transition from quantum to classical as $\hbar$ is reduced to zero, caused much debate and interest. The use of classical mechanics to describe physical systems could be viewed as merely an approximation to the actual and exact description given by quantum theory. The time and length scales of a given system

relative to the quantum wavelength are a good indication to how good the classical description will be. If the quantum wavelengths are small but non-zero, then the system is said to be in the semi-classical regime, and quantum effects start to become important.

This thesis is concerned with time dependent systems, specifically in the case where the Hamiltonian varies periodically with time. Time dependent chaotic systems where the quantum dependancy becomes important (for example, varying electromagnetic field on Rydberg atoms and Molecules) have been studied by Bayfield and Koch, Casati *et al*, Jensen *et al*, Meerson *et al*, [3, 36] and Blümel *et al*, [4]. Work has been carried out on an experimental configuration of Josephson junctions, [104]. Also, important work on the kicked rotor model and the discovery of dynamical localisation, which forms one of the focuses of this report, was done by Casati and Fishman *et al*, [5, 36]. Since their work that particular field has bloomed with experimental realisations of many theoretical predictions, including Wannier-Stark ladders, dynamical Bloch band suppression and the quantum chaos effects of dynamical localisation and chaos assisted tunnelling, [11]-[26].

2.3 Dynamical Localisation

The quantum effect of dynamical localisation in systems where the classical dynamics are chaotic has been found to be a very robust phenomenon. It can be found in a wide range of systems and is insensitive to the small details of the particular systems in which it is found. The effect has been observed in experiments on the ionisation of Rydberg atoms where the relative probability of atom ionisation by a microwave field is suppressed relative to the classical predictions, [5, 4]. The effect is also seen in dissociation of molecules by a strong monochromatic field and kicked optical systems recreating the delta kicked and driven rotor. In all cases classical chaotic diffusion is eventually stopped by quantum wave effects. Dynamical localisation manifests itself in this quantum suppression of classical diffusion and the localisation of quasi-energy eigenfunctions and is best explained in terms of a destructive interference effect. In 1982, a close link between Dynamical localisation in the kicked rotor model and An-

derson localisation in disordered solids was made by Fishman *et al*, [5]. It is this paradigm system which is discussed next to demonstrate this effect.

2.4 The Delta Kicked Rotor

2.4.1 Classical Analysis

Many systems have been thoroughly investigated by many groups around the world in the field of non-linear dynamics, however the most studied of all of these systems is probably the Delta Kicked Rotor. This system was investigated by Casati *et al*, who first showed the effect of dynamic localisation in a quantum chaotic system.

The kicked rotor is considered as a paradigm system in the field of quantum chaos. It consists of a weightless rotor subject to a periodic train of delta kicks, $\sum_n(\delta(t/T-n))$. The Hamiltonian for the system can be written as follows;

$$H(L,\Theta;t) = \frac{L^2}{2I} + k\cos(\Theta)\sum_n(\delta(t/T-n)), \tag{2.1}$$

where Θ, is the angle of the rotor, L, the angular momentum, k, the kick strength, t, time and T the period.

In breaking the system into periods of free evolution interspersed with kicks and by considering each of these parts separately, it can be easily shown that this Hamiltonian can be translated into a discrete mapping. This mapping is written down in terms of the angular momentum, and angle of the rotor immediately before kick number n and immediately before kick number $n+1$. This mapping is known as the standard mapping and is written;

$$l_{n+1} = l_n + K\sin(\theta_n), \tag{2.2}$$

$$\theta_{n+1} = \theta_n + l_{n+1}, \tag{2.3}$$

where all variables, l, θ and K are now written in dimensionless units. n indicates the kick number.

This mapping was first written by Chirikov *et al* [2]. It is clear from the map that the classical dynamics of the rotor depend only on one control parameter, the kicking strength K. An important point to note is that the mapping cannot be solved explicitly, so the best method for predicting l_n and θ_n is by iterating the map itself. The most effective way to observe the dynamics of the system as they change with K is through the use of Poincaré surfaces of section plots (SOS) of the phase space for the system. The angle variable is periodic in 2π and the angular momentum unbounded, making the topology cylindrical for the phase space of the kicked rotor.

These SOS plots can be used to examine how the dynamics can vary as a function of K. As can be seen in figure 2.1 as the kicking strength is increased more and more tori (solid lines running across the plots) are destroyed and chaotic regions appear. At $K \sim 0.97$ it was numerically shown by Greene [76] (and estimated by Chirikov [4]) that the last torus is destroyed and the transition to global chaos is complete. The last KAM torus corresponds to the most irrational winding number $\langle \Delta\theta \rangle = 2\pi R$, where R is the *golden mean* ratio, $R = (\sqrt{5}+1)/2$. As K is further increased the remaining cantori (which are broken tori) are progressively weakened and more and more islands in phase space disappear.

After the last of the KAM tori are destroyed, the system's energy then grows diffusively with the number of kicks and each trajectory is free to expand through all phase space. The average energy for an ensemble of rotors can be written, by considering (2.2) as,

$$E_n = \frac{\langle l_n^2 \rangle}{2} = \frac{C_0 n}{2} + \frac{1}{2} \sum_{m,m'=0}^{n-1} C_{m-m'} \tag{2.4}$$

here, the correlation functions $C_{m-m'}$ are given as,

$$C_{m-m'} = \langle K \sin(\theta_m) \sin(\theta_{m'}) \rangle \tag{2.5}$$

The angle brackets denote an averaging of the ensemble over all phase space and the $(m - m')$ indicates the kick separation over which the correlations are considered. These correlations are short time as they are only found to be significant over small $(m - m')$. In the quasi-linear approximation the value θ_n is assumed to be effectively

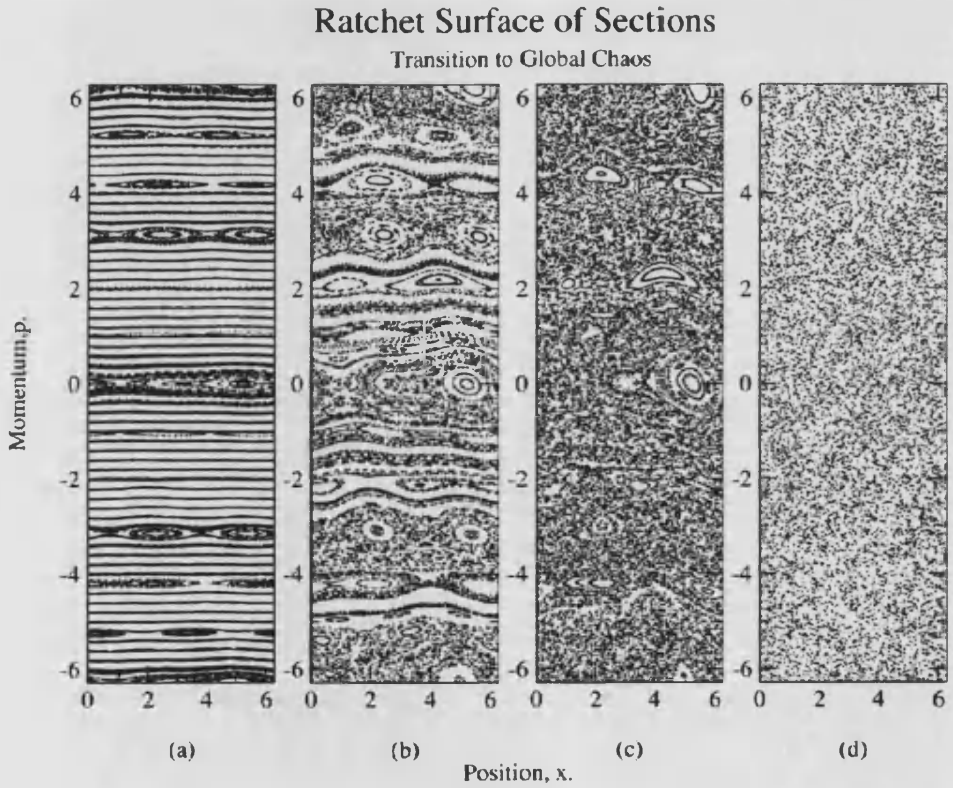

Figure 2.1: Stroboscopic Poincaré surface of section plots for the kicked rotor. (a) Low kick strength $K = 0.3$ nearly all phase space consists of regular manifolds. (b) Mixed phase space with $K = 0.97$ just below threshold for the destruction of the last KAM torus, however, trajectories are still bounded. (c) $K = 2$ in the region of global chaos, trajectories not started on a regular island are free to explore all momentum space. (d) High $K = 5$ phase space is completely chaotic with the exception of only a small number of tiny regular islands.

randomised for large values of the kicking strength. In doing this, equation (2.5) can be simply solved to show,

$$D_{ql}(K) = K^2/4. \tag{2.6}$$

This random phase approximation is effectively assuming a random walk in momentum, so the momentum distribution is asymptotically Gaussian with width $\sqrt{n}$.

For finite values of K, the quasi-linear approximation is not always sufficient. The diffusion rate can deviate from the quasi-linear approximation due to non-zero longer time correlations. These correction terms were evaluated by use of a Fourier path technique by Rechester *et al*, [74, 75], and shown to be,

$$D(K) = \frac{K^2}{2}\left\{\frac{1}{2} - J_2(K) - J_1^2(K) + J_2^2(K) + J_3^2(K)\right\} \tag{2.7}$$

to $O(K^{-2})$. This formula, although more general than the random phase approximation of equation (2.5), still only takes into account a few early correlations. Even for very large values of the kicking strength there still remain small islands in the chaotic sea. These islands can attract some orbits that wonder past after some time, these orbit may then remain in the area of these islands for many kicks, either reducing or enhancing the chaotic transport of the system, depending on the nature of the islands. There are two types of islands that may form; some surrounding a fixed point of the motion, these islands lead to reduced transport, and accelerator modes [60], where particles are at the correct position at each kick to receive the maximum possible impulse, so momentum is rapidly increased, these islands can enhance transport through streaming [23]. In these regimes the diffusion of the system is known as anomalous diffusion and is particularly apparent around values of K near $2\pi j$ where j is a positive integer. At these values of K, the main family of accelerator modes is stable.

2.4.2 Quantum Analysis

The quantum dynamics of this simple system show some different and surprising results when compared to the classical dynamics. The quantum dynamics can be

analysed in terms of a time evolution operator in the Heisenberg picture of quantum theory. The most general form of the time evolution operator is,

$$\hat{U}(t,t_0) = \hat{T}\exp\frac{i}{\hbar}\int_{t_0}^{t}\hat{H}'(t')dt', \tag{2.8}$$

where $\hat{T}$ is the time-ordering operator. This may be used to evolve the quantum wavefunction over one time period, τ,

$$\Psi(\tau) = \hat{U}(\tau,0)\Psi(t=0). \tag{2.9}$$

In the δ-kicked rotor, $\hat{U}(\tau,0)$ can be factorised into a free evolution part and a kick part, reflecting the two halves of the Hamiltonian.

$$\hat{U}(\tau,0) = \hat{U}_{total} = \hat{U}_{free}\hat{U}_{kick}. \tag{2.10}$$

The evolution operator can be written;

$$\hat{U}_{free} = \exp(-\imath\tau\hat{\ell}^2/2) \tag{2.11}$$

and

$$\hat{U}_{kick} = \exp(\imath k\cos(\theta)), \tag{2.12}$$

Where $\hat{\ell}$ are the momentum operator ,θ represents the position. τ and k are the new dimensionless quantum control parameters.

To evolve the system quantum mechanically the evolution operator is used to iterate the wavefunction, and the quantum evolution takes the form;

$$\Psi((n+1)\tau) = \hat{U}\Psi(t=n\tau). \tag{2.13}$$

The simplest method to attain numerical results for the quantum kicked rotor is to expand the rotor wavefunction in the angular momentum basis with the iterated wavefunction calculated from the expansion amplitudes of the angular momentum eigenstates. In plotting the quantum mechanical energy growth, calculated as,

$$E_n = \langle\psi_n|\hat{\ell}^2/2|\psi_n\rangle = \hbar^2\sum_{\ell=-\infty}^{\ell=\infty}\ell^2|\psi(\ell)|^2, \tag{2.14}$$

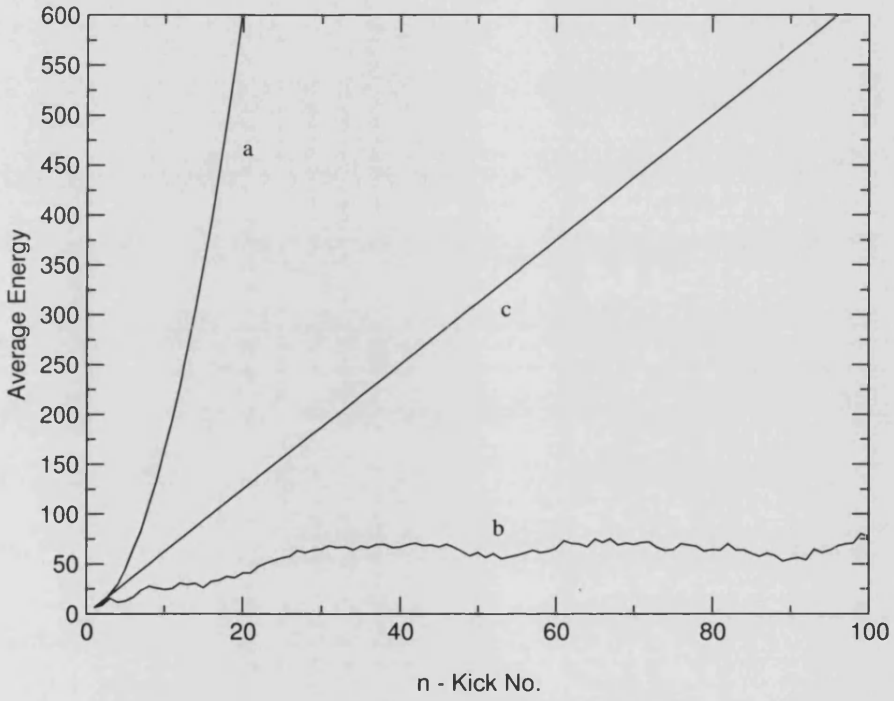

Figure 2.2: Kicked rotor plot for energy vs time (measured in kicks). Both classical (c) and quantum behaviours are plotted. Line (a) displays the effect of a quantum resonance and exhibits parabolic behaviour. (b) shows the more widely seen quantum localisation where quantum energy growth is suppressed by localisation of the wavefunction in momentum space

for values of the quantum control parameters corresponding to classical $K = 5$, two unexpected results were observed and are displayed in figure 2.2.

Firstly, for τ as rational multiples of π, quadratic energy growth was observed. This unexpected behaviour, which is caused by the existence of quantum resonances, was first researched by Izrailev and Shepelyansky in 1979 [63]. This effect has be understood by considering that, between kicks the system evolves by an amount,

$$U_{free} = \exp \frac{-il^2\tau}{2}, \tag{2.15}$$

where l is an integer. This means that if τ is a rational multiple of π, the phase is not randomised between consecutive kicks. In fact for $\tau = 4\pi$, $\hat{U}_{free} = 1$ and the system experiences no evolution at all between kicks. Hence, the effect of the kicks accumulates constructively. So rational values of τ/π correspond to the quantum resonances, [5].

Secondly, the discovery of dynamical localisation, which manifests itself as the suppression of the quantum energy growth [63, 4, 5, 36]. Dynamical localisation is explained as an interference effect that stops the wavefunction spreading out into all of the available angular momentum basis. The dynamical localisation in the quantum kicked rotor system is characterised in terms of the localisation length and the quantum break time. The localisation length defines how fast the momentum falls off exponentially after the wavefunction becomes frozen in momentum space. This freezing of the rotor energy only occurs after a finite period of time t^*, the quantum break time, before this time, the quantum energy diffuses as the classical energy does until the quantum coherence effects arrest the diffusion of the wavefunction. The smaller the effective $\hbar$ of the system, i.e. the more classical the system is, the longer the quantum dynamics follow their classical counterparts. However, even for small τ the quantum interference effects eventually dominate. Estimations for the localisation length, L, and the break time were made by Shepelyanski, [63], he states $L \sim D/\hbar$ and $t^* \sim L/\hbar$. A strong argument for the explanation of dynamical localisation was put forward by Fishman *et al*, [5], he proposed that dynamical localisation is analogous to Anderson localisation in disordered solids. He showed that the quantum rotor dynamics could in fact be mapped on the Anderson model as there is a close

similarity of Floquet's theory for time periodic systems and the Bloch theorem for spatial periodicity. The time evolution of a wavefunction can be expanded in the following way,

$$\psi(\theta,t)=\sum_{\omega}A_{\omega}\psi_{\omega}(\theta,t) \tag{2.16}$$

where the A_ω are constants, ω is the quasi-energy and the quasi-energy eigenstates are given by,

$$\tilde{F}\psi_{\omega}(\theta,t)=\exp(-\imath\omega)\psi_{\omega}(\theta,t) \tag{2.17}$$

and $\tilde{F}$ is the quasi-energy operator. Notice that $\tilde{F}$ is the one period time evolution operator in equation (2.8). Floquet's theorem states that, for a time periodic system, the eigenfunction can be written,

$$\psi_{\omega}(\theta,t)=\exp(-\imath\omega t)u_{\omega}(\omega,t) \tag{2.18}$$

where u_ω is periodic in time with the same periodicity as the Hamiltonian,

$$u_{\omega}(\omega,t)=u_{\omega}(\omega,t+1). \tag{2.19}$$

Here the period of the system has been normalised to unity. Next the quasi-energy states are projected onto the momentum states so their properties can be investigated, it can be shown that,

$$u_{\ell}^{-}=\exp(\imath(\omega-\tau\ell^{2}/2))u_{\ell}^{+} \tag{2.20}$$

and

$$u^{+}(\theta,m)=\exp(\imath V(\theta))u^{-}(\theta,m) \tag{2.21}$$

where, u^+ and u^- are values just after and just before a kick. It can be further shown that by introduction of the function, $W(\theta)=-\tan(V(\theta)/2)$, the rotor model is mapped to the Anderson model,

$$T_{\ell}\bar{u}_{\ell}+\sum_{r}W_{\ell-r}\bar{u}_{r}=0 \tag{2.22}$$

with

$$T_{\ell}=\tan(\frac{1}{2}(\omega-\frac{1}{2}\tau\ell^{2})) \tag{2.23}$$

which are the diagonal matrix elements. The hopping matrix elements are $W_{\ell-r}$ and are projected onto the momentum basis. $\bar{u}_\ell$ is the average u_ℓ before and after a kick. In analogy to the Anderson model, ℓ is the lattice site. In the Anderson model T_ℓ is an externally given random number reflecting impurities in the lattice and it is this randomness which prevents one solution of the Bloch wave at every lattice site, in effect localising the wavefunction. In the rotor mapping for large values of ℓ the value T_ℓ varies erratically and can be thought of as being in essence the *random* factor required for dynamical localisation.

2.5 Experimental Developments

Recent developments in the world of laser cooling and trapping have enabled many of the theoretical predictions put forward in quantum chaos to be tested. The control of the external degrees of freedom of atoms in laser fields has become more and more exact. The work done in the field recently led to the Nobel prize for S. Chu, W. P. Phillips and C. Cohen-Tanonudji for the optical lattice in 1997 and for Eric Cornell, Carl Weinmann and Wolfgang Ketterle for the observation of a Bose-Einstein condenstate in a dilute gas in 2001. In particular, the realisation of the optical lattice has enabled the prediction of the quantum effect of dynamical localisation described above to be demonstrated in experiment and henceforth many interesting phenomenon that depend on it.

2.5.1 The Optical Lattice

An optical lattice [28, 31] can be in broad terms described as the interaction of a cold atomic gas with a spatially modulated light field to form an ordered pattern, in effect, an *ordered gas.* These light bound atom lattices typically consist of alkali-metal atoms, for example sodium and cesium. The light interaction acts on the degrees of freedom of the atoms as a force dependent on the internal state of the atom and proportional to the polarisation of the laser light. A periodic one dimensional optical lattice is achieved by setting up a standing wave of laser light using counter

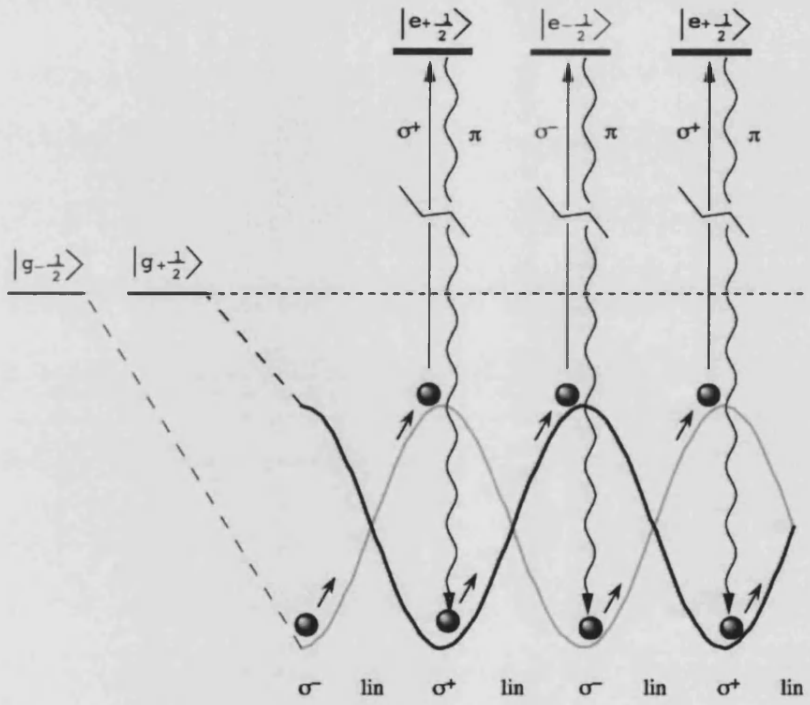

Figure 2.3: The process of Sisyphus cooling in an optical lattice. The atomic energy levels are modulated by the phase variation in the laser light (light shifts) creating a potential energy surface. Spatial correlation between the light shift and the optical pumping ensures a loss in atomic K.E. as the atom climbs the potential but never goes without photon recoil, from [29]

propagating, coherent and orthogonally linearly polarised beams. This gives a spatial variation in the polarisation of the light field and hence a spatial variation of the photon angular momentum. The potential the atoms see is associated with the spatial variation of the light shifts of the atoms internal states (ac Stark shifts), known as a light-shift potential energy surface, figure 2.3. The cooling mechanism at the heart of the optical lattice is Sisyphus cooling, named after the legendary king of Corinth, who was condemned to a punishment of rolling a huge stone up a hill, only to have it roll to the bottom before he reached the summit each time, [33]. In the realm of the optical lattice the atom is optically pumped down to the potential minima of the other ground state sub-level as it climbs the potential hill. During this process, on average, the kinetic energy lost through the spontaneously emitted photons is larger than that from the photons absorbed from the light field. This reduction in kinetic energy of the atom eventually renders it trapped in the potential wells of the energy surface. Once trapped in the lattice, these cold atoms can be very precisely manipulated opening new possibilities for experimentation.

2.5.2 Experimental Results

With the new tool of the optical lattice available, a large body of experimental work has been done, verifying large amounts of theoretically predicted physics as well as discovering new physics. A good proportion of this effort was put towards creating an experimental test bed for the kicked rotor system in particular. This effort was motivated by the fact that much of the large body of the theoretical work done on this model and some similar models remained unverified and also that these systems display a rich variety of phenomena from very simple equations of motion.

The first experimental kicked rotor was realised by the Raizen group in Texas, [11], in terms of a pulsed optical lattice. This work was done with trapped sodium atoms and not only demonstrated dynamical localisation but also quantum resonances for specific values of the pulse period, notably for multiples of the natural period. In their experiment, as a delta kick is not experimentally feasible, a very narrow pulse width was used. This had the disadvantage of the control parameter K, falling off in

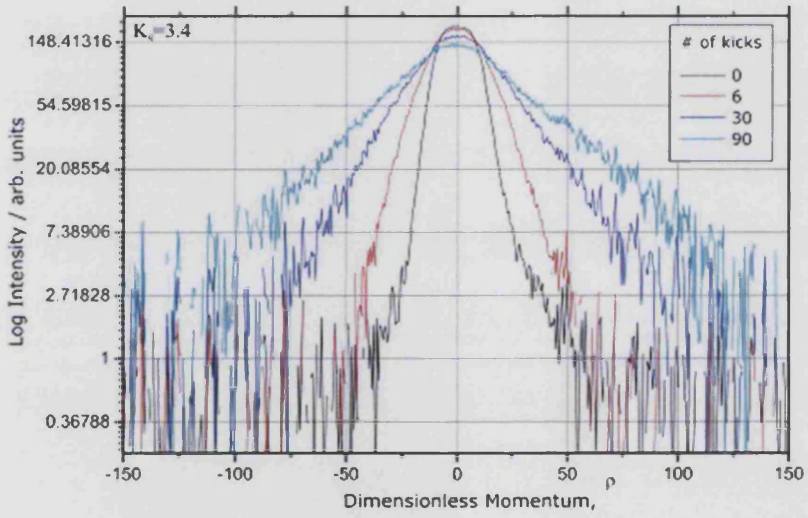

Figure 2.4: Localised momentum distributions achieved by the Meacher Group at UCL for an experimental realisation of the kicked rotor. The figure shows momentum distributions for ultra cold caesium atoms in an optical lattice. The straight sided signature of a dynamically localised distribution is clear after 90 kicks (turquoise line).

intensity for larger momentum. In later experiments, the group changed to cesium atoms in their kicked rotor setup, [12]. The large atomic mass of cesium allows a larger amount of momentum space to be investigated for an equivalent pulse duration.

In previous work the group had already experimentally realised the periodically driven rotor, [14], which was first suggested by Zoller *et al*, [66]. In this model the phase of the standing light wave is sinusoidally modulated. Momentum transfer only occurs when the velocities of the atom and the standing wave are matched, these momentum transfers are known as resonant kicks. Above a certain atomic velocity, these resonant kicks (RK) switch off and so there is a predicted RK boundary and this was shown experimentally. Dynamical localisation was also observed experimentally in the regime where t^* is less than the time taken to reach the RK boundary.

In 1996 the group experimentally demonstrated the overlap criterion, [15]. This was done by observing a single pulse momentum transfer and varying the pulse duration to show a critical pulse length required to induce chaotic behaviour. For this chaotic behaviour to be observed, the quantum break time must be significantly longer than the interaction time.

The group did further experiments on atomic tunnelling, in 1997, [16], using an accelerating optical potential. tunnelling was investigated in terms of the maximum acceleration allowed before the atomic loss from the wells became too large. This acceleration limit was reach well before the predicted classical limit and was attributed to quantum mechanical tunnelling. The atoms tunnelled out of the potential wells via Landau-Zener transitions to higher energy bands until they became effectively free particles. More recently, [17], the group investigated chaos assisted tunnelling. The experimental set-up was an amplitude modulated standing wave double well. Experimental parameters set in the region of mixed phase space. A quantum wavepacket is predicted to oscillate between two symmetry related islands, this tunnelling can be enhanced in the doublet state of the double well by interaction with a chaotic state. This effect was demonstrated to be reduced in the presence of noise and decrease with the coupling strength, α, which is in opposition to expectation for two state

tunnelling. The Hamiltonian for the system is written,

$$H = p^2/2 - 2\alpha\cos^2(\pi t)\cos(x) \tag{2.24}$$

More work was done on the effects of noise on the quantum dynamics, [18]. The group showed that dynamical localisation is completely destroyed for high amplitude noise and that at lower $\hbar$ the system becomes more sensitive to this noise. This showed that the system of the kicked rotor could be driven to its classical limit through noise. They showed this through recovered diffusive growth in their system and Gaussian momentum distributions.

The group were also the first to experimentally show dynamical Bloch band suppression, [20]. This is achieved through strong phase modulation of the standing wave light field which causes the band structure to collapse stopping the dc transport which was driven by the ac field. More recent work has been the state reconstruction of the kicked rotor, [21], in which a clever interferometric method was used involving a mixed starting state. Half of the state feels the kicked rotor potential and the other half does not. The unaffected half can then be used as a reference state to recover the phase of the wavefunction as well as its amplitude. This could provide insight into the phase behaviour at the heart of dynamical localisation and quantum resonances.

Other important experimental work in the field has been done by a group at Oxford University. The main experimental discovery of this group is that of quantum accelerator modes, [57, 59, 61]. While accelerator modes have been known classically for many years a quantum counterpart had not been experimentally shown. These quantum accelerator modes exhibit large energy growth exceeding classical predictions. The accelerator modes were achieved in a system very similar to the delta kicked rotor, the only difference being, that the cesium atoms are allowed to fall freely under gravity between the kicks and the potential is oriented in the vertical plane. The group have also developed a theoretical model for the effect. According to their model, these modes can be understood as the repeated application of blazed diffraction gratings. These accelerator modes are a very efficient way of imparting a coherently large amount of momentum to a particle. A possible application is put forward in terms of an atomic beam splitter although only momentum change can

be accomplished and not amplitude splitting. The group later investigated the effect of noise in the form of random scattering events. Noise effect were investigated in the regime of the quantum accelerator modes, [60], and it found that the effect was reduced significantly by the introduction of noise. The group also investigated noise in the region of quantum resonance in the delta kicked rotor, [58]. In these regions, the system proved to be especially sensitive to noise compared to the well localised regions studied by other groups. The argument then is that it is in these resonant regions of the system dynamics that will provide the best testing ground of quantum-classical correspondences.

Chapter 3

Ratchets

3.1 Motivation for the Study of Ratchets

Ratchets are in wide ranging use today, both in man made technologies and in nature. Artificial ratchets are used mainly as energy saving devices, making useful work from random motions. For example, a self winding wrist watch uses some of the kinetic energy from the motion of the wrist on which it is worn to load the spring in the watch's mechanism, which in turn drives the watch's hands. Winding wrenches on yachts, spanners, and screw drivers all use simple ratchets, allowing work to be done only in one direction, providing labour-saving devices and improving efficiency. As technology pushes further and further towards the atomic level, the motivation for the scientific study of ratchet systems becomes more apparent. Already nano-technological devices are used to manipulate on the atomic level. Ratcheting systems could be implemented in these technologies to provide a possible method for atomic transport. Nature also provides us with a great motivation for understanding molecular ratchets on a biophysical level. Cell highways could possibly be understood on a molecular level in terms of a ratchet system. Cell highways are the means by which chemicals are transported around cells. It is conjectured, [37], that Brownian noise effects along with a broken parity symmetry potential is the motor behind these highways. In fact as almost all systems are subjected to random fluctuations in some form or another, often as an unavoidable consequence of the environment in which

the system is situated (for example thermal noise), the idea of utilising this natural randomness is very appealing.

3.2 The Definition of a Ratchet

The ratchet effect can be defined as the rectification of random or anti-symmetric fluctuations into useful work. In many cases, this can be narrowed down further to preferred or directed transport in spatially periodic systems. However, this useful work cannot be achieved without cost. Gaining useful work from a system which exerts no net force in a particular direction without the input of energy, for example, a spatially periodic system in contact with a single thermal heat bath, is ruled out by the second law of thermodynamics. This was first investigated by Smoluchowski and was presented in conference in 1912 and later extended by Feynman in his popular Lectures on Physics, [106] The two investigators' model system was a simple ratchet and pawl and is explained in section (3.3.1). Many types of ratchet system, some of which are very complicated in structure, have been investigated since and as a result, a common thread of requirements has been established to produce a ratchet effect or directed transport. Most importantly, the system must not be in thermal equilibrium in order to obey the second law of thermodynamics. Aside from this requirement, system symmetries must be appropriately lowered. Time reversal symmetry must be destroyed and this symmetry is most commonly broken by the use of thermal noise. Also in many systems, the spatial inversion symmetry is required to be broken in conjunction with the broken time symmetry. In fact there is a hypothesis which states that: *if a certain phenomenon is not ruled out by symmetries then it will occur.* This is known as Curie's principle. So one can argue, some cases that show no transport are equally as interesting as those which do. The symmetry requirements suggested above for directed transport are most commonly achieved through either one of three basic schemes: pulsed ratchets, tilting ratchets and fluctuating state ratchets. Examples and definitions of each type are outlined and reviewed in this chapter. However, the main focus of this thesis is on the stochastic, pulsed scheme. There are, as always, exceptions to rules and, as discussed later, a special set of apparently broken symme-

try systems are possible that produce no directed transport [41]: these systems are referred to as supersymmetric. In the progression of this research field, noisy Brownian motors have been studied, then noise free dissipative ratchets and finally clean Hamiltonian ratchets. Ratchets have been studied in both the classical and quantum regimes. The largest body of research has been in Brownian ratchets, probably because these ratchets have the most obvious motivation from biophysics, for a full review see [40]. There has been a tendency to reduce models towards the more simple systems more often found in the study of non-linear dynamics. So the first logical step in the simplification of the models was to remove the random noise in favour of deterministic chaos. The ratchets effect was first accomplished in these systems by including frictional terms, [83]. These ratchets became known as deterministic inertia ratchets with dissipation. The next step in the chain was the removal of all frictional terms. These ratchets rely only on the chaotic Hamiltonian dynamics and so are the cleanest, most simple systems. Unlike the dissipation ratchets mentioned above, where a large body of research has been carried out, there has been little in comparison for this last class of ratchet. Notable exceptions are Schanz *et al* and Flach *et al*, [53, 54, 52]. A more detailed overview of the important and recent work in the field is presented in the following sections.

3.2.1 Types of Ratchet

As hinted at earlier, there are many different and diverse ways to achieve a ratchet effect and whether considering the quantum or classical, Hamiltonian or noisy regimes most can be classified into three groups: pulsed ratchets, tilting ratchets and state fluctuating ratchets or a combination thereof. Here, a model equation of motion (in this case for a noisy dissipative system) is introduced so as to demonstrate the various classes and highlight the differences between them. The particular form of each term on the right hand side can be related to a different type of ratchet.

$$m\ddot{x}(t) + \eta\dot{x}(t) - F = -V'(x(t), g(t)) + y(t) + \xi(t) \tag{3.1}$$

ξ represents Gaussian white noise of zero mean, which satisfies the relation:

$$\langle \xi(t)\xi(s) \rangle = 2\eta\kappa_B T\delta(t-s) \tag{3.2}$$

F is the force against which the ratchet can do work and $y(t)$ represents a time dependent tilting of the potential. η is the coefficient for viscous friction. Primes mark differentials with respect to x, and dots with respect to t. The potential $V(x,g)$ is periodic in x. The potential will be termed as a ratchet potential if it does not satisfy the symmetry condition $V(-x,g(t)) = V(x+\Delta x, g(t))$. The tilting process $y(t)$ is inversion symmetric if there is a Δt satisfying $-y(t) = y(t+\Delta t)$ or, if the $y(t)$ is stochastic, symmetry requires that all statistical properties are identical for $-y(t)$ and $y(t)$ alike.

Pulsed Ratchets

Pulsed ratchets themselves can be divided up in to two main subclasses. The first is when the potential is modulated or kicked and takes the mathematical form,

$$V(x,g(t)) = V(x)[1+g(t)]. \tag{3.3}$$

Ratchet models of this form are generally known as fluctuating potential ratchets. In the case where the function $g(t)$ can only take the values ± 1, the fluctuating ratchet becomes an on-off ratchet. In the extreme case, where $g(t)$ takes the form of a delta function, the system is being kicked in a similar way to the kicking seen in the kicked rotor model described in the previous chapter. It is this type of ratchet potential that is explored in detail in this thesis.

The second subclass of the pulsating ratchet is where the potential can be written in the form:

$$V(x,g(t)) = V(x-f(t)). \tag{3.4}$$

This is a travelling potential ratchet type. Here the potential is most commonly subject to a drift and hence breaks the symmetries defined earlier. Only after the subtraction of this drift are the symmetries seen. It should be noted that, in this potential arrangement, a non-zero current is possible without the need for a ratchet

potential of the form defined earlier, i.e., a symmetric potential can produce a system current.

Tilting Ratchets

In this case, we focus on the $y(t)$ term and where this term is stochastic, the name fluctuating force ratchets is used. In the case where the $y(t)$ is periodic in nature the well known and experimentally very significant rocking ratchet results. In order to gain non-zero current, either an asymmetric $V(x)$ when $y(t)$ is symmetric is necessary, or the reverse, $y(t)$ asymmetric while $V(x)$ is symmetric. Non-zero current can also be gained when both term are asymmetric.

State Changing Ratchets

In the case where both $g(t)$ and $y(t)$ are zero, the ratchet effect can still be achieved for a ratchet potential by changing the state of the system in a periodic manner. The most obvious route to this is the changing of the temperature of the entire system, either modulated in respect to time, a temperature ratchet, or with respect to space, known as a Seebeck ratchet. A potentially more subtle example could be seen in atom optics, with atoms fluctuating between two states or potential surfaces of an optical lattice, exploring the dynamics of fluctuations between independently added states.

3.3 Brownian Motors

Brownian motors exploit the fact that most systems are subjected to thermal noise. On a molecular level this thermal noise is easily demonstrated in terms of Brownian motion and can be seen by the motion of a polystyrene ball floating on the surface of warm water in almost every school laboratory. The detailed study of the molecular motion of Brownian particles revolves around three sets of equations. The Langevin, Fokker-Planck and Smoluchowski equations represent Brownian motion on different time scales of the motion respectively, the Smoluchowski equations being over the longest time scale. The next section explores briefly the most well known of

Figure 3.1: A graphical representation of the Feynman ratchet showing both the bombarded panels and the ratchet and pawl. From [50].

Brownian motors, proposed by Smoluchowski in a thought experiment in 1912.

3.3.1 The Smoluchowski-Feynman Ratchet

The system, figure 3.1, often referred to as the Smoluchowski-Feynman Ratchet, consists of an axle with paddles attached to one end and a saw-toothed ratchet and pawl at the other. A small weight is attached in the middle of the axle to allow the work done by the system to be measured. The whole system is surrounded by a gas in thermal equilibrium. Without the pawl, if the system could freely turn it would perform rotational Brownian motion caused by the random impacts of the gas molecules on the paddle in all directions. The pawl is designed to allow only motion in one direction: the forward direction. It is intuitive that the pawl would allow the teeth to pass in the forward direction if there were enough favourable impacts from the gas molecules, and not at all in the backward direction. So, it would seem at

first sight that the system would slowly turn in the forward direction, even without the input of external energy, this, on the condition that the ratchet can overcome the stopping force of the small weight. This would of course be a perpetual motion machine, strictly forbidden by the second law of thermodynamics. Something must have been overlooked and the working of the pawl would seem to be the most natural suspect. The pawl, resembling a Maxwell's demon, as shown by Smoluchowski, would also be affected by the thermal impacts of the gas molecules. These impacts can lift the pawl, thus allowing motion in both directions. When the pawl can be lifted by these impacts, the motion of the axle will be in favour of the backwards direction. Indeed, quantitative analysis shows the right balance to prevent such a perpetual motion machine. When this ratchet and pawl model was experimentally recreated on a molecular scale, [46], with use of nuclear magnetic resonance techniques, the lack of any preferred direction was verified. Later, Feynman extended the ratchet pawl model, [106]. He explored the case where the cog-wheel and pawl at one end were surrounded by a gas at temperature T_A, while the paddles were surrounded by a gas of temperature T_B. Feynman showed that the system does work if the temperature are not equal. He also showed that the system does this work with an efficiency of $(T_A - T_B)/T_A$, the Carnot efficiency. Feynman also pointed out a similarity with an electrical rectifier with an asymmetric response to an external static force field. Here too, random thermal variations are not converted to useful work in any way. In this example, the effect (or lack thereof), is known as Brillouin's paradox. The analysis of the ratchet and pawl presented by Smoluchowski and Feynman is complex, so as a guide system which displays the qualitative features of the ratchet and pawl, an analysis of a Brownian particle is followed from [41], in the following section.

3.3.2 The Brownian Particle

A Brownian particle subjected to a periodic potential is considered in one dimension. Newton's equation of motion for this particle can be written as,

$$m\ddot{x}(t) + V'(x(t)) = -\eta\dot{x}(t) + \xi(t). \tag{3.5}$$

Here the left hand side of equation (3.5) is made up of the inertial term and the force resulting from the periodic potential interaction and so is the conservative and deterministic part of the particle dynamics. On the right hand side is the thermal environment of the system, made up of the thermal noise and viscous friction, these two terms arising from the same source. Once again the thermal noise is Gaussian white noise of zero average satisfying the fluctuation-dispersion relationship (3.2). In re-scaling the system into dimensionless units, it becomes apparent that in the regime of over-damped dynamics, the re-scaled mass of the particle is small compared to the other system terms, therefore, to a good approximation the inertial term $m\ddot{x}$ can be dropped.

A statistical approach is now taken, where an ensemble of Brownian particles is considered. Since each particle being independently acted on by one of the random fluctuations of $\xi(t)$, a probability distribution describing the distribution of the Brownian particles can be written,

$$P(x,t) = \langle \delta(x - x(t)) \rangle, \tag{3.6}$$

which can be normalised to unity by direct integration.

The key to the dynamics is the time evolution of the probability distribution (3.6). Two special cases are considered: Firstly $V'(x) = 0$, a free thermal diffusion of a Brownian particle. This diffusion is described by the Einstein relation,

$$D = \frac{k_b T}{\eta} \tag{3.7}$$

and the evolution of $P(x,t)$ by the diffusion equation,

$$\frac{\partial}{\partial t} P(x,t) = D \frac{\partial^2}{\partial x^2} P(x,t). \tag{3.8}$$

The next special case to consider is the deterministic case, so the noise contribution $\xi(t)$ is zero. In this case, the dynamics of $P(x,t)$ are evolved through a Liouville equation,

$$\frac{\partial}{\partial t} P(x,t) = \frac{\partial}{\partial x} \Big[\frac{V'(x)}{\eta} P(x,t) \Big] \tag{3.9}$$

In the case where neither $\xi(t)$ or $V'(x)$ is zero, the evolution of the probability distribution is a combination of both equations (3.8) and (3.9) due to the linear nature in $P(x,t)$. Now the Fokker-Planck equation can be written as,

$$\frac{\partial}{\partial t}P(x,t) = \frac{\partial}{\partial x}\Big[\frac{V'(x)}{\eta}P(x,t)\Big] + D\frac{\partial^2}{\partial x^2}P(x,t) \tag{3.10}$$

As for determining whether there is a ratchet effect or directed transport and the extent to which it is occurring, the quantity of greatest interest is the average velocity of the ensemble of Brownian particles, the particle current. The definition of the probability current, $J(x,t)$ is introduced, such that,

$$J(x,t) = \langle(\dot{x}(t))\delta(x - x(t))\rangle \tag{3.11}$$

where $\dot{x}(t)$ is the particle current which can be determined by direct integration of (3.11),

$$\langle\dot{x}\rangle = \int_{-\infty}^{\infty} J(x,t)dx. \tag{3.12}$$

It is also possible, from the definition of the probability distribution to write down a continuity equation in $P(x,t)$.

$$\frac{\partial}{\partial t}P(x,t) + \frac{\partial}{\partial x}J(x,t) = 0, \tag{3.13}$$

by comparison to equation (3.10) the specific Fokker-Planck equation for the Brownian particle an expression for the probability current can be obtained,

$$J(x,t) = -\Big[\frac{V'(x)}{\eta} + D\frac{\partial}{\partial x}\Big]P(x,t), \tag{3.14}$$

so then, by directly integrating (3.14), an expression for the particle current can be derived for a given potential, $V(x)$. When considering the long time limit, as t approaches infinity, a steady state probability density is expected for physical reasons. As a result of this, the probability current would also reach a steady state. Equation (3.12) can be re-written, by means of partial integration, as:

$$\langle\dot{x}\rangle = \int_{-\infty}^{\infty} x\frac{\partial J(x,t)}{\partial x}dx. \tag{3.15}$$

Now, by using (3.13), the expression for the particle current can be again re-written as follows,

$$\langle \dot{x} \rangle = -\int_{-\infty}^{\infty} x \frac{\partial P(x,t)}{\partial t} dx. \tag{3.16}$$

Therefore, for a long time limit steady state probability distribution, $\partial P(x,t)/\partial t = 0$, it is expected that the ensemble average particle current will fall to zero.

$$\langle \dot{x} \rangle = 0. \tag{3.17}$$

Therefore, as required by the second law of thermodynamics, no net work is performed by this system when it is in thermal equilibrium. In the condition that thermal equilibrium is broken, the results are different. In considering a system where the temperature, or the noise intensity, is varied with time, an excellent demonstration of an on-off ratchet is demonstrated. The equation of motion for the Brownian particle can be updated as follows,

$$\eta \dot{x} = -V'(x) + g(t)\xi(t). \tag{3.18}$$

Here the intensity of the Gaussian white noise is modulated by the function $g(t) = [\eta k_B T(t)]^{1/2}$. $T(t) = \bar{T}[1 + A\mathbf{Sgn}(\sin(2\pi t/\tau))]$ and is a periodic function in time with period τ. So, the temperature function $T(t)$ jumps between values of $\bar{T}[1 + A]$ and $\bar{T}[1 - A]$ twice every period. The particle current in this new system can be shown to be non-zero for an asymmetric potential, as here the probability distribution does not reach a steady state long term behaviour due to the permanent temperature oscillations. The probability function becomes periodic in time in the long time limit. Because of this periodic behaviour, it makes more sense to write a time averaged particle current over one period,

$$\langle \dot{x} \rangle = \frac{1}{\tau} \int_{t}^{t+\tau} dt \int_{-\infty}^{\infty} \frac{-V'(x)}{\eta} P(x,t). \tag{3.19}$$

The mechanism for the ratchet effect in this system is explained as follows: In the first part of the time period, the thermal energy is at a constant value, $k_B\bar{T}[1 - A]$, which is smaller than the potential barrier height (the change in the magnitude of $V(x)$ between the maxima and minima). As a result of this, the particles will gather

at the local minimum of the potential. In the next half of the time cycle, the thermal energy jumps to a much higher value $k_B\bar{T}[1 + A]$, which is significantly greater than the potential maxima. As a result, the particles don't feel the potential to any great extent and diffuse out evenly for this half period. Next, as the thermal energy is reduced to its original level, the potential is once again significant. Now, once again trapped between adjacent maxima the particles are pushed towards the minima and are redistributed accordingly. It is the fact the potential is asymmetric which leads to this redistribution also being asymmetric resulting in a net displacement every time cycle and a non-zero current. The ratchet effect explained above is tenable with more general temperature variations, so long as they are sufficiently slow to allow particle diffusion. Experimentally, the required manipulation of the thermal energy in terms of time scale and magnitude could be difficult to achieve. However, many Brownian ratchets have been studied experimentally and Buttiker and Landauer achieved macroscopic movement of a particle using a temperature ratchet with a spatially periodic distribution of temperature with the correct asymmetries.

It is easy to see that this temperature ratchet process is extremely similar to the effect of switching on and off the potential itself whereby the particles are put through the same sequence of free diffusion and trapping at local minima by changing the potential rather than the particle energy. In figure 3.2 a schematic diagram of the asymmetric redistribution is shown for such an on-off ratchet.

The on-off ratchet was experimentally realised in terms of polystyrene latex spheres in solution. The experimental set-up was devised by Rousselet *et al* where the spheres were subjected to a pulsed periodic ratchet potential created by switching on and off electrodes deposited on a glass slide. The experiment was later refined by Gorre-Talini using optical diffraction gratings to produce the electrostatic ratchet potential.

In Biophysics, motor proteins are studied as Brownian ratchets, here chemical energy released is used to give unidirectional motion. The ratchets effect is thought to explain muscle action and contraction as well as intracellular transport. Experiments have been carried out to measure the stopping force in Kinesin transport along microtubes [84] which is fueled by the exothermic chemical hydrolysis of ATP into ADP + P, releasing approximately $20k_bT$ of chemical energy in the reaction.

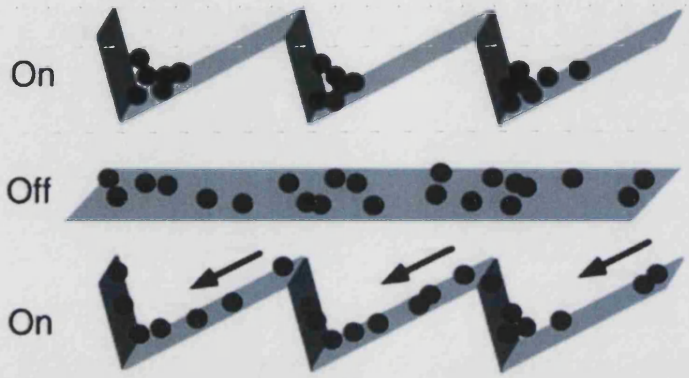

Figure 3.2: An on-off ratchet to illustrate the mechanism for directed transport from [91]. While the potential is on the particle form around the potential minima. As soon as the potential is switched off the particle diffuse in all directions, as the potential is re-engaged the particles move to the next minima and are thus asymmetrically redistributed. This results in a net current to the left despite there being no net force.

3.3.3 Quantum Brownian Ratchets

Most of the ratchet effects already considered occur on a very small scale, where although the phenomena are classical in nature, it is on the molecular level that the systems are considered. It is therefore a very natural and obvious step to next consider whether quantum mechanical effects play an important role in the workings of these sometimes nano-scale ratchets. It could well be expected that important and surprising results may be discovered when the system length, time and energy scales are approaching that of the Planck's constant. In modelling the quantum system and the thermal environment, a Hamiltonian framework is used to maintain consistencies with the second law of thermodynamics. The Hamiltonian system consists of a standard Hamiltonian for a particle in a one dimensional ratchet potential $V(x)$ plus a heat bath which is modelled by an infinite number of harmonic oscillators. The infinite number of oscillators means an infinite heat capacity and therefore the heat bath keeps its initial temperature for all time. The Hamiltonian and heat bath are

written as the following equations,

$$\hat{H}(t) = \frac{\hat{p}^2}{2m} + V(\hat{x}) - \hat{x}y(t) + H_B \tag{3.20}$$

$$\hat{H}_B = \sum_{j=1}^{\infty} \frac{\hat{p}_j^2}{2m_j} + \frac{1}{2}m_j\omega_j^2\Big(\hat{x}_j - \frac{c_j\hat{x}}{m_j\omega_j^2}\Big)^2, \tag{3.21}$$

where $\hat{x}$ and $\hat{p}$ are the position and momentum operators of the particle and the $\hat{x}_j, \hat{p}_j$ denote those of the heat bath oscillators. The $y(t)$ is a tilting force which is unbiased on average. The effect of the thermal environment, which is coupled via the coupling strengths c_j to the base system, is controlled by the spectral density of the heat bath. Integrating over the bath degrees of freedom it is possible to arrive at an analogous equation to (3.5) such that left hand side of the equation describes the system dynamics and the right hand side describes the thermal environment.

$$m\ddot{\hat{x}}(t) + V'(\hat{x}(t)) - y(t) = -\int_0^t \hat{\eta}(t-t')\dot{\hat{x}}(t')dt' + \hat{\xi}(t). \tag{3.22}$$

A theoretical system was considered by the Reimann *et al* [42]. The group considered a model where the driving term $y(t)$ was limited to values only of $\pm F$. This they called the *adiabatically tilting quantum ratchet.* While making the assumptions of weak noise compared to the potential barrier height and excluding running solutions (i.e. a classical, noise free, particle would reside in the potential minima under tilting) the group made two interesting observations. Firstly, that at low temperatures the directed quantum transport of the system was considerably enhanced compared to the classical behaviour and as the temperature was lowered this effect was increased further. As the temperature was increased the classical dynamics were approached. Secondly, as the temperature of the system is lowered still further, the system undergoes a current reversal. Classically, as the temperature is lowered, no such reversal occurs. Both of these observations are surprising. The asymmetry in the potential, the barrier height that particles need to overcome is lower for a tilt to the right in figure 3.2 than a tilt to the left, therefore, the directed current would classically always be expected to be to the right. The quantum mechanical particles can tunnel through barriers however. The tunnelling probability for a particle not only depends

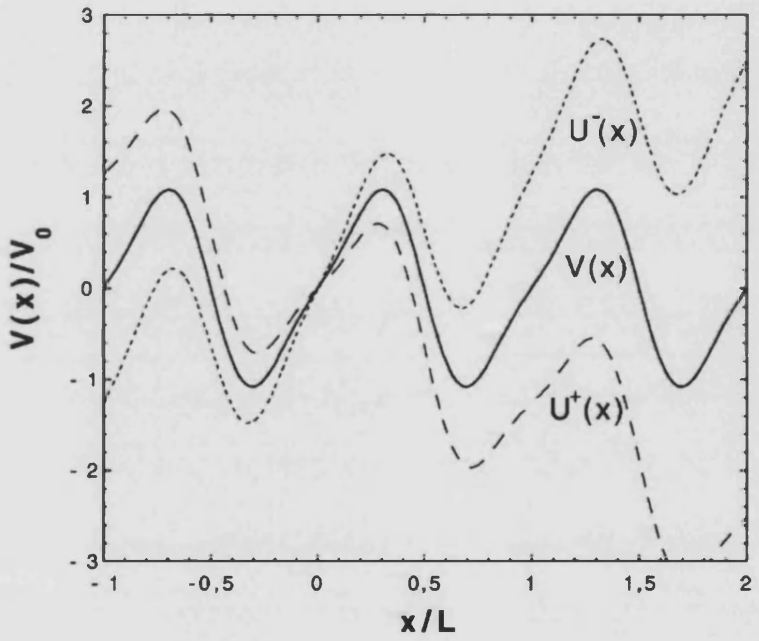

Figure 3.3: The tilting ratchet considered by Reimann [41]. It is clear to see that the potential and the tilting are of zero average and time periodic. One can also note that in tilting it is not just the barrier height that is affected: the barrier thickness also oscillates in magnitude.

on the height of the barrier but also the barrier's shape. Since, under tilting, the barrier width is less for a tilt to the left, the tunnelling probability is greater and a net negative tunnelling current is expected. Above a certain critical temperature, quantum mechanical tunnelling becomes rare, so the escape over the barrier dominates the dynamics and in agreement with the classical theory, a positive current results but enhanced in magnitude. As the temperature is reduced below the critical temperature, a point is reached where tunnelling effects dominate and the current is inverted. This current reversal is a very robust physical mechanism and as such it would be expected to be readily experimentally observable.

The experimental evidence of this effect was first shown by the Linke Group in their experiments in a semiconductor ratchet for electrons, [90, 91, 93, 95]. The group created an asymmetric conducting channel by etching trenches into a GaAs/AlGaAs hetrostructure. The channel shown in figure 3.3 acts as a wave-guide, an electron in the channel sees the double saw-toothed patterns as asymmetric energy barriers. A current in the channel is induced by a bias voltage and is determined by the reflection and tunnelling coefficients of the barriers. The barriers are themselves deformed in a way that depends on the direction of the applied electric field and since the tunnelling probabilities are dependent on the barrier shape, a net current can be generated with an alternating electric field. The experiment is set up such that the probabilities of escaping over the barriers and tunnelling through them are comparable, resulting in the current direction being highly temperature dependent.

Quantum Brownian ratchets have been observed experimentally in different contexts, including, the directed motion of vortices in a superconductor. The vortex patterns formed in many superconductor experiments are induced by fields as small as the earth's magnetic field. These vortices substantially hinder experiments as once present, they dissipate energy and create internal noise which can inhibit the operation of many superconductor devices. So a method for removing such vortices is greatly welcomed. It would seem the answer may lie in the application of a ratchet potential, [104]. When a superconductor is patterned with an asymmetric saw-tooth pinning potential, which is obtained by varying the sample thickness, the vortices will move along the potential in the presence of a directed current. If the current

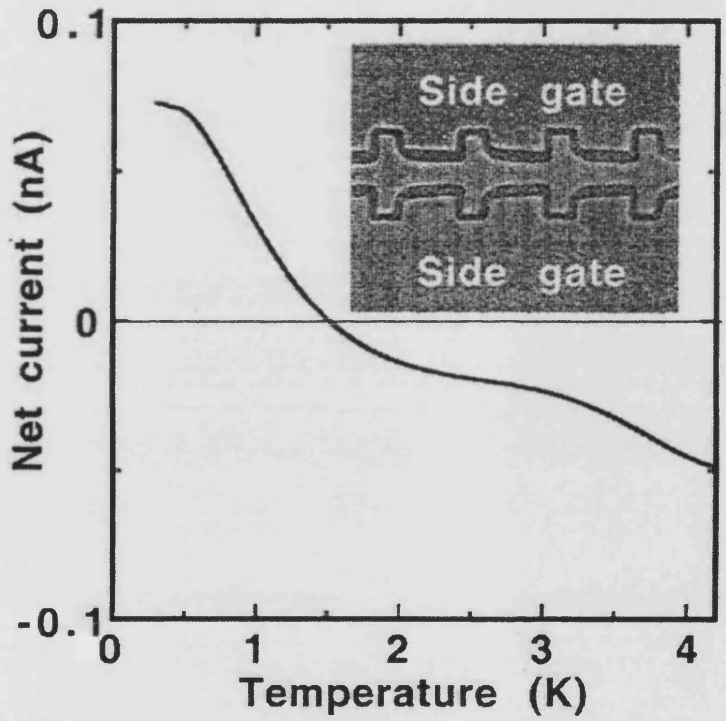

Figure 3.4: The experimental realisation of the tunnelling ratchet produced by the Linke group [90]. Inset is an image of the semiconductor channel used in the experiment, the dark regions representing the etched asymmetry waveguide. The graph clearly shows a current reversal as the temperature is reduced due to the increasing contribution of the tunnelling current.

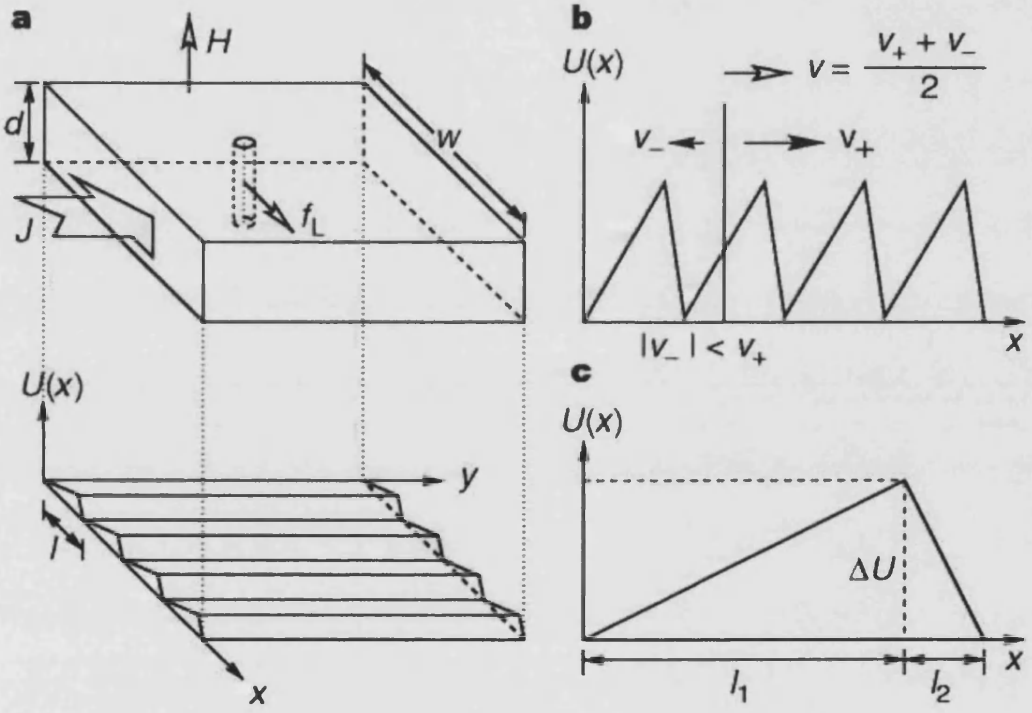

Figure 3.5: Vortices caused by small magnetic field effects, can be removed from a superconductor by the application of an alternating current in the direction perpendicular to the asymmetry in the pinning potential. A net current results as the vortex velocity in the positive x direction is greater than that in the negative x direction because of the asymmetry of the potential. The potential is created by varying the depth of the superconductor d. [104]

direction is in the positive y direction (see fig. 3.4 above) the vortices move in the positive x direction, when the current is reversed the direction of the vortex motion is reversed. However, the magnitude of the vortex velocity in the negative x direction is smaller than that of the positive x direction due to the asymmetry of the potential, so, by applying an alternating current a net vortex motion can be achieved with a velocity $v = (v_+ + v_-)/2$ in the positive x direction. Furthermore, superconducting vortex ratchets have also been used to demonstrate the temperature dependent current inversions predicted by Reimann *et al* [82].

3.4 Deterministic Ratchets

From the noisy and dissipative regime of the Brownian motor, the next step in the evolution of ratchet concepts came by stripping the models down to their simplest forms and removing noise completely. This is the deterministic ratchet. As a further step the case of vanishing dissipation, i.e. Hamiltonian dynamics, is of great interest. The system equation can now take the form for a general deterministic ratchet,

$$m\ddot{x} = -V'(x(t)) - \gamma\dot{x} + y(t) \tag{3.23}$$

where the function $y(t)$ provides a rocking as before and γ is the frictional term which vanishes in the case of Hamiltonian dynamics. $V(x)$ is again spatially periodic.

The re-inclusion of the inertial term $m\ddot{x}$ for both the dissipative and Hamiltonian regimes allows the system to exhibit chaotic behaviour and as such brings with it new theoretical considerations. Due to the complex nature of chaotic systems, for example, phase space islands, stochastic layers and KAM tori, many of the system dynamics are dependent on initial conditions. However, in the case of strong system perturbations leading to global chaos, novel and generic phenomenon can be observed. The combination of the well understood field of diffusive transport with the idea of directed transport shows new robust physical mechanisms.

In comparison to the mountain of work done on the subject of Brownian ratchets, there has been little on their deterministic counter parts. One of the most noteworthy

studies was carried out by Flach *et al* [52], where the system was studied by inspecting various symmetry properties. The group showed that the correct lowering of the system symmetries can lead to a nonzero dc current and argued that even lowering the symmetry of $y(t)$ alone can give this result. While this system has been studied by many groups, in general, harmonic functions have been considered for $V(x(t))$ and $y(t)$ and it is this choice of symmetry that leads to zero current. The group defined system symmetries such that for $f(x) = V'(x)$,

$$\hat{f}_a : f(x+\chi) = -f(-x+\chi), \tag{3.24}$$

$$\hat{y}_s : y(t+\tau) = y(-t+\tau), \tag{3.25}$$

and

$$\hat{y}_{sh} : y(t) = -y(t+T/2). \tag{3.26}$$

Where T is the time period of the system, χ and τ are appropriate origin shifts. If the system is invariant for the transformations,

$$\hat{S}_a : x \mapsto (-x+\chi), t \mapsto (-t+T/2) \tag{3.27}$$

and,

$$\hat{S}_b : t \mapsto (-t+\tau), \tag{3.28}$$

then all trajectories subject to the above symmetries in a stochastic layer will remain in the layer with a zero time averaged velocity. The group go on to show numerically that if the symmetries are not present, then the above does not hold and that nonzero time averaged velocities result. The effect is attributed to desymmetrization of Levy flights in the positive and negative directions. Furthermore, the current can be inverted in the dissipationless case by applying the substitutions $t = -t$ or $x = -x$ and $y(t) = -y(t)$. In the case where $\gamma \neq 0$ only the symmetry transformation $\hat{S}_a$ is possible (as the dissipation acts to break time reversal symmetry) and when present, zero current results. For every trajectory there is a counter moving partner. In the instance when the symmetry $\hat{S}_a$ is broken, the resulting current can be reversed under the operation $V(x) = -V(-x)$ and $y(t) = -y(t)$ only.

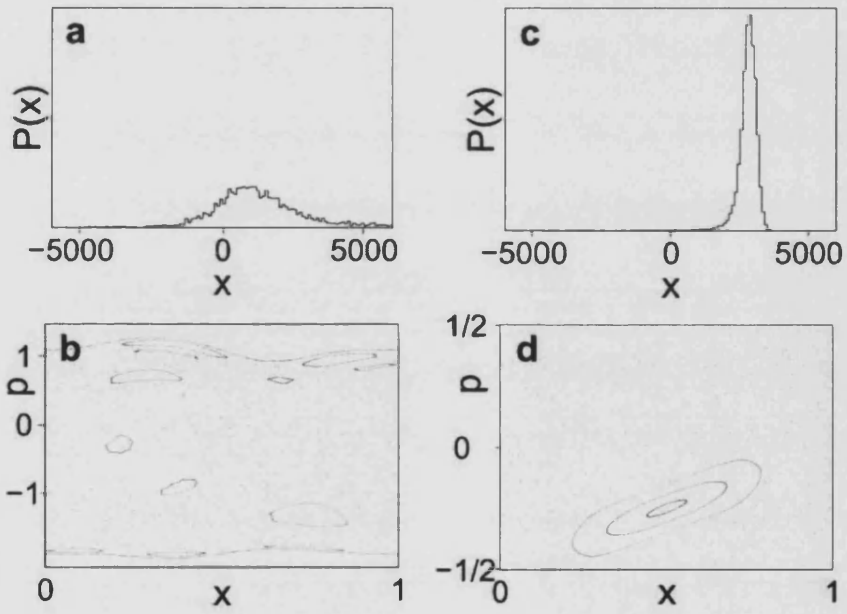

Figure 3.6: (a) Spatial distribution of a classical ensemble of particles after 20,000 kicks for a driven system, (b) the corresponding phase space plot, where the upper and lower limits are KAM tori. (c) and (d) are the same for a kicked system, with $V'(x) = (x - 0.5)\mathbf{mod}1$ and $T'(p) = \mathbf{Sgn}(\sin 2\pi p + 3/(2\pi)\cos 2\pi p)$ from [54]

Another block of important work has been carried through by the Dittrich group in Germany, [53, 54]. This group's approach was to analyse both the regular and chaotic regions of phase space and determine the transport characteristics for each one. The resulting classical and quantum sum rules give excellent insight into the detailed structure of the dynamics of Hamiltonian ratchets. The group analysed a time periodic system of the Hamiltonian form,

$$H(x,p,t) = T(p) + V(x,t), \tag{3.29}$$

where $T(p)$ is the kinetic energy and the potential has the features of time periodicity, $V(x,t+T) = V(x,t)$, and a periodic spatial derivative in x, $V'(x+X,t) = V'(x,t)$. The group considered the system in the regime of mixed phase space, i.e. a phase space that is made up of regions of both chaotic and regular dynamics. Due to the conservative nature of Hamiltonian systems, the transport features of finite invariant regions of phase space were studied and for such a region, the ballistic transport is defined as phase space volume times the average velocity of the phase space area. As such it can be written,

$$\tau_M = \int_0^T dt \int_0^x dx \int_{-\infty}^{+\infty} dp \chi_M(x,p,t) \frac{\partial H}{\partial P}. \tag{3.30}$$

Here, χ_M is the characteristic function of the invariant section of phase space M. Now the total transport for all the invariant phase space regions can be summed,

$$\tau_M = \sum_i \tau_{M_i}. \tag{3.31}$$

The regular regions of this mixed phase space was assumed to be made up of only regular islands for simplicity. So treating each island as an invariant region in phase space, the ballistic transport for the regular region of the phase space is,

$$\tau_i = A_i v_i. \tag{3.32}$$

The area A_i is the island area in a stroboscopic surface of section plot and the average velocity v_i of that island is given by the winding number of the stable fixed point at the islands centre, $\omega_i = x_i/t_i$. Before the onset of global chaos and the destruction

of the last KAM surface, chaotic regions of phase space are typically bounded by two KAM tori forbidding any trajectory started within from escaping. The bounded region between these KAM surfaces can be considered as a large invariant area in phase space itself and as such its transport can be calculated. This can be shown to be the difference between the average kinetic energies of the two bounding tori and written as $\langle T\rangle_a - \langle T\rangle_b$. Now a point has been reached where the transport for the chaotic region of the phase space can be written down as the total transport of the stochastic layer minus the regular transport of the embedded islands [54].

$$A_{ch}v_{ch} = \langle T_a\rangle - \langle T_b\rangle - \sum_i A_i\omega_i. \tag{3.33}$$

In [54] the predicted theoretical values for the chaotic drift agree well with numerical results obtained by evolving many trajectories over a long time period. The group also showed for a δ-kicked system with $V'(x) = (x - 0.5)\mathbf{mod}1$ and $T'(p) = \mathbf{Sgn}(\sin 2\pi p + 3/(2\pi)\cos 2\pi p)$ that if the initial starting conditions were evenly spread over the entire unit cell, zero net transport (i.e. no not current in either direction) would result. Therefore, for these system parameters the regular and chaotic regions cancel each other.

$$A_{ch}v_{ch} + A_{reg}v_{reg} = 0. \tag{3.34}$$

The group also derived a quantum mechanical counterpart to their classical sum rule. This was achieved by considering the Floquet band structure of the system and once again centred around the invariants of the dynamics which satisfy the Bloch-Floquet conditions. The quantum transport for the system is related to the expectation values of the stationary states. These velocities can be written in terms of the band slopes,

$$v_{\alpha,k} = \int dk \sum_\alpha |\psi_{\alpha,k}|^2 \frac{\partial \epsilon_{\alpha,k}}{\partial k}, \tag{3.35}$$

where $\epsilon_{\alpha,k}$ is the quasi-energy and k the quasi-momentum. Now, transport can be analysed in terms of the spectral properties and through band diagrams.

The group showed that in the diabatic regime, the band diagram has two sets of bands, straight (negatively) sloping bands attributed to regular islands and spaghetti like bands for the chaotic regions of phase space. In the adiabatic limit (fine detail)

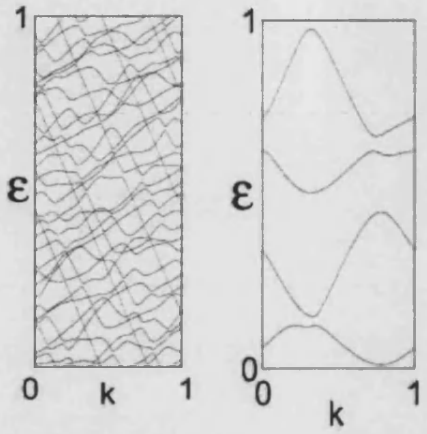

Figure 3.7: The band structure of the quantum mechanical system, on the left panel the diabatic case with band crossings. The regular invariant islands are represented by the straight strongly sloping lines, the chaotic regions by the spaghetti style lines. The average gradient of each group represents its transport velocity. On the right the avoided crossings of the adiabatic case.

all band crossing are avoided and hence the sum of gradients over all bands is zero. Each band can be associated with a winding number according to its gradient, with the sum of all winding numbers being also zero. Moving from the adiabatic to the diabatic regime conserves winding numbers and hence once again the quantum chaotic drift current can be calculated through a sum rule as the regular bands have a finite gradient in the diabatic regime.

$$\sum_{\alpha} \omega^{ch} + \sum_{\alpha} \omega^{reg} = 0. \tag{3.36}$$

Work concerning the nature of current reversals in deterministic ratchets has been completed by Mateos [38]. He found that current reversals in his system correspond to bifurcations in the system's period doubling route to chaos. The system which was studied is represented as,

$$\ddot{x} + b\dot{x} + V'(x) = a\cos(wt). \tag{3.37}$$

The parameters b and w were held constant while a was varied. It was shown that the

system underwent current reversals as a was increased, furthermore, these reversals were observed to occur at the same values of a as the bifurcations. It was shown that in the periodic regions of the bifurcation diagram the trajectories were in *running modes* which had certain constant momentum values. Near the bifurcation, the orbit intermittently behaves periodically, broken up by short times of chaotic motion, as the bifurcation is crossed, the orbit becomes truly periodic and has directed motion in a given direction (negative for the four period orbit). As these *running modes* were switched on and off with increasing a the current produced by the system jumped between different levels. This is described as precisely the mechanism by which the current reversal takes place.

In the next few chapters a new mechanism for directed transport in a Hamiltonian ratchet is introduced. This mechanism operates purely in the fully chaotic regime and therefore requires no specific dynamic phase space features and the ability to produce directed transport is independent of starting conditions. The model is fully consistent with the sum rules of the Dittrich group and the symmetry arguments of the Flach group. The model displays current reversals which are dependent on system parameters and which are explained in terms of the momentum diffusion of the system.

Chapter 4

Classical Theory

4.1 Introduction

The main focus of this thesis is in presenting a model for clean atomic transport. The model presented is a new type of Hamiltonian ratchet and will be known as the chirped double well classical kicked rotor (CDW-CKR). The motivation for the system springs from the recent series of experiments in optical lattices involving kicked and driven systems which were outlined in chapter 2. The model proposed is experimentally realisable due to the possibility of asymmetric optical lattice potentials which can be pulsed on and off and as such the system is an on-off ratchet as explained in chapter 3. This Hamiltonian model is studied for high values of the stochasticity parameter, so, it is in the completely chaotic regime and therefore does not rely on any specific preparation of islands and/or tori in its phase space. The system is a kicked system in nature and can be seen as an extension of the standard map. However, in line with all other ratchet models the system symmetries have been lowered. In this instance both time (by chirped series of kicks) and spatial symmetries (asymmetric double well) have been broken. This is the first system to rely on a ratchet mechanism of preferred diffusion - whereby the diffusion of atoms with positive and those with negative momentum are uneven up to a finite time, the ratchet time, t_r. The dynamics of the system are explored in both the classical and quantum regimes and in later chapters comparisons between the quantum and classical are explored. In

this chapter the model is presented classically.

4.2 Symmetry

As discussed in detail in chapter 3 when considering a ratchet system a necessary condition for a non-zero particle current is the lowering of one or more of the model's symmetries. In the CDW-CKR, time reversal symmetry is broken; $f(t) \neq f(-t)$. Also spatial symmetries are broken such that $V(x) \neq V(-x)$. The CDW-CKR also does not fall into the group of system which are super-symmetric [41], whereby a combination of symmetry breaking conditions leads to a zero net dc current.

4.2.1 Spatial Symmetries

The spatial symmetries of the system are broken by means of an asymmetric double well potential. This potential is an approximation (to the second harmonic) of a *saw-tooth* potential seen in many ratchet systems. The potential can be written as follows;

$$V(x) = \sin(x) + a\sin(2x + \phi) \tag{4.1}$$

The variable a, is the ratio of the relative strengths of each harmonic component and ϕ is the relative phase difference between them. The potential is clearly periodic in x, such that for the correct value X and any integer n,

$$V(x) = V(x + nX). \tag{4.2}$$

Figures 4.1 and 4.2 show some of the variations possible with this simple potential set-up.

This potential is pulsed on and off by a delta function. The amplitude of each *kick* is defined by a stochasticity parameter K, the kicking strength. In order to relate back to the kicked rotor model an effective kick strength is defined K_{eff}, where:

$$K_{eff} = K\sqrt{1 + 4a^2} \tag{4.3}$$

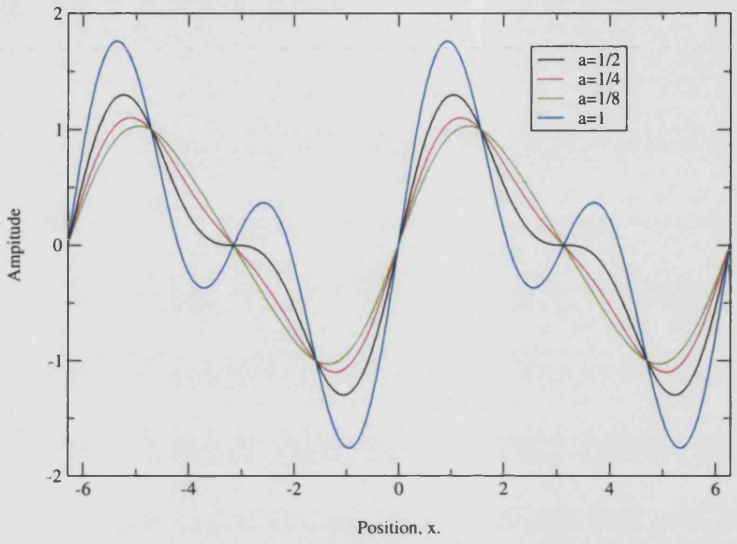

Figure 4.1: Potential surfaces for the CDW-CKR for various values of the parameter a. $a = 1$ shows very pronounced double well formation (blue line) while a saw-tooth potential is better approximated by $a = 0.25$ (red line). For all curves $\phi = 0$

where neglecting all classical correlation terms, the diffusion constant is calculated to be $D \sim D_0 = K_{eff}^2/2$. Hence the quasi-linear diffusion rate analogous to the kicked rotor is regained, see equation (2.6).

4.2.2 Temporal Symmetries

The time reversal symmetry of the model is broken by means of using a repeating *chirped* sequence of delta kicks as opposed to the equal kick spacing in the kicked rotor model. For a value j, an integer greater than one and b, a small time perturbation, the time intervals between kicks in a $2j+1$ kick cycle can be written down as follows,

$$1 + jb, 1 + (j-1)b...., 1 - (j-1)b, 1 - jb. \tag{4.4}$$

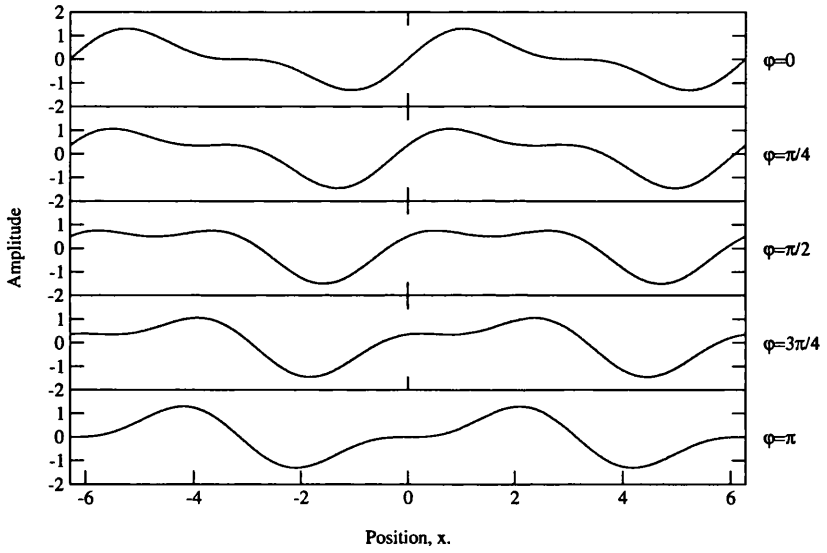

Figure 4.2: Diagram showing how the direction of the ratchet *teeth* can be altered by varying phase. For typical on-off ratchet dynamics, figure 3.2, the direction of the particle current could be expected to reverse for changes in phase from $\phi = 0$ to $\phi = \pi$. Note that the potential becomes symmetric for $\phi = \pi/2$ and anti-symmetric for $\phi = 0$.

The overall time period in the model is the sum of all the kicks in a cycle,

$$T_{tot} = \sum_{i=1}^{j} T_i. \tag{4.5}$$

The time is rescaled such that over each cycle the average time between kicks, T, is unitary: $\langle T_i \rangle = 1$. This gives $T_{tot} = N$ without a loss of generality. The number of kicks in a cycle, N, is $N = 2j+1$, for N odd and $N = 2j$ for even N. So for example for $N = 3$, the repeating cycle of kicks are spaced as: $T_1 = 1 + b, T_2 = 1, T_3 = 1 - b$. For $N = 2$ the cycle is: $T_1 = 1 + b/2, T_2 = 1 - b/2$.

Now, the chain of delta kicks can be written down as the double summation,

$$f(t) = \sum_{n=0}^{\infty} \sum_{M=1}^{N} \delta(t - (nT_{tot} + \sum_{i=1}^{M} T_i)) \tag{4.6}$$

So in the sequence the first delta kick comes at time T_1 the next at $T_1 + T_2$ the next at $T_1 + T_2 + T_3$, in a three kick cycle ($N = 3$) the fourth kick would come at time $T_1 + (T_1 + T_2 + T_3)$.

4.3 Classical Scaling and the Hamiltonian

The motivation for the study of the model initially came from an atom-optics point of view as mentioned in earlier sections. Therefore in defining the Hamiltonian for the system I will start from an atom-optics stand point. It can be shown (see section 6.1 and [67]) that the Hamiltonian for an atom in a kicked optical lattice can be written in the form,

$$H(x, p, t) = \frac{p^2}{2M} + V_0 F(t, 2k_L x) \tag{4.7}$$

where momentum and position take their normal notation x, p and k_L is the wavenumber of the standing wave of laser light of frequency ω_L. V_0 is the intensity of the laser potential and M is the atomic mass. The function F represents the potential and incorporates both time and space dependencies.

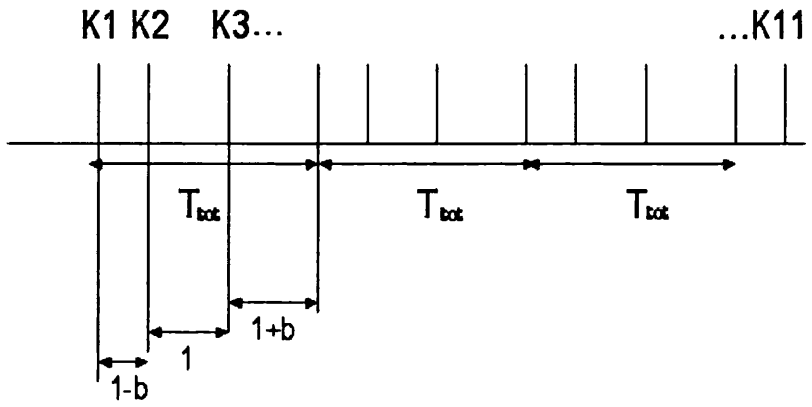

Figure 4.3: Schematic diagram of the time intervals between successive kicks. Shown are the first 11 kicks of a sequence for $N = 3$ with the first three intervals labelled for the first complete time period.

The classical dynamics represented by the above Hamiltonian appear to depend on three separate parameters: M, V_0, k_L. For a study of the system dynamics and the onset of chaos each of the parameters would have to be varied in turn along with the time between consecutive kicks. This would require a very large parameter space to be explored. However, due to re-scaling of the Hamiltonian to dimensionless units it can be shown that the classical dynamics only depend on one re-scaled parameter which is a combination of all the above. This is achieved by introducing the following scaling transformations;

$$t : T\tau \tag{4.8}$$

$$x : \frac{x'}{2k_L} \tag{4.9}$$

$$p : \frac{p'M}{2k_L\tau}. \tag{4.10}$$

So, after substitution into the Hamiltonian (4.7),

$$H = \frac{M}{8k_L^2T^2}p'^2 + V_0F(\tau, x') \tag{4.11}$$

which can be re-written with a re-scaled energy,

$$\frac{p'^2}{2} + KF(\tau, x') = \epsilon \tag{4.12}$$

where $\epsilon = 8\omega_r T^2 H/\hbar$ and $\omega_r = \hbar k_L/2M$ and is the atomic recoil frequency.

After dropping primes and approximating the short pulse of an experiment by a delta kick, the classical Hamiltonian for the system is written,

$$H(p, x, \tau) = \frac{p^2}{2} + KV(x)f(\tau), \tag{4.13}$$

where $V(x)$ is defined in section 4.2.1. and $f(\tau)$ is given by equation (4.6) before re-scaling.

4.3.1 The Map

The Hamiltonian (4.13) is solved to give an iterative map, like the kicked rotor, by considering the free evolution and kick separately. So, Hamilton's equation for the model are written as,

$$\frac{\partial H}{\partial p} = \dot{x} = p \tag{4.14}$$

and,

$$\frac{\partial H}{\partial x} = -\dot{p} = KV'(x)f(\tau). \tag{4.15}$$

The kicking part of the evolution (4.13) is solved by integrating over a small dimensionless time interval $2\Delta\xi$. This interval starts just before and finishes just after the kick to give an expression for the change in momentum. For the nth kick from $n\langle T\rangle - \xi$ to $n\langle T\rangle + \xi$.

$$\Delta p = -KV'(x)\int_{n\langle T\rangle-\xi}^{n\langle T\rangle+\xi} f(\tau)d\tau. \tag{4.16}$$

The delta kick is an instantaneous process, therefore no change in position results across the kick. In the free evolution between each kick, of duration T_i, the change in the position variable is written simply as,

$$\Delta x = pT_i. \tag{4.17}$$

The discrete mapping for the system can now be written,

$$p_{n+1} = p_n - KV'(x) \tag{4.18}$$

$$x_{n+1} = x_n + p_{n+1}T_i, \tag{4.19}$$

where n implies the kick number and $V'(x) = \partial V/\partial x$ and i is the ith kick of the N kick sequence. So for the CDW-CKR the mapping for the first kick in a three kick chirp sequence is written as,

$$p_{n+1} = p_n - KV'(x_n), \tag{4.20}$$

$$x_{n+1} = x_n + p_{n+1}(1+b). \tag{4.21}$$

4.4 Phase Space Features

The dynamics of the above map are, like the kicked rotor, explored through surface of section plots. The phase space plots can be used to investigate the system's transition to global chaos and any features of the system such as the existence and position of regular islands, KAM tori, accelerator modes etc. In the following sections, surface of section plots are presented for varying system parameters to show their effects on the system dynamics.

4.4.1 Variation of the Effective Kick Strength

Here the effective stochasticity parameter K_{eff} is varied. Starting at very low kicking strength (figure 2.4a) the phase space of the system is almost entirely regular, with only very narrow stochastic regions trapped between invariant KAM tori. The phase space bears close resemblance to a completely unperturbed system, where all tori are flat and there are no chaotic areas of phase space. The next plot is for a mixed phase space where there are still many regular islands and intact KAM tori, so initial trajectories cannot explore the whole phase space and are limited to stay between their nearest two bounding KAM tori. Moving further right and still in the regime of mixed phase space, the surface of section plot is for a value of $K_{eff} = 0.6$ where

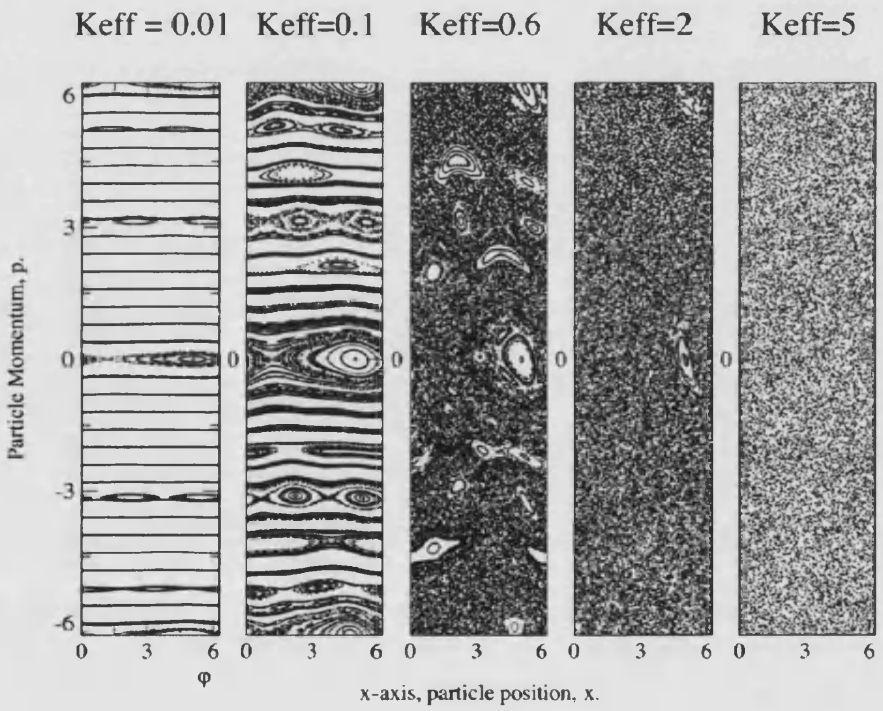

Figure 4.4: Five surface of section plots as the effective kick strength is varied from $K_{eff} = 0.01$ until $K_{eff} = 5$ going from left to right. $b = 0.1$, $a = 0.5$, $\phi = 0$

the last KAM torus has just been destroyed. Note that both in (b) and (c) not all islands in the positive momentum phase space have a matching island in the negative momentum phase space. This is as a result of the lowered system symmetries - not all trajectories have a counter moving partner. The next phase space is for $K_{eff} = 2$ and is largely chaotic. Most of the area is taken up by the chaotic sea. Finally in the last plot the kicking strength is such that phase space is almost entirely chaotic with only minute islands still existing.

4.4.2 Amplitude ratio of potential harmonics

In figure 4.5, the ratio of the two components of the potential, a, is varied. While for values of a from 2 until 1/2 there is little difference in the phase space features, it is clear to see that as the second harmonic (the $\sin(2x + \phi)$ term) is reduced and eventually switched off (4.5e) the phase space becomes more regular (there are more intact tori) despite the effective kicking strength K_{eff} remaining a constant throughout.

4.4.3 Relative phase of potential harmonics.

In figure 4.6 the phase difference between the two terms in the potential is varied from $-\pi$ to π. Here in figure 4.6c there is less matching between phase space islands in positive and negative regions of the phase space, especially relative to figures 4.6a and 4.6e where all islands in the positive momentum space are very well matched in terms of size to their counter propagating negative momentum counter parts.

4.4.4 Phase-Space Structure as a Function of N

In this section, the effect of varying N, the number of kicks in the sequence, on the classical phase space features is examined. There is a very clear pattern: For $N = 1$ there is no time asymmetry and the phase space looks quite regular, KAM tori still exist and as such phase space is mixed but bounded. For figure 4.7b where there are two kicks in the sequence, time symmetry is still not broken, but the dynamics are

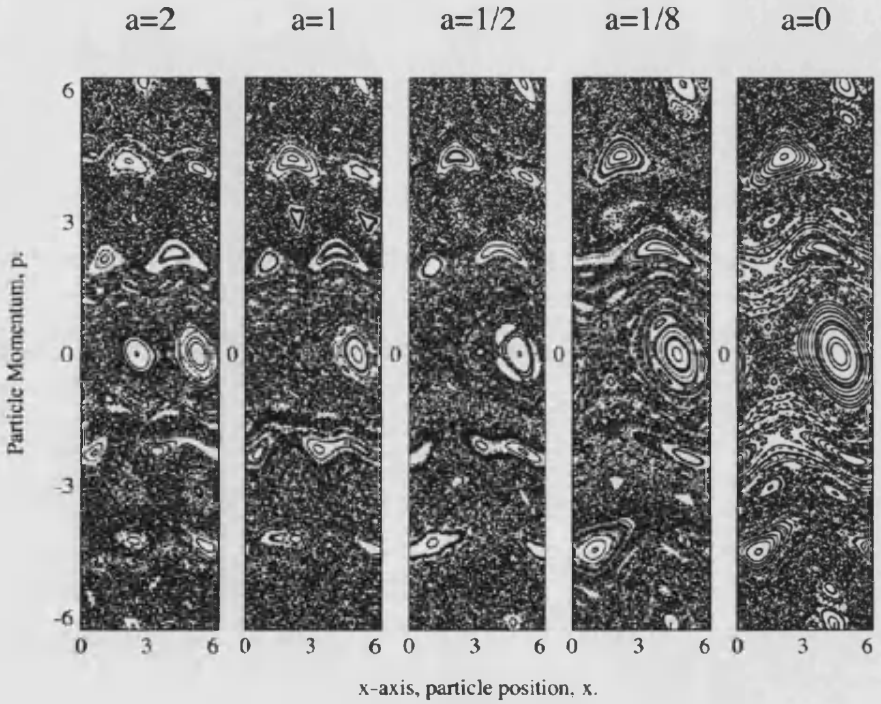

Figure 4.5: phase space diagrams for the CDW-CKR as a is changed from values on the left where $a = 2$ and the second harmonic has the biggest contribution in the potential until the second harmonic is completely removed at $a = 0$. Other parameters are all kept constant; $b = 0.1$, $K_{eff} = 0.5$, $\phi = 0$

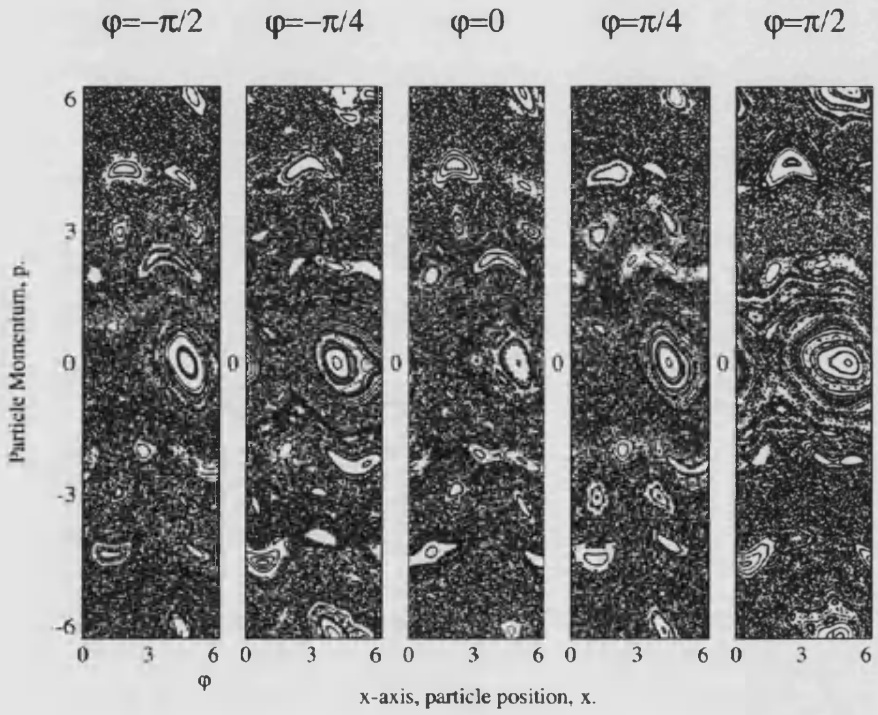

Figure 4.6: Surface of section plots showing phase varied, while $a = 0.5$, $K_{eff} = 0.5$, $b = 0.1$ are kept constant.

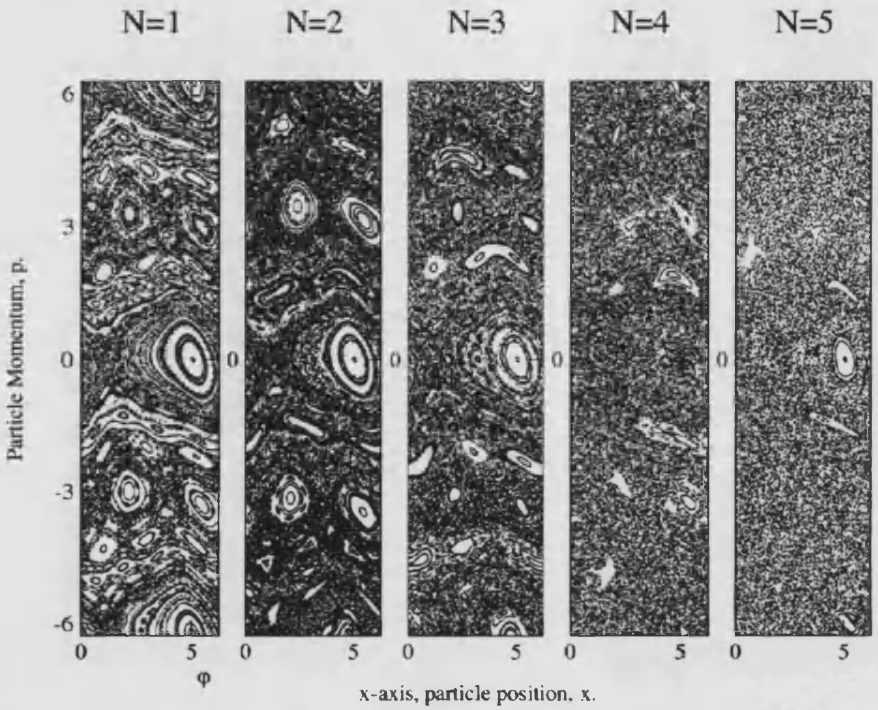

Figure 4.7: Surface of section plots as the number of sequence kicks, N, is increased. $\phi = 0$, $b = 0.1$, $a = 0.5$.)

already comparably more chaotic. As the value of N is increased still further, time reversal symmetry is broken after $N = 3$ and for every additional kick in the sequence the phase space becomes more chaotic. This can be explained by considering that for a sequence with a high value of N there are more kicks separated by long time intervals, for example, for $N = 5$, $T_5 = 1+2b$. The time between kicks can be mapped onto the kick strength for the next kick in the sequence and as a result a longer time between two adjacent kicks is equivalent to a higher effective kicking strength. While there are also the same number of kicks with smaller time separations it is those with a high effective stochasticity parameter that allow the trajectories to explore the full range of the phase space.

4.4.5 Kick separation, b

Once again, there are obvious trends in the phase space plots in figure 4.8. Starting at 4.8b, with the parameter b set to zero, the time reversal symmetry remains intact. As a result, the system bears a closer resemblance to the standard map and is far more regular than at other values of b for the same K_{eff}. As b is increased once again the system tends more and more towards the totally chaotic phase space and to an increasing extent, not all islands can be matched to their counter propagating partners. An important point of interest is the comparison between figures 4.8a and 4.8d, which show very similar features of their phase space, only reversed in momentum. It will be shown later in this report that b is one system parameter that can be used to generate a current reversal. It should also be noted that the phase space periodicity in momentum scales with b for rational values of this parameter. This can be seen by examining the map where b is represented by M/N in a similar way to Cheon *et al*, [55]. Here, M and N are both integer numbers, so b is a rational number,

$$x_{n+1} = x_n + p_{n+1}(1 + M/N), \tag{4.22}$$

$$p_{n+1} = p_n - KV'(x_n). \tag{4.23}$$

From direct substitution of $p_n \mapsto p_n + 2N\pi$, it is straight forward to see,

$$x_{n+1} \mapsto x_{n+1} + 2(M + N)\pi \tag{4.24}$$

so, as there is a 2π periodicity in x, for integer $N + M$ there is a $2\pi\beta$ periodicity in momentum, where β is defined $1/\beta = M/N$. Therefore, the periodicity of momentum scales as $2\pi\beta = 2\pi/b$, an inverse relationship with b.

4.5 Is there a Ratchet?

Now that the classical phase space has been presented in detail, the next question to answer is whether a non-zero current does result from the broken symmetries despite the absence of any noise or dissipation. In figure 4.9 an ensemble of 300,000 trajectories were started along the line $p = 0$ between values in x of $0, 2\pi$. The

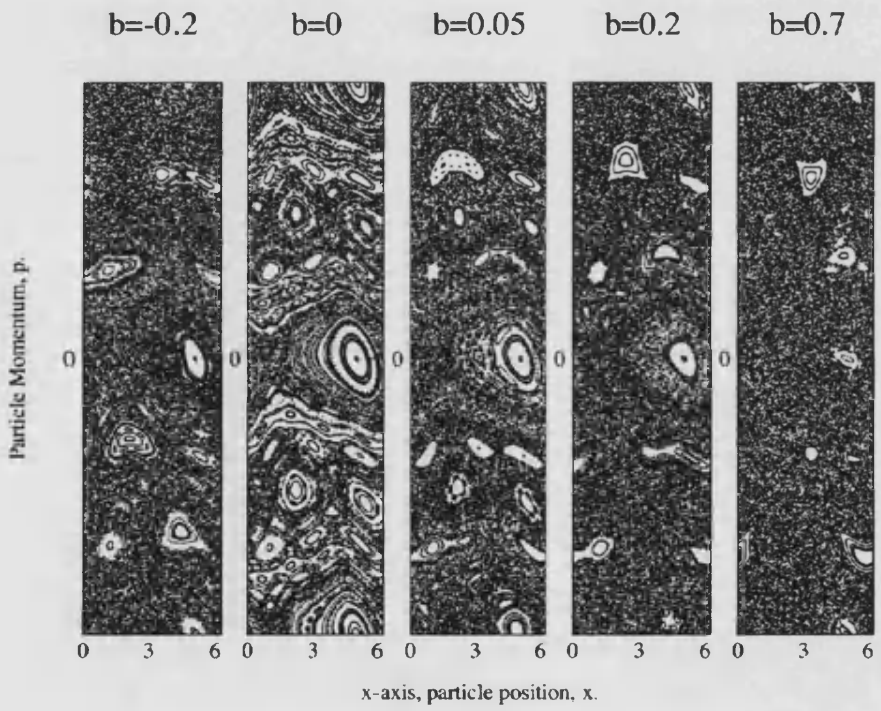

Figure 4.8: The time perturbation , b, the amount by which the kicks are moved from an even time spacing is studied via the phase space. $\phi = 0$, $a = 0.5$, $K_{eff} = 0.5$.

particular system setup these trajectories were subjected to was one of a three kick sequence with the small time perturbation $b = 0.1$. The average energy and the ensemble average momentum are displayed and it is strikingly clear that the system is indeed a ratchet. The presence of non-zero current, which is constant after a finite time, was found to be a generic effect: it is not only independent of specific dynamical features of the phase space, but exhibits current reversals for varying control parameters. Such control over the current produced in such a system could prove useful for devices based around the model.

4.5.1 Ratchet Mechanism

The mechanism by which the system produces the ratchet effect relies on an uneven diffusion in momentum. For a finite time, the positive and negative momentum trajectories of the system gain energy at different rates. This lasts up to the ratchet saturation time t_r, which can be read from figure 4.9 as the point at which the average momentum flattens. This is further illustrated in figure 4.10 where for a similar ensemble as used in figure 4.9 the energy of the positive and negative momenta are plotted on two different curves with half of the total energy plotted between (red line). This figure clearly shows that negative momentum trajectories are gaining energy considerably faster than their positive momentum counter-parts at early time scales before the two lines later begin to draw parallel around 1500 kicks.

The diffusion formula for the ratchet is momentum dependent, in fact periodic in p. Locally, about $p = 0$, the diffusion is a decreasing function in p, this results in a preferred diffusion in the negative direction. For short time scales the distribution in p is subjected to this gradient in diffusion. Over long time scales, the distribution spreads over several periods in momentum and the effect becomes averaged out or saturated. The splitting in the positive and negative momentum seen in figure 4.10. To start with the energies split in a linear fashion before some averaging takes place as some of the trajectories explore a wide range of the phase space on their *random* walk. Full saturation is reached at t_r when the momentum distribution has a width significantly greater than the momentum period of the diffusion function.

An asymmetric potential $V(x)$ produces a momentum dependent diffusion which is not symmetric in p. Although a symmetric potential also leads to a periodic diffusion function, a wavepacket started at $p = 0$ would not exhibit a directed current as the trajectories would diffuse evenly away from their starting positions. A measurable ratchet effect would, however, be achievable with a carefully chosen non-zero starting position.

To gain some insight into how the momentum dependence of the diffusion arises a brief analysis of the mappings for the standard map and the ratchet are compared. This is before a more mathematically rigourous description of the diffusion formula follows in the remaining sections of this chapter.

So, from the mapping of the standard kicked rotor,

$$p_N - p_0 = \sum_{j=0}^{N-1} -V'(x_j) = \sum_{j=0}^{N-1} K \sin(x_j), \tag{4.25}$$

is it clear to see,

$$\langle (p_N - p_0)^2 \rangle = \langle (V'(x_0) + V'(x_1) \cdots V'(x_N))^2 \rangle. \tag{4.26}$$

The R.H.S of equation (4.26) gives terms like $(V'(x_j))^2$ which from equation (4.25) will average to $K^2/2$ since $\langle \sin^2(x_j) \rangle = 1/2$ for an ensemble of particles spanning a large range of x_j. The corrections to the diffusion constant come from the *cross terms* resulting from (4.26). For example $\langle 2V'(x_j)V'(x_k) \rangle$ is the correlation between kick j and kick k. Adjacent kicks are uncorrelated, for example consider,

$$\begin{aligned} \langle V'(x_0)V'(x_1) \rangle &= K^2 \langle \sin(x_0) \sin(x_0 + p_0) \rangle \\ &= \langle K^2 [\sin^2(x_0) \cos(p_0) + \sin(x_0) \cos(x_0) \sin(p_0)] \rangle. \end{aligned} \tag{4.27}$$

If an ensemble average is taken, with, for example, a Gaussian distribution in x and p which is not too narrow (which would be typical after a small number of kicks), then, $\langle \cos(p_0) \rangle$ and $\langle \sin(p_0) \rangle$ both average to zero. Hence, the adjacent kicks provide no correction to the diffusion.

The 2-kick correlations, however, for example $\langle V'(x_0)V'(x_2) \rangle$, do produce non-zero corrections. It is straightforward to see that terms in $\cos^2 p$ and $\sin^2 p$ result

for the 2-kick average. Since both $\langle \cos^2 p \rangle$ and $\langle \sin^2 p \rangle$ are $1/2$ there are non-zero correlations. The average over x yields a second order Bessel function $= J_2(K)$ for the two kick correction.

So why is there a p-dependent correction in the ratchet? By considering the mapping of the CDW-CKR it is clear to see that the introduction of the uneven kicks allows an additional free evolution for a small distance $p_i b$. Hence, there are now corrections which depend on the sign of p and scale with b and (for short time scales at least) $D(p)^- \neq D(p)^+$. The mapping for the CDW-CKR is written,

$$x_{i+1} = x_i + p_i(t_{i+1} - t_i), \tag{4.28}$$

$$p_{i+1} = p_i - KV'[x_i], \tag{4.29}$$

where $(t_{i+1} - t_i)$ is the time between consecutive kicks which is no longer always unity.

Instead of the $\cos^2 p$ and $\sin^2 p$ terms in the standard map, for the ratchet we have terms of the type,

$$\begin{aligned} \langle \cos(p(1+b)) \cos(p) \rangle &= \langle \cos^2 p \cos pb - \sin p \cos p \sin pb \rangle \\ &\simeq \langle \frac{1}{2} \cos pb \rangle \\ &\simeq \frac{1}{2}. \end{aligned} \tag{4.30}$$

Here, $\cos^2 p$ oscillates fast compared to $\cos pb$ which for small $b \propto 0.05$ is approximately constant, $\cos pb \sim 1$. There are also terms like;

$$\begin{aligned} \langle \sin(p(1+b)) \cos(p) \rangle &= \langle \sin^2 p \sin pb + \sin p \cos p \cos pb \rangle \\ &\simeq \frac{1}{2} pb. \end{aligned} \tag{4.31}$$

This term produces the ratchet effect and carries the p-dependence of the 2-kick correlations. It is argued that while terms such as $\sin^2(p)$ will be quickly averaged away after only a few kicks, the terms with the much smaller arguments $\sin^2(pb)$, will not average so quickly and for short time scales, smaller that the ratchet saturation time, the small angle approximation holds. While this argument provides insight into the origin of the ratchet, a more formal, mathematically rigourous approach is possible and is outlined in the next section.

4.5.2 The Ratchet Diffusion Constant

Through a more rigourous method it is possible to attach a time dependence to the diffusion in the ratchet, allowing more accurate estimates of the system saturation point and behaviour with various system parameters. Here, the derivation of the diffusion constant for the ratchet is outlined and given up to the first non-zero correction term, $C(2,p)$. This is done through a modified version of a method first demonstrated by Rechester and White [74]. Firstly, the simple case for the kicked rotor. From equation (4.25),

$$S_l = \sum_{j=0}^{l} K \sin(x_j), \tag{4.32}$$

so now one can write,

$$p_N = p_0 + S_{N-1} \tag{4.33}$$

$$x_N = x_{N-1} + p_N = x_{N-1} + p_0 + S_{N-1}. \tag{4.34}$$

Next, the probability distribution which gives the probability such that at time t, $x(t) = x$ and $p(t) = p$ is given by the function $G(x,p,t)$. At time $t = T$,

$$\begin{aligned} G(x_T,p_T,T) \;=\; & \sum_{n_T=-\infty}^{\infty} \cdots \sum_{n_1=-\infty}^{\infty} \int_{-\infty}^{\infty} dp_0 g(p_0) \int_0^{2\pi} dx_0 f(x_0) \int_0^{2\pi} dx_1 \int_0^{2\pi} dx_2 \\ & \cdots \int_0^{2\pi} dx_T \delta(p_T - p_0 - S_{T-1}) \delta(x_T - x_{T-1} - p_0 - S_{T-2} + 2\pi n_T) \\ & \cdots \delta(x_1 - x_0 - p_0 - S_0 + 2\pi n_1). \end{aligned} \tag{4.35}$$

Where $f(x_0)$ is the normalised distribution for x_0 and $g(p_0)$ is the normalized distribution for p_0. The T summations over n are due to the periodic boundary conditions imposed on x_i by the mapping. Following [74] the initial starting conditions are taken as $g(p_0) = \delta(p_0 - p_{in})$ and $f(x_0) = 1/2\pi$. An expression for the diffusion constant can be arrived at by starting with the definition,

$$D = \frac{1}{2T} \langle (p_T - p_0)^2 \rangle_T. \tag{4.36}$$

Now,

$$D = \frac{1}{2T} \int_0^{2\pi} dx_T \int_{-\infty}^{\infty} dp G(x_T,p_T,T)(p_T - p_0)^2. \tag{4.37}$$

By direct substitution the diffusion constant can be written as,

$$\begin{aligned} D &= \frac{1}{2T}\int_0^{2T} dx_T \sum_{n_1=-\infty}^{\infty} \cdots \sum_{n_T=-\infty}^{\infty} \int_0^{2\pi} \frac{dx_0}{2\pi} \int_0^{2\pi} dx_1 \int_0^{2\pi} dx_2(\cdots) \\ &\quad (S_{T-1})^2 \delta(x_T - x_{T-1} - p_{init} - S_{T-1} + 2\pi n_T) \\ &\quad \cdots \delta(x_1 - x_0 - p_{init} - S_0 + 2\pi n_1). \end{aligned} \tag{4.38}$$

The above expression can be somewhat simplified with the use of the Poisson summation formula,

$$\sum_{n=-\infty}^{\infty} \delta(y + 2\pi n) = \frac{1}{2\pi} \sum_{m=-\infty}^{\infty} \exp(imy). \tag{4.39}$$

and can be written as,

$$\begin{aligned} D &= \lim_{t\infty} \frac{1}{2T} \sum_{m_1=-\infty}^{\infty} \cdots \sum_{m_T=-\infty}^{\infty} \int_0^{2\pi} \frac{dx_0}{2\pi} \int_0^{2\pi} \frac{dx_1}{2\pi} \cdots \int_0^{2\pi} \frac{dx_T}{2\pi} \\ &\quad (S_{T-1})^2 e^{im_T(x_T - x_{T-1} - p_{init} - S_{T-1})} \cdots e^{im_1(x_1 - x_0 - p_{init} - S_0)} \end{aligned} \tag{4.40}$$

The simplest solution to the diffusion constant integral is the quasi-linear diffusion rate which neglects all correlations between neighbouring kicks. This is calculated by setting the values of all the $m_j = 0$ and recalling equation (4.32), it can be shown that,

$$D_{ql} \simeq \frac{K^2}{4}. \tag{4.41}$$

The corrections to this result come from considering terms with non-zero m_i or in physical terms by the consideration of the kick to kick correlations for the sequence. The integral in (4.40) can be solved by using the identity,

$$e^{\pm ik\sin(x)} = \sum_{n=-\infty}^{\infty} J_n(k) e^{\pm inx}, \tag{4.42}$$

whereby now the correction terms will appear as a series of Bessel functions. The most simple correction arises from considering 2-kick correlations i.e. correlations between kicks j and $j-2$, as argued above. This term is the lowest order correction and is derived by setting $m_i = \pm 1$ and $m_{i-1} = \mp 1$. The resulting correction term is then,

$$\begin{aligned} C_i(2) &= \frac{K^2}{2T} \int_0^{2\pi} \frac{dx_0}{2\pi} \int_0^{2\pi} \frac{dx_1}{2\pi} \cdots \int_0^{2\pi} \frac{dx_T}{2\pi} \\ &\quad \left\{ \sum_{j=0}^{T-1} \sin(x_j) \right\}^2 e^{i(x_i - x_{i-1})} e^{i(x_{i-1} - x_{i-2})} e^{i(S_{i-2} - S_{i-1})} \end{aligned} \tag{4.43}$$

where here $m_{i+1} = 1, m_{i-1} = -m_i$ and $i = 2, 3..., T$. Noting that $S_{i-1} - S_{i-2} = K\sin(x_{i-1})$ and using equation (4.42) then the first part if the correction term is,

$$\frac{K^2}{2T}\int_0^{2\pi}\frac{dx_0}{2\pi}\int_0^{2\pi}\frac{dx_1}{2\pi}\cdots\int_0^{2\pi}\frac{dx_T}{2\pi}\left\{\sum_{j=0}^{T-1}\sin(x_j)\right\}^2 e^{i(x_i-2x_{i-1}+x_{i-2})}\sum_{n=-\infty}^{\infty}J_n(K)e^{-inx_{i-1}} \tag{4.44}$$

The integral above only returns a non-zero result for terms involving $2\sin(x_i)\sin(x_{i-2})$ and when the value of n in the summation of Bessel functions is set to -2, giving,

$$\frac{K^2}{2T}J_2(K)\int_0^{2\pi}\frac{dx_i}{2\pi}\int_0^{2\pi}\frac{dx_{i-2}}{2\pi}2\sin(x_i)\sin(x_{i-2})e^{i(x_i+x_{i-2})} \tag{4.45}$$

which simplifies to,

$$-\frac{K^2}{4T}J_2(K). \tag{4.46}$$

There is an equal result for values of $m_i = -1$, $m_{i-1} = 1$. There are in fact $(T-1)$ terms of this type for each value of i,

$$\sum_i C_i(2) = \frac{K^2}{2T}J_2(K)(-1)(T-1) \simeq \frac{-K^2}{2}J_2(K) \tag{4.47}$$

for large T. The diffusion constant is now,

$$D(K) = \frac{K^2}{4} - \frac{K^2}{2}J_2(K). \tag{4.48}$$

Higher order correction terms are derived in the paper of Rechester *et al* [75]. For the standard map the diffusion rate is independent of the sign of the starting momentum and as such is the same whether averaged over all negative momentum or positive momentum i.e. $D(p)^- = D(p)^+$.

Now, considering the case of the ratchet system, the map can be defined,

$$S_l = \sum_{j=0}^{l} KV'[x_j], \tag{4.49}$$

as before, and by following the same line of argument used in the derivation of the standard map diffusion constant, the CDW-CKR diffusion constant is written,

$$D = \lim_{t\infty}\frac{1}{2T}\sum_{m_1=-\infty}^{\infty}\cdots\sum_{m_T=-\infty}^{\infty}\int_0^{2\pi}\frac{dx_0}{2\pi}\int_0^{2\pi}\frac{dx_1}{2\pi}\cdots\int_0^{2\pi}\frac{dx_T}{2\pi}$$
$$(S_{T-1})^2 e^{im_T(x_T-x_{T-1}-(t_T-t_{T-1})(P_{init}-S_{T-1}))}\cdots e^{im_1(x_1-x_0-(t_1-t_0)(P_{init}-S_0))}. \tag{4.50}$$

Once again the quasi-linear diffusion constant is regained by setting $m_j = 0$ but the differences begin to arise when the higher order corrections are considered. It is the inclusion of the $(t_{i+1} - t_i)$ in the exponential gives rise to the extra b-dependent correction for the chirped double well map. Taking as an example an $N = 3$, i.e. a three kick sequence map, there are three different 2-kick correlations to be considered for the $C(2,p)$ correction term. These three correlations are between the 1^{st} and 3^{rd}, 2^{nd} and 4^{th} and also 3^{rd} and 5^{th} kicks in the sequence. These three different contributions to the correction term are averaged to give the final $C(2,p)$ correction term. Also important to note is that for this lowest order correction two values of m_i are required for each contribution: $m_i \pm 1, \pm 2$. This is to pick out each of the terms in the double well potential. This is in contrast to the one correlation considered in the derivation for the same correction in the standard map above. The derivation of even this lowest order term is very involved and so here it will be merely quoted.

$$C_{tot}(2,p) = \frac{1}{3}\left\{ C^{1:3}_{K\sin(x)} + C^{1:3}_{Ka\sin(2x)} + C^{2:4}_{K\sin(x)} + C^{2:4}_{Ka\sin(2x)} + C^{3:5}_{K\sin(x)} + C^{3:5}_{Ka\sin(2x)} \right\} \tag{4.51}$$

where,

$$C^{1:3}_{K\sin(x)} = -\frac{1}{4}\sum_s J_{2-2s}((1-b)K)J_s((1-b)2Ka)(\cos(p_0 b)\cos(\pi s/2)+\sin(p_0 b)\sin(\pi s/2)) \tag{4.52}$$

results from the $\langle \sin x_i \sin x_{i+2} \rangle$ correlations and,

$$C^{1:3}_{Ka\sin(2x)} = \frac{1}{4}\sum_s J_{4-2s}(2(1-b)K)J_s((1-b)4Ka)(\cos(2p_0 b)\cos(\pi s/2)+\sin(2p_0 b)\sin(\pi s/2)) \tag{4.53}$$

results from the $\langle \sin 2x_i \sin 2x_{i+2} \rangle$ correlations and so forth:

$$C^{2:4}_{K\sin(x)} = -\frac{1}{4}\sum_s J_{2-2s}((1+b)K)J_s((1+b)2Ka)(\cos(2p_0 b)\cos(\pi s/2)-\sin(2p_0 b)\sin(\pi s/2)) \tag{4.54}$$

$$C^{2:4}_{Ka\sin(2x)} = \frac{1}{4}\sum_s J_{4-2s}((1-b)2K)J_s((1-b)4Ka)(\cos(4p_0 b)\cos(\pi s/2)-\sin(4p_0 b)\sin(\pi s/2)) \tag{4.55}$$

$$C^{3:5}_{K\sin(x)} = -\frac{1}{4}\sum_s J_{2-2s}(K)J_s(2Ka)(\cos(p_0b)\cos(\pi s/2) + \sin(p_0b)\sin(\pi s/2)) \quad (4.56)$$

$$C^{3:5}_{Ka\sin(2x)} = \frac{1}{4}\sum_s J_{4-2s}((2K)J_s((4Ka)(\cos(2p_0b)\cos(\pi s/2) + \sin(2p_0b)\sin(\pi s/2)). \quad (4.57)$$

As can be seen from equations (4.52-57) the diffusion constant for the correction is dependent on the sign of p_0 and the magnitude of b. This dependence takes form in both the arguments of the Bessel functions and additional $\cos(p_0b)$ and $\sin(p_0b)$ terms not existent in the standard map. It is these terms which are responsible for the splitting of the $D(p)^-$ and $D(p)^+$ curves in figure 4.10. For a complete derivation of the $C(2,p)$ refer to [56].

Numerically, the energy spread for the ratchet can be shown to vary with initial momentum, as shown in figure 4.11. The figure shows the total average energy spread for 10^6 initial trajectories. The energy spread is an oscillating periodic function in p_0, the period of which matches the p-periodicity of the phase space. In the lower plot of figure 4.11, the momentum independent terms are removed and by a Fourier analysis a good fit is found to a polynomial in $\sin(pb)$. This is because the $\sin(p_0b)$ dependent terms are the largest contributors to the diffusion constant correction at time scales of 100 kicks (those shown in figure 4.11).

The time scales for each contribution to the diffusion constant correction can be analytically derived [56], and are given here,

$$t_r^{(\sin p_0b)} = \frac{2\ln(20)}{(Kb)^2}, \quad (4.58)$$

$$t_r^{(\sin 2p_0b)} = \frac{2\ln(20)}{(2Kb)^2}, \quad (4.59)$$

$$t_r^{(\sin 4p_0b)} = \frac{2\ln(20)}{(4Kb)^2}. \quad (4.60)$$

Each of these time scales refers to the point at which each contribution to the diffusion constant (from $\sin(p_0b)$, $\sin(2p_0b)$, $\sin(4p_0b)$) becomes saturated or averaged away. In the following chapters the value of the total ratchet time t_r will be shown to be vital to optimising the ratchet current.

4.6 Conclusion

In this chapter the CDW-CKR is introduced in detail. The broken system symmetries are shown for both the space and time domains. The classical Hamiltonian is given in dimensionless units. Phase space features were discussed for variations in each system parameter and the mechanism for this new type of ratchet was explained in terms of momentum dependent diffusion. The CDW-CKR is also given up to the first 2-kick correction term. In the chapter 5 the classical system's parameter space is explored in order to find the best system parameters for producing the strongest ratchet current.

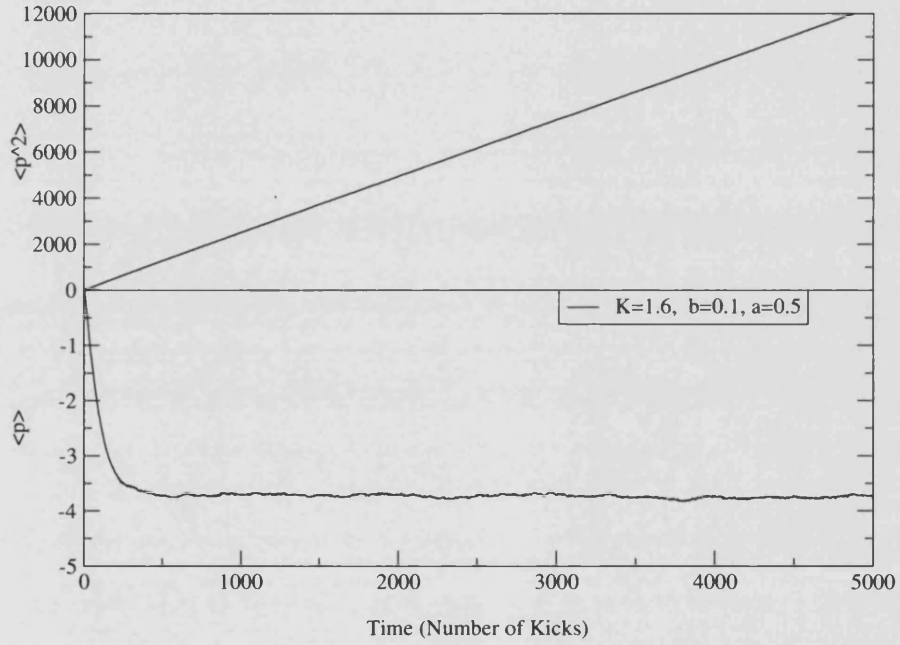

Figure 4.9: Plots of both Energy (top panel) and average ensemble momentum(lower panel) for 300,000 trajectories started along the line $p = 0$. The lower graph shows a strong negative particle current which is still constant after 5,000 iterations of the mapping.

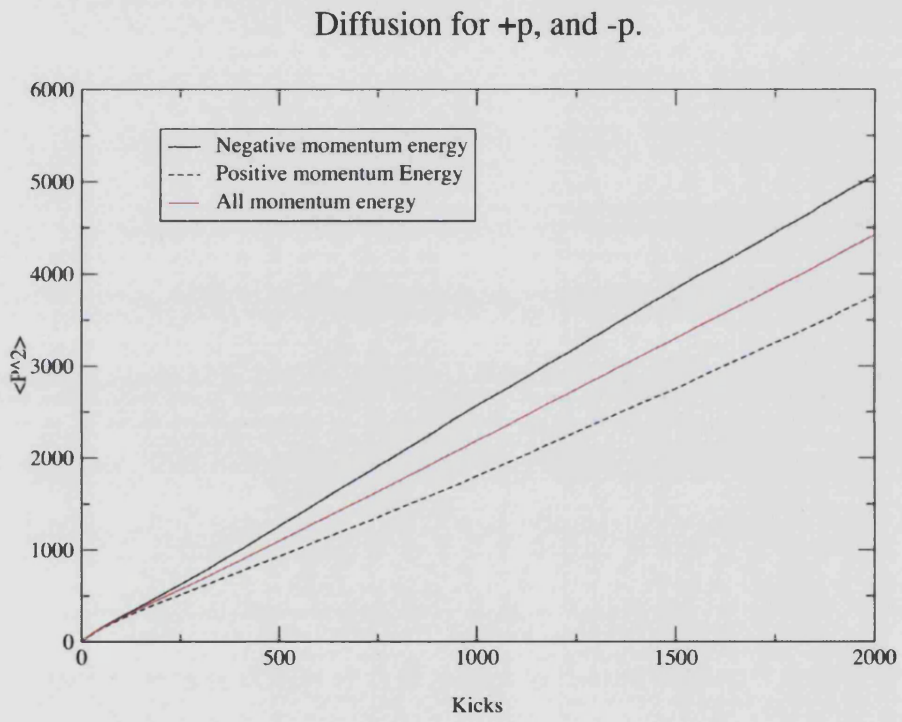

Figure 4.10: Shows the comparison between the rates at which positive and negative momentum gain energy. The red (middle) line is the total energy for the trajectories divided by two. This calculation was performed using the same starting conditions as in figure 4.9

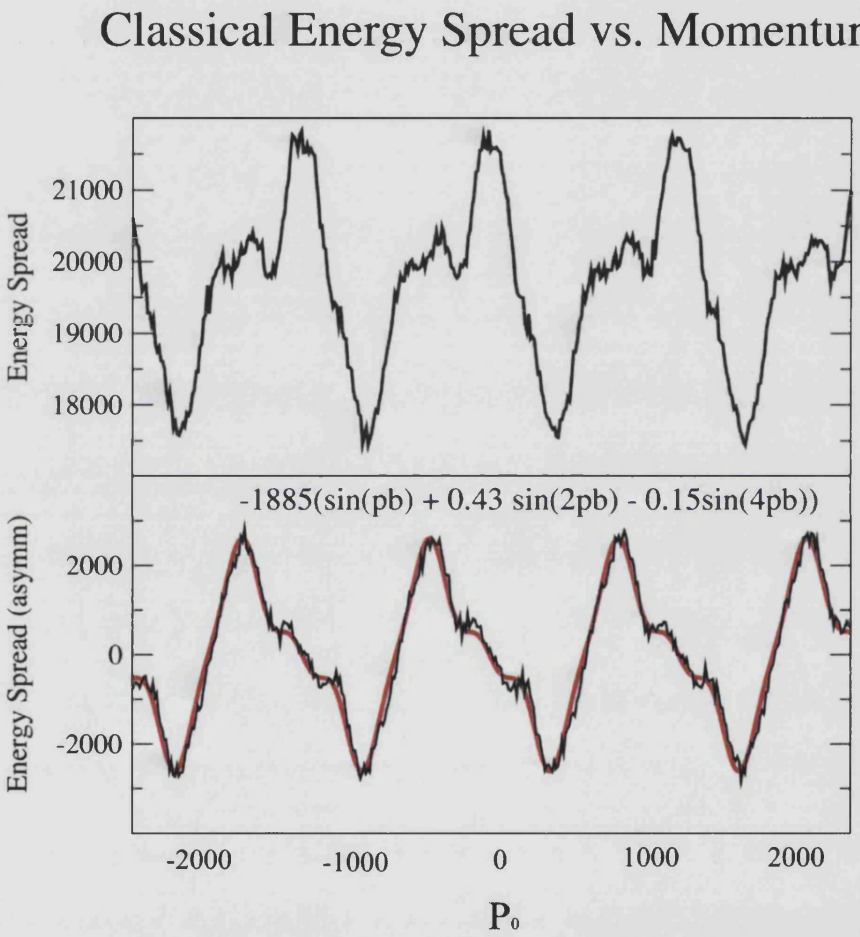

Figure 4.11: Shows momentum dependent energy spreading for the ratchet classically. $K = 14$, $a = 1/2$, $b = 0.005$. The lower panel shows the spreading after all momentum independent contributions have been removed

Chapter 5

Classical Calculations

5.1 Introduction

Now that the model for the CDW-CKR has been described classically and in detail, the system's behaviour can been examined over the large parameter space. In this chapter the system is the subject of a numerical investigation of its properties under changing system parameters. How these calculations are performed including a description of the initial starting conditions is given in detail. Each system parameter is investigated individually and those parameters which control current inversions are highlighted. Also, a combination of parameter values and ranges is proposed to give, classically, the best ratchet, i.e. the combination which produces the largest net current. While this chapter focuses on the classical dynamics of the system, with a view to a comparison of the quantum and classical regimes, the classical starting condition are chosen to reflect those of their quantum counter-parts.

5.2 Classical Simulation of a Gaussian Wavepacket

For the numerical calculation of the classical observables, momentum and energy, a classical *wavepacket* is used. This *wavepacket* takes the form of a large number of particles ($\sim 10^6$) with a Gaussian distribution in both momentum and position of a uniform deviate. A uniform deviate is a random number within a specified range and

in this case the range is specified to be between 0 and 1. One or more uniform deviates can be used, through an appropriate operation, to form other types of deviate such as the Gaussian deviate used in this chapter.

In order to get useful statistical results it is important to ensure that the random number generator used performs well. Here, a simple multiplicative algorithm [108] of the form,

$$I_{j+1} = aI_j \mathbf{mod}(m), \tag{5.1}$$

is used.

This type of algorithm has been shown to fill a multi-dimensional space sufficiently evenly so long as the multiplication factor a and the modulus m are carefully chosen. Following [108] these values are chosen as $a = 16807$ and $m = 2147483647$.

Once the random numbers have can be successfully generated the resulting uniform deviates are, by means of a transformation method, converted to a Gaussian distribution. The transformation method chosen here is known as the Box-Muller transformation [108]. The details of this method used to generate the random deviate with a Gaussian distribution are now described.

The generated uniform deviates have a uniform distribution in the specified range such that the probability of generating a number in that range between x_1 and x_1+dx_1 is given by,

$$p(x_1)dx_1 = dx_1 \tag{5.2}$$

and for a joint probability for n deviates,

$$p(x_1, x_2..., x_n)dx_1, dx_2..., dx_n = dx_1, dx_2..., dx_n. \tag{5.3}$$

Now, the joint probability distribution of y_n functions of the n uniform deviates can be written using the transformation law of probability as,

$$p(y_1, y_2..., y_n)dy_1dy_2..., dy_n = p(x_1, x_2..., x_n)\left|\frac{\partial(x_1, x_2..., x_n)}{\partial(y_1, y_2..., y_n)}\right|dy_1dy_2..., dy_n \tag{5.4}$$

For a phase space dimensionality of two as in the system of the CDW-CKR a gaussian distribution takes the form,

$$p(y_1, y_2)dy_1dy_2 = \frac{1}{N}e^{(-\frac{1}{2\sigma}(y_1^2+y_2^2))}dy_1dy_2 \tag{5.5}$$

Here, σ, is the width of the distribution. y_1 and y_2 are functions of x_1 and x_2, the uniform deviates. In order to transform uniform deviates in the range of $(0,1)$ the following Box-Muller transformations are used for each deviate.

$$y_1 = \sqrt{-2\sigma \ln(x_1)} \cos(2\pi x_2) \tag{5.6}$$

$$y_2 = \sqrt{-2\sigma \ln(x_1)} \sin(2\pi x_2) \tag{5.7}$$

These transformations can be proven to form the desired distribution by calculating the Jacobian determinant from equation 5.4,

$$\frac{\partial(x_1, x_2)}{\partial(y_1, y_2)} = -\left\{\frac{1}{\sqrt{2\pi}} e^{-y_2^2/2\sigma}\right\}\left\{\frac{1}{\sqrt{2\pi}} e^{-y_1^2/2\sigma}\right\} \tag{5.8}$$

The efficiency of the algorithm can be improved by choosing initial deviates that are formed from the ordinate and abscissa if a random point inside a unit circle. The angle that this point defines from the ordinate axis replaces the angle $2\pi x_2$ and the distance from the origin to the point squared replaces x_1. In effect, a transformation to polar co-ordinates, allowing the trigonometric calls to be replaced by $r_1/\sqrt{R^2}$ and $r_2/\sqrt{R^2}$. Where (r_1, r_2) is the co-ordinate of the point within the unit circle and with $R^2 = r_1^2 + r_2^2$. Now, the transformations are written,

$$y_1 = \sqrt{-2\sigma \ln(R^2)} \frac{r_1}{\sqrt{R^2}} \tag{5.9}$$

$$y_2 = \sqrt{-2\sigma \ln(R^2)} \frac{r_2}{\sqrt{R^2}} \tag{5.10}$$

Initial distributions formed using this transformation method are displayed for various values of σ both spatially and across momentum in figs 5.1 and 5.2.

This distribution of initial trajectories is used in Monte-Carlo type calculations discussed throughout the rest of this chapter. To insure a good statistical average the number of trajectories typically used is in the order of 10^6. This initial distribution is used as a classical analogy to the quantum mechanical minimum uncertainty wavepacket defined in chapter 6.

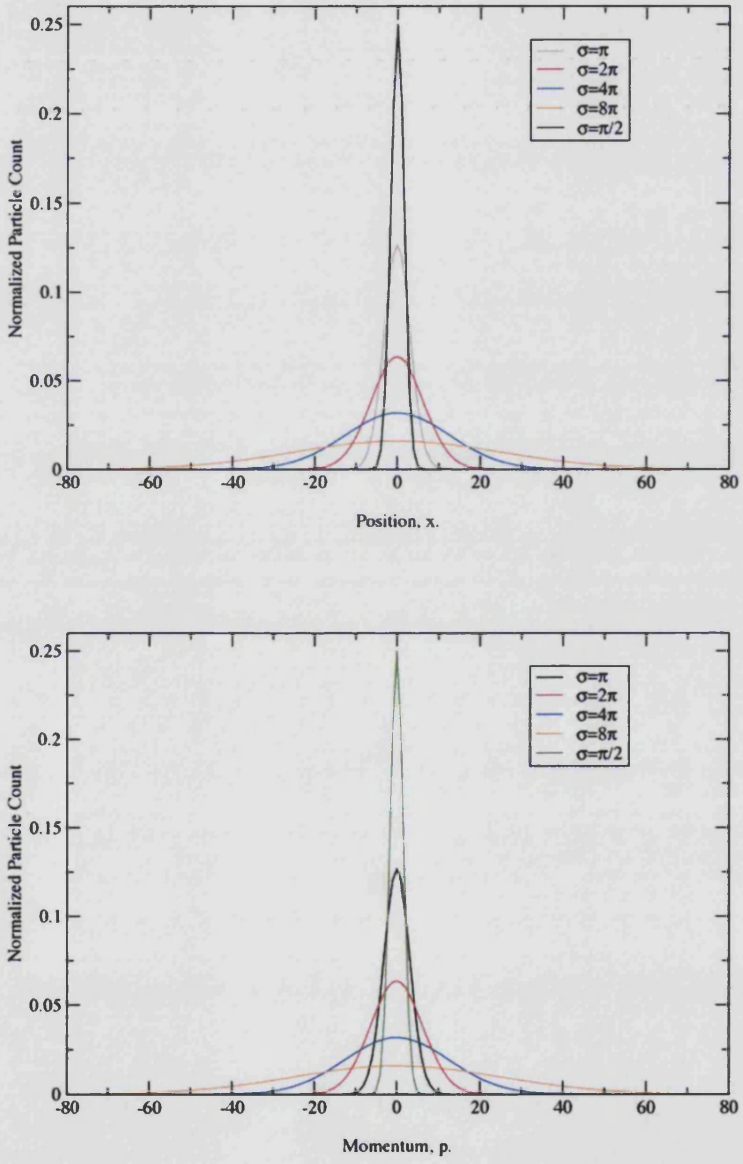

Figure 5.1: shows initial distribution of classical particles in position (top panel) and momentum (bottom panel) for various values of σ. The figure shows that the number of initial trajectories used provides a smooth distribution, the shape of which very closely approximates a Gaussian in both position and momentum.

5.3 Calculations

The classical evolution of the system is easy to perform; for each trajectory after each kick two quantities are calculated. These are the ensemble average energy,

$$E_n = \frac{1}{2M} \sum_{m=1}^{M} p_{n,m}^2 \tag{5.11}$$

which is a normalized sum over all m trajectories after each kick n, and secondly the average classical momentum,

$$\langle p_{cl} \rangle = \frac{1}{M} \sum_{m=1}^{M} p_{n,m}. \tag{5.12}$$

The results of these calculations are displayed in various forms over this and the following chapters.

5.4 The Ratchet Time

As demonstrated in the previous chapter the ratchet effect in the CDW-CKR results from trajectories with negative momentum gaining, on average, more energy than the positive momentum trajectories or vice versa. This effect is also shown to be a short time scale effect in figure 4.9 in the previous chapter. After only ~ 500 kicks the average momentum saturates and thereafter remains at a constant value. This saturation point will be known as the *ratchet time*, t_r. As explained in the previous chapter this saturation point is affected by the magnitude of the small time perturbation b. Figure 5.2 shows the energy splitting for p^- and p^+ for two different values of b. It can be clearly seen that in the instance of the smaller value of $b = 0.04$ the value of t_r is significantly larger than the corresponding saturation time for $b = 0.1$. It is the behaviour of t_r and $\langle p \rangle$ as system parameters are varied that is investigated numerically in the following sections.

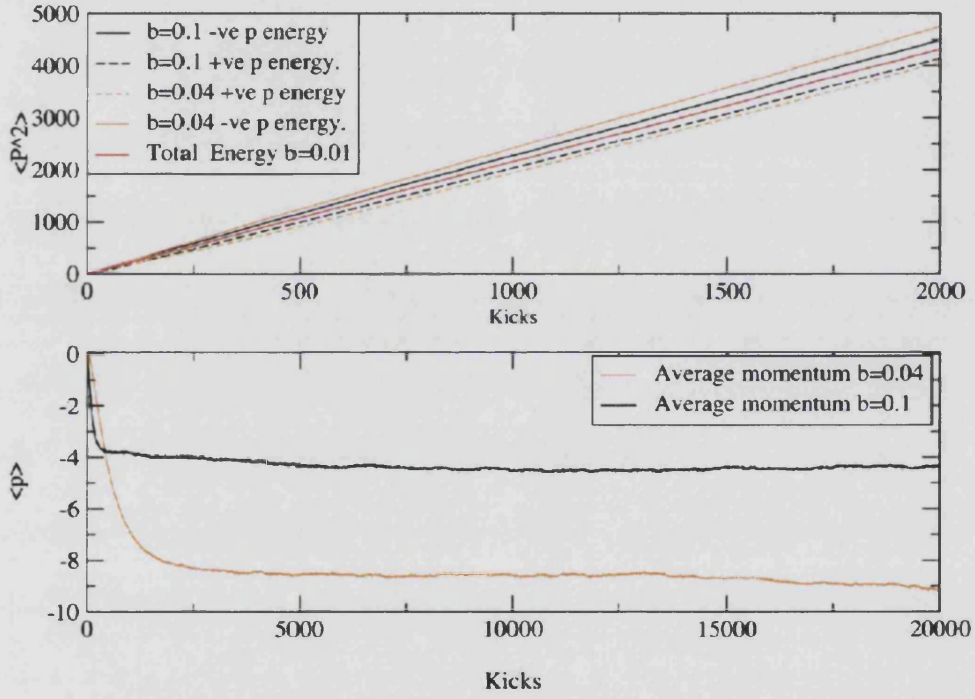

Figure 5.2: Shows the splitting of the energy for various b for the ratchet (top panel). The lower panel displays the corresponding $\langle p \rangle$ for each b. The system parameters used in the figure are $K = 1.8$, $a = 0.5$, $\phi = 0$, $N = 3$ and $b = 0.1$ and 0.04 as stated above.

5.5 Asymmetry in Momentum

The asymmetric diffusion, for trajectories with differing signs in momentum, up to the ratchet time, t_r, leads to an asymmetric distribution in momentum. This asymmetry, which is clearly demonstrated in figure 5.3, continues to build up until the ratchet time is reached. The greater the asymmetry the greater the net current for the ratchet. Particularly clear in the top right panel of figure 5.3 is a distinctive bulge in the momentum distribution for negative momentum. This graph was plotted from initial system parameters of $b = 0.03$, $K = 1.6$, $a = 0.5$ and $N = 3$ with zero phase difference for the harmonics. The lower plot shows the time averaged momentum distribution shown in the plot above but this time multiplied by p. It is straight forward to see that the difference in area underneath the curves for positive and negative momentum is proportional to the net current. This is because the top panel plots are calculated by simply summing the number of trajectories with momentum $p_1 < p < p_1 + \delta p$ in a histogram fashion after kick n. The resulting distribution is then normalized to unity.

5.6 Kick Separation (Variance of b)

Recall that the parameter b specifies the deviation from the period-one kicking: for $N = 3$ system kicks are at intervals $1+b$, 1, $1-b$. Here, b is varied through a range $-0.3 < b < 0.3$. Figure 5.4 displays results obtained using the Gaussian distribution of initial conditions described in section 5.2 for 10^6 starting trajectories. The top panel of the plot shows the average momentum of the ensemble, calculated simply by averaging all momenta for all trajectories after each kick in the sequence, for several values of b. Even from the top panel alone it is clear to see the large increase in the ratchet saturation time, t_r, and the resulting final average momentum. These results and more are recast in the two lower panels, firstly a plot of t_r against b where the ratchet time is calculated for values of b at intervals of 0.01. The value of t_r was taken at the point where a the standard deviation of a running average of $\langle p \rangle$ for 100 kicks falls to 5 percent. These numerical results are plotted against

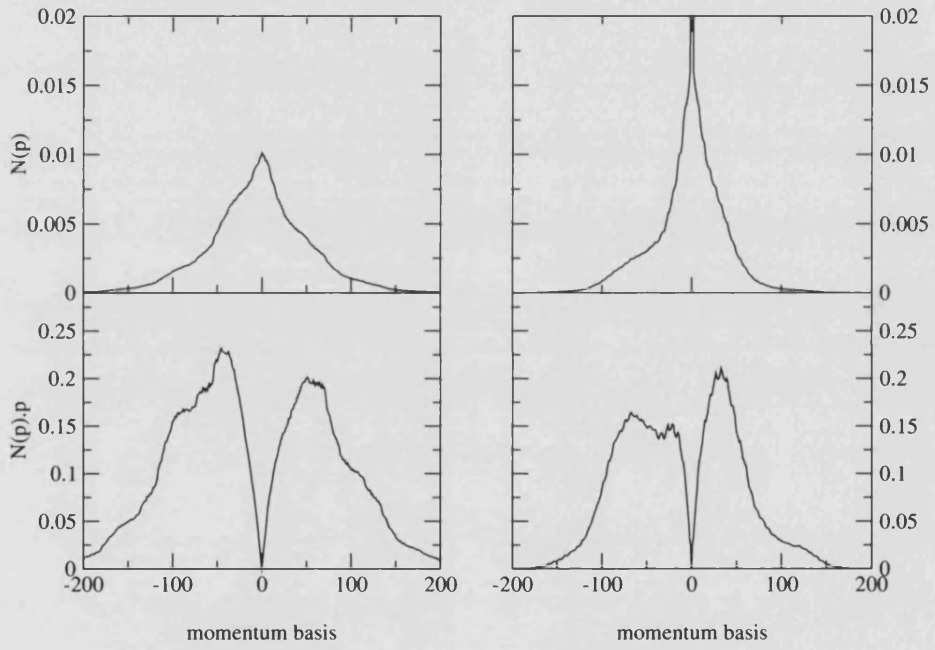

Figure 5.3: Shows the asymmetry in classical momentum distributions for values of $K = 1.6$, $N = 3$, $a = 0.5$ and $\phi = 0$ for $b = 0.1$ on the left hand side and $b = 0.03$ for the right hand side. The lower panel of plots show the same result multiplied by momentum.

an analytical formula of the form $t_r = 6.3/Db^2$. The fit is very close and presents a strong numerical argument that the ratchet time is $\propto 1/Db^2$, [56, 111]. This numerical result is in good agreement with estimations possible from the diffusion analysis of the previous chapter. For an order of magnitude estimate only it is noted that in section 4.5.1 there are odd terms (i.e. sensitive to the sign of p) of the form $I(p) = \langle \sin(p(1+b)) \cos p \rangle$. When these terms are averaged over p the terms take the form $I(p) = \langle p_\pm \rangle b/2$ from the small angle approximation for small pb. For large values of pb such terms tend towards a zero average and the correction for the ratchet is lost. Estimating the small angle approximation to be no longer valid for values of $b\sqrt{\langle p^2 \rangle} \sim \pi$ for both positive and negative momentum, one arrives at a value for the ratchet time $t_r \sim 6.3^2/Db^2$. This estimate proves consistent with the numerical findings. A more accurate estimate is possible from a more detailed consideration of the diffusion equations where each individual contribution of diffusion equation in section 4.5.1 can be assigned an individual ratchet time, [56]. The next panel shows the average current $\langle p \rangle$ against b, here once again values are plotted for intervals in b of 0.01. The most striking aspect of this final plot is the current reversal for $b < 0$. Numerically, the relationship of $|\langle p \rangle|$ with varying b is shown to closely resemble a $1/b$ proportionality. This relationship is as expected from the $1/b$ scaling of the phase space in momentum, explained in chapter 4.5.4. For a longer phase space periodicity in p, the momentum distribution can spread further before the effect of the momentum dependent diffusion becomes averaged to zero (once several periods of $D(p)$ have been encompassed by the widening distribution). This increased saturation time results in a greater current magnitude despite the local gradient (in p) of the diffusion formula becoming smaller. This can be observed from figure 5.2 where a greater *acceleration* can be seen for $b = 0.1$ compared to $b = 0.04$, however, note that the longer saturation time allows for a greater final current and hence the asymptotic response in $\langle p \rangle$ to decreasing b. As b approaches zero, the local gradient in p for the diffusion formula also approaches zero, with the ratchet effect switching off in the limit $b = 0$. The average current accurately follows a $\langle p \rangle = -1/6.3b$ trend seen again as the dashed line curve. All calculations in figure 5.4 were performed with the kick strength $K = 1.6$, $a = 1/2$, $\phi = 0$ and a sequence length of $N = 3$. The Gaussian starting distribution

had zero average in both position and momentum and were of width $\sigma = 1.5$.

5.7 Variation of a

The parameter controlling the amplitude ratio of the potential harmonics, a, is varied through a range of zero to two. The resulting classical system behaviour with respect to a is presented in figure 5.5, where both $\langle p \rangle$ and t_r are examined. The figure shows a close relationship between t_r and $\langle p \rangle$ for increasing a. Longer ratchet times correspond well with large currents. The largest current magnitude is seen for $a = 0.4$ which is plotted (green line) in the top panel of figure 5.5. The basic form of the t_r and $\langle p \rangle$ graphs can be explained by considering the shape of the potential. For a approaching zero, the potential closely approximates the a symmetric $\sin x$ shape, for which no current is produced. As a result both t_r and $\langle p \rangle$ also tend to zero. For larger values of $a > 1.5$, the first harmonic starts to become less significant and once again a symmetric potential is approximated. Again, a corresponding fall off in the magnitude of t_r and $\langle p \rangle$ can be observed.

5.8 Sequence length (Variation of N)

Another system parameter affecting the time symmetry of the system is the number of kicks in the repeated chirped sequence, N. In order to break the time reversal symmetry a minimum number of 3 kicks is needed. In this section the numerical results have the same initial starting conditions as before but with system parameters set to $K = 1.8$, $b = 0.05$, $a = 0.25$, $\phi = 0$ and values of $N = 3, 4, 5..., 11$. Increasing N has little effect on the dynamics of the CDW-CKR. Although there is a clear change in the ratchet current as N is increased, no current reversal is seen. Also the value of t_r shows only a slight downward trend for increasing N. The unspectacular system behaviour with varying N can be attributed to the fact that, for any sequence (with $N > 3$), the two kick correlations, which are the most significant contributors to the ratchet effect, are always present. There are in fact N two kick correlations for an N kick sequence. These N correlations are merely averaged and so it is no surprise

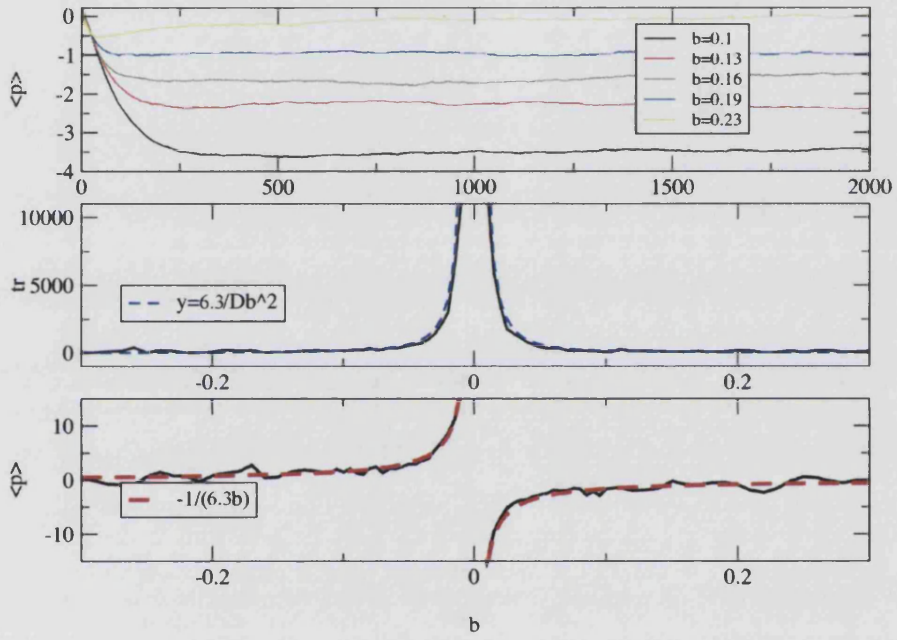

Figure 5.4: Demonstrates the variance of the net current for the CDW-CKR for various values of b. The top panel shows various evolutions of the $\langle p \rangle$ of the system for varying values of b. All other system parameters are kept constant with $N = 3$, $K = 1.6$, $a = 0.5$ and $\phi = 0$. It should be noted that as well as the saturated $\langle p \rangle$ increasing as b is reduced that the flattening point of each curve also occurs at a longer time. This time, t_r is plotted against various b in the middle panel and compared to a fitted line with equation $t_r = 6.3/(Kb)^2$. The lowest panel show a current reversal as b goes negative and a clear $1/b$ proportionality.

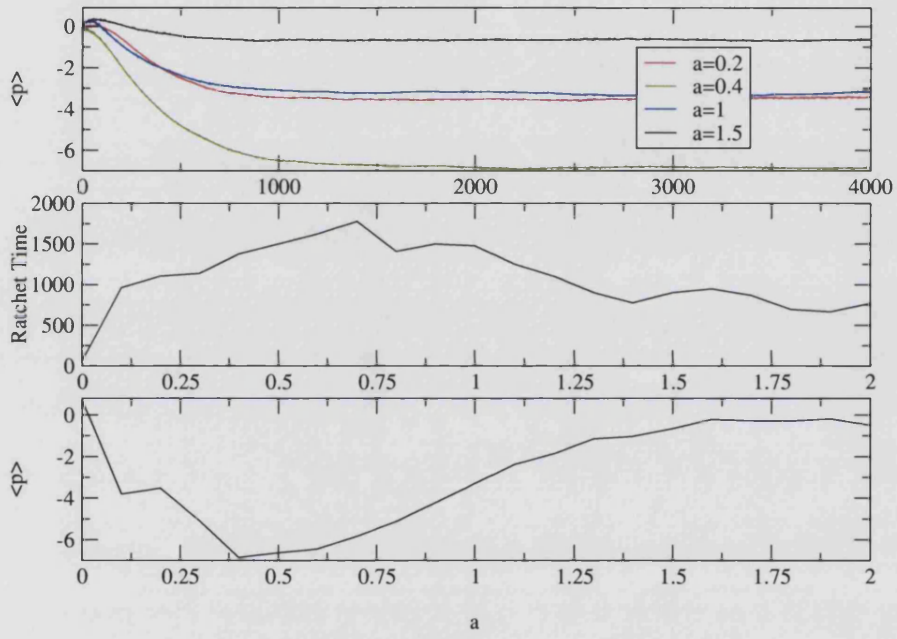

Figure 5.5: Shows classical behaviour for a varied from $0-2$. The top plots depicts $\langle p \rangle$ versus time measured in the number of kicks. The next two graphs moving down show t_r versus a and $\langle p \rangle$ versus a respectively. All graphs were calculated from 10^6 initial starting conditions with a Gaussian distribution described in section 5.2. System parameters are $K_{eff} = 1.7$, $\phi = 0$, $N = 3$ and $b = 0.05$.

that the classical behaviour is relatively unchanged for different N. It is fortunate, however, that the largest $\langle p \rangle$ is recorded for $N = 3$. Not only is this the simplest sequence to analyse in terms of it diffusion formula, but, as will be shown in chapter 8, the shortest sequence provides the most favourable quantum behaviour.

5.9 Variation of Stochasticity Parameter K

In figure 5.7, in the top graph, $\langle p \rangle$ is plotted against time. The familiar behaviour with the current increasing until the ratchet time is reached is once again clear, this time for parameter values of $N = 3$, $a = 1/2$, $\phi = 0$ and $b = 0.1$ for a range of values of K. It comes as no surprise that there is a strong dependence of the current on the kicking strength. The expression for the momentum dependent diffusion for the CDW-CKR is primarily a series of Bessel functions with arguments of various multiples of K. This dependence is apparent in the top graph of figure 5.7 where increases in K lead to a lower $\langle p \rangle$. This trend could be argued to be due to a similar reduction in the ratchet time, which as shown in section 5.4 is $\sim 1/(Kb)^2$. This trend is illustrated in the middle graph of figure 5.7 for values of $K = 1$ to 8 at intervals of $K = 0.1$. There is shown to be, numerically, a good fit to the dashed line with equation $t = 6.3/(Kb)^2$. This, however, is only part of the story. In the bottom panel of the figure $\langle p \rangle$ is plotted against K for two different values of b. The graph shows two current reversals as K is increased for the lower value of b the first of which occurs at approximately $K = 2.7$. For the higher value of $b = 0.1$ the momentum has a minimum at $K = 1.6$ which coincides with the minimum value for the $b = 0.07$ plot. After this, the magnitude of the current slowly drops to zero as K is increased, as for this higher value of b, the ratchet time becomes too small, due to the $1/K^2$ proportionality, for sufficient asymmetry in momentum space to accumulate to produce a non-zero current. However, for the lower value of b, the ratchet time remains sufficiently long at higher values of the stochasticity parameter to see current reversals. These current reversals are due to the fact that the diffusion constant correction terms are oscillating functions and can be both positively and negatively valued. For the region of a net positive current the various contributions

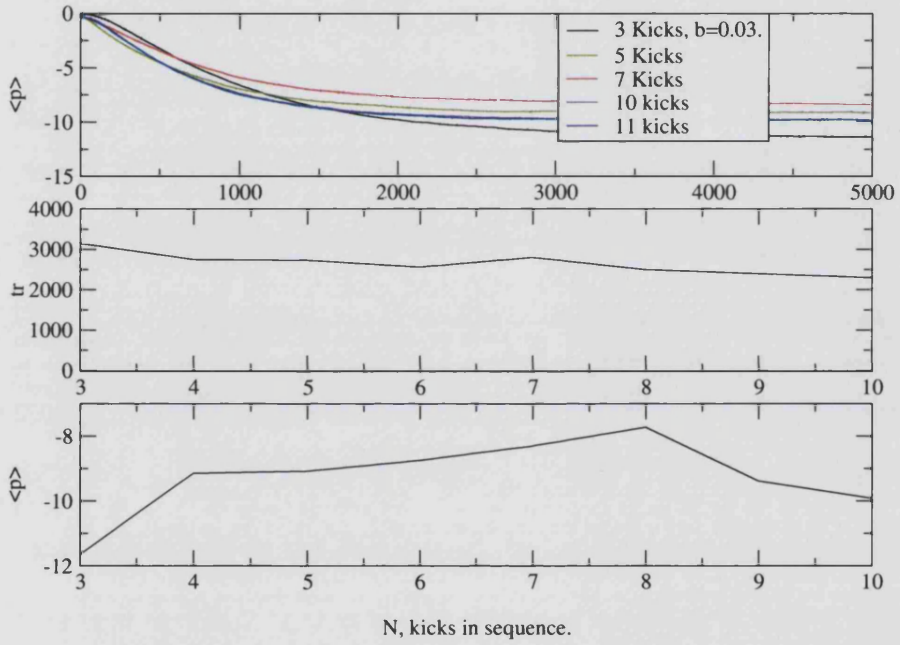

Figure 5.6: shows a comparison of $\langle p \rangle$ and t_r for the CDW-CKR with all system parameters except N held constant at $K = 1.8$, $b = 0.05$, $a = 0.5$ and $\phi = 0$. Each curve is an iteration of 10^6 initial starting conditions with gaussian distribution. The greatest $\langle p \rangle$ is demonstrated for $N = 3$. The graphs from top to bottom display: $\langle p \rangle$ vs time for various N, t_r vs N and $\langle p \rangle$ vs N.

to the diffusion constant combine in such a way that the sum of all the diffusion components return a value which is greater for the positive momentum that the negative momentum. For the long time scales in figure 5.7 the correction terms with the longest time scale which prove most important and as a result the variation of $\langle p \rangle$ with K follows the form of the $\sin p_0 b$ dependent terms in equation 4.51 at the end of the previous chapter. The trend towards zero for small K is due to the sum of Bessel functions seen in each term in 4.51 tends to zero for small K.

5.10 Relative Phase of the Harmonics

The final system parameter that gives a current reversal is the phase parameter ϕ. A range of values from $\phi = -\pi$ to $\phi = \pi$ is plotted in figure 5.8 each for the same classical *wavepacket* starting conditions and with system parameters of $b = 0.07$, $K = 1.8$, $N = 3$ and $a = 1/2$. The range of ϕ is sufficient to encompass a spatial symmetry inversion, see figure 4.2 in the previous chapter. This reversal of the spatial symmetry is sufficient to give a current reversal. The inclusion of the phase results in a term of the form $e^{i\phi}$ being introduced within the diffusion formula, reversing the overall sign in the case of $\phi = \pi$ resulting in the current reversal and given a zero real value in the case of $\phi = \pi/2$. The lower two panels in figure 5.8 highlight the points of symmetry in the potential with minima in the t_r versus $\langle p \rangle$ graph (middle) and points of $\langle p \rangle \sim 0$ in the bottom graph. Also highlighted once again is the matching of maximum t_r with maximum current (in both directions). Also, it can be seen that both the t_r and $\langle p \rangle$ are periodic in ϕ. The periodicity of the t_r curve is half that of the $\langle p \rangle$ curve. This is explained as the ratchet time is proportional to $1/Db^2$ and as a result t_r takes the periodicity of $\langle p^2 \rangle$.

5.11 Optimal Ratchet Parameters

Classically the best ratchet will be considered as the set of parameters which produce the greatest net current. As such, the only time scale of importance in maximizing the current is the ratchet time, t_r, this is a clear contrast to the quantum

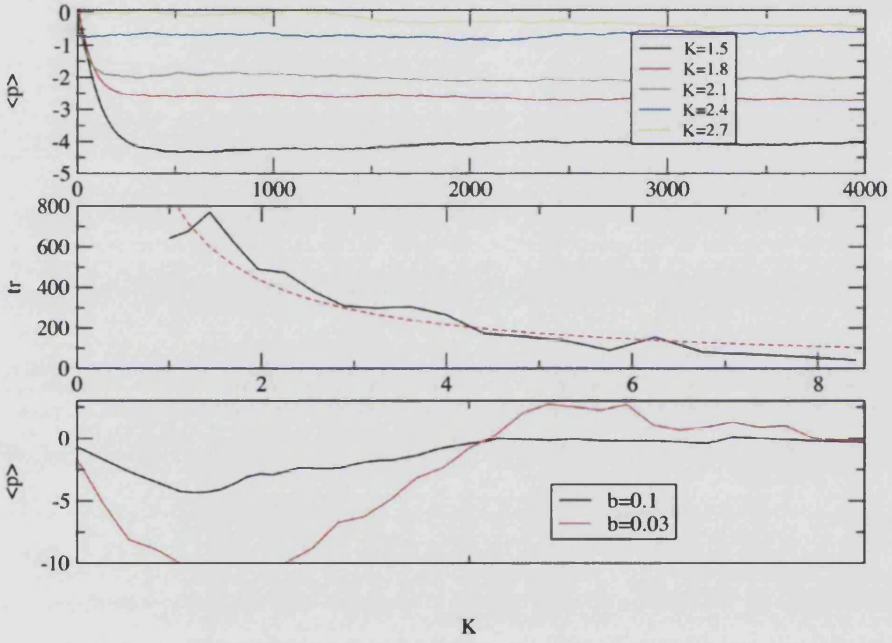

Figure 5.7: Displays the sensitivity to K of the dynamics of the CDW-CKR. Starting condition consist of 10^6 initial trajectories with a random gaussian distribution. The top graph displays the behaviour for various K, with $\langle p \rangle$ dropping as K is increased towards $K = 2.7$. Also note that the saturation point or flattening point of each curve, t_r, is smaller for the higher kick strengths. The middle graph plots t_r as a function of K and is compared to an analytical $6.3/(Kb)^2$ curve. The bottom panel displays $\langle p \rangle$ against K and displays a more complicated nature than expected with current reversals for low values of b.

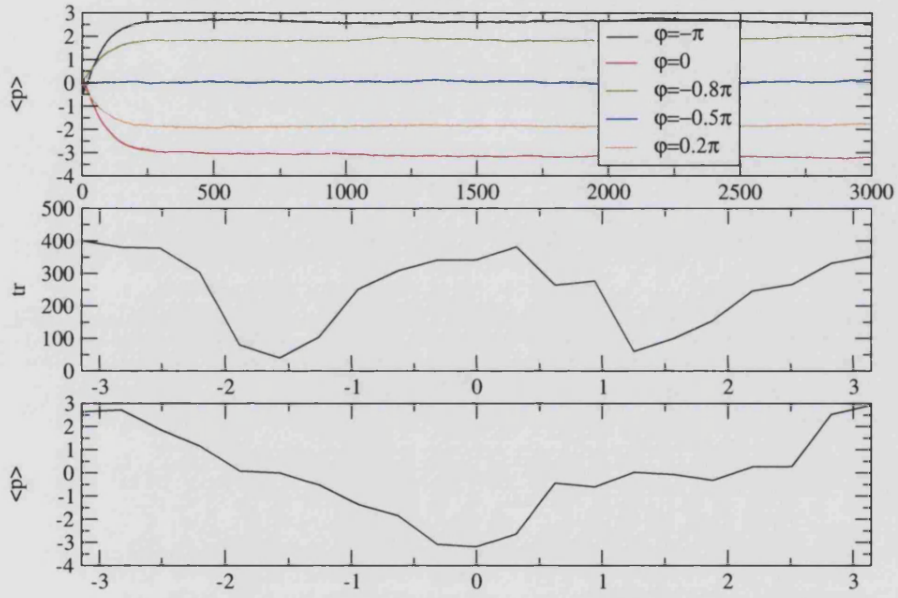

Figure 5.8: Classical calculation from 10^6 initial starting condition randomly generated with a normalized gaussian distribution. Each curve is plotted for system parameters of $K = 1.8$, $b = 0.07$, $N = 3$ and $a = 0.5$. Results are displayed for values of ϕ ranging 0 to π. Current reversal is seen as the potential goes through an asymmetric - symmetric - asymmeric transition as ϕ goes through the value of $\pm\pi/2$.

Table 5.1: displays which system parameters give current inversions and shows what parameter value gives the maximum t_r and $\langle p \rangle$

Parameter	t_r	$\langle p \rangle$	Current Reversal
N	3	3	no
a	0.7	0.4	no
b	small but non-zero	small but non-zero	yes
ϕ	$-\pi$, 0, π	0	yes
K	small but non-zero	1.6	yes

system described in the following two chapters. The system has an approximately linear growth in energy (and spread in momentum) whether a strong ratchet current is being produce or not, so choosing parameter values which maximise t_r, will optimise the ratchet. As has been shown in this chapter, a net current relies on the build up of asymmetry in momentum. This asymmetry results from the momentum dependent diffusion constant given at the end of the previous chapter. This asymmetry continues to build up to the ratchet time, t_r, so the longer the ratchet time the greater the asymmetry and the greater the net current. Follow this logic choosing correct values of K and b on which the ratchet time strongly depends is important. From figure 5.7 the best value of K would appear to be ~ 1.6, to partner this the lower the value of b leads to a longer ratchet time, so a value in the range $b = 0.015$ leads to a very strong negative current, figure 5.9. Other system parameters effect on the ratchet current are summarised in table 5.1. Where there are several values for a parameter, each producing equal $|\langle p \rangle|$, choosing the simplest system is the preferred path. So, from the table above setting $N = 3$, $\phi = 0$ and $a = 0.4$ along with $K = 1.6$ and $b = 0.015$ produces a very strong ratchet current from zero average starting conditions.

5.12 Conclusions

Through this chapter the classical behaviour for the ratchet has been studied in detail. A full parameter space has been explored. Resulting from this, optimum parameters are suggested to produce the maximum $|\langle p \rangle|$. Also numerically demonstrated are relationships for the ratchet time and ratchet current with system parame-

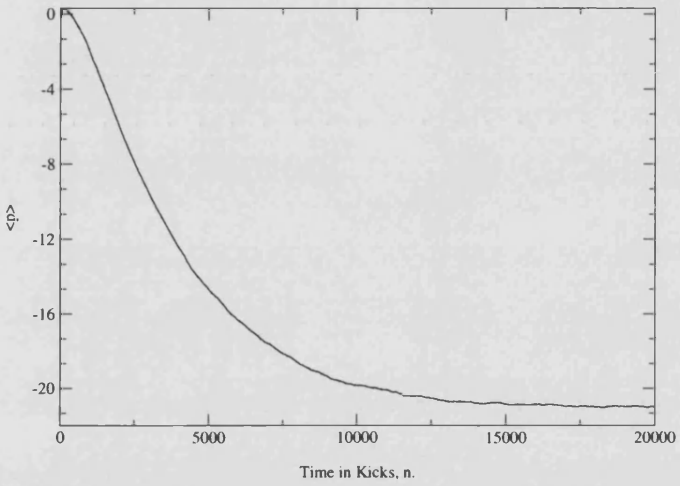

Figure 5.9: Shows the average momentum for a ratchet with $b = 0.015$. There is a very strong current at long times for small b. Here the $\langle p \rangle$ becomes saturated after $\sim 20,000$ kicks, with a maximum value of 20.69. The system parameters used are $K = 1.6$, $N = 3$, $a = 0.4$ and $\phi = 0$.

ters. The large (and rapid) spread in momentum, seen in the classical system, would suggest that an experimentally detectable ratchet current would be very difficult to achieve. The asymmetry in the classical system would quickly become very small compared to the increasing energy and momentum range resulting from the diffusive nature of the classical dynamics. In the next chapter the system is theoretically discussed in the quantum regime. For non-zero values of the Planck's constant, $\hbar$, it is found that the diffusive growth in energy for the system is eventually stopped. It is due to this well known effect of dynamical localisation, that there is proposed, a possible experimental realisation for the ratchet in a pulsed optical lattice. The quantum Hamiltonian is, therefore, introduced in terms of an atom-optics stand point in chapter 6. The system is then investigated numerically in detail in chapter 7 which finishes with suggestions for the best experimental ratchet parameters.

Chapter 6

Quantum Theory

6.1 Introduction

As for the classical system, in the quantum analysis of the system, the evolution is iterated in terms of a discrete mapping. This mapping takes the form of an evolution operator and closely parallels to the analysis of the quantum kicked rotor. The evolution operator maps the wavefunction of the system from just before a kick to that just before the next kick in the sequence. For the long time evolution of the quantum system the evolution operator is iterated repeatedly. The quantum system can be formulated so that there are only two control parameters, the effective Planck's constant, $\hbar$ and the kicking strength K. In this chapter the explicit form of the time evolution operator for the quantum ratchet is derived, the initial starting conditions, the form of the matrix elements, the expectation values for energy and momentum and the Hamiltonian. Example results are also shown as a prelude to the following chapter.

6.2 The Quantum Hamiltonian

Since a possible experimental realisation of the ratchet system is being proposed, in this thesis (in terms of an optical lattice experiment). The Hamiltonian for the chirped double well quantum kicked ratchet (CDW-QKR) will be derived from an

atom-optics standpoint. Following [67] and considering a two-level atom in a standing wave of far detuned laser light, the laser field is described, for a standing wave of laser light, formed by two counter propagating waves,

$$E(x,t) = \hat{z}E_0(\sin(k_L x))(e^{i\omega_L t} + e^{-i\omega_L t}), \tag{6.1}$$

here E_0 is the amplitude of the field and ω_L the laser frequency. Also note that the light is treated classically.

The free evolution Hamiltonian for the atom can be written,

$$H_A = \frac{p^2}{2M} + \hbar\omega_0|e\rangle\langle e|, \tag{6.2}$$

where $\hbar$ is Planck's constant, ω_0 is the atomic resonance frequency and $|e\rangle$ is the excited internal state of the atom. For the Hamiltonian describing the interaction of the atom and the field,

$$H_{AF} = -\mathbf{d}.E, \tag{6.3}$$

here d is the atomic dipole operator which can be written in terms of the atomic lowering operator $a = |g\rangle\langle e|$ as $d = (a^\dagger + a)\langle e|\mathbf{d}|g\rangle$. Now the interaction Hamiltonian can be re-written,

$$\tilde{H}_{AF} = \frac{\hbar\Omega}{2}(\tilde{a}^\dagger + \tilde{a})(\sin(k_L x)). \tag{6.4}$$

The tilde denotes the rotating frame of the laser having made the relevant transformations. $\Omega = -2\langle\tilde{e}|d_z|g\rangle E_0/\hbar$ is defined as the maximum Rabi frequency. In this frame the free atomic Hamiltonian is now,

$$\tilde{H}_A = \frac{p^2}{2M} + \hbar\Delta_L|\tilde{e}\rangle\langle\tilde{e}|, \tag{6.5}$$

which follows from using the transformation $U_L = e^{i\omega_L t|e\rangle\langle e|}$, where Δ_L is the laser de-tuning from the atomic resonance.

As the laser is far detuned, i.e. Δ_L is large, spontaneous emission can be neglected and the Schrödinger equation can be written,

$$(H_A + H_{AF})|\psi\rangle = i\hbar\frac{\partial}{\partial t}|\psi\rangle. \tag{6.6}$$

Now, decomposing the vector $|\psi\rangle$ into a linear combination of its internal and external states and noting that in the interaction representation, in which some of the time dependence is carried by the operators, not the eigenstates, the time derivatives of $|g\rangle$ and $|\tilde{e}\rangle$ are dropped and the Schrödinger equation can be written as a coupled pair of equations:

$$i\hbar\frac{\partial\psi_e}{\partial t} = \frac{p^2}{2M}\psi_e + \frac{\hbar\omega}{2}(\sin(k_L x))\psi_g - \hbar\Delta_L\psi_e, \tag{6.7}$$

$$i\hbar\frac{\partial\psi_g}{\partial t} = \frac{p^2}{2M}\psi_g + \frac{\hbar\omega}{2}(\sin(k_L x))\psi_e. \tag{6.8}$$

Equations 6.7 and 6.8 are the equations for the center of mass motion for wavefunctions $\psi_e(x,t) = \langle x|\psi_e\rangle$ and $\psi_g(x,t) = \langle x|\psi_g\rangle$ respectively. These equations can be simplified using the adiabatic approximation. Since the center of mass motion for the atom is slow compared to the internal atomic motion, which occurs on a time scale much shorter than the damping time (which corresponds to the natural atomic decay rate), it is a good approximation to assume that the internal motion is damped instantaneously. Now $\partial\psi_e/\partial t = 0$ as this is the term which carries the internal time dependence. This gives a relationship between ψ_g and ψ_e and as a result ψ_e can be eliminated from equation 6.7 which becomes,

$$i\hbar\frac{\partial\psi_g}{\partial t} = \frac{p^2}{2M}\psi_g + V_0(\sin(2k_L x)). \tag{6.9}$$

where $V_0 = \hbar\Omega^2/8\Delta_L$. Due to the large detuning almost all the atomic population is in the ground state. As a result the excited state can be ignored from the problem and the atoms have a center of mass Hamiltonian,

$$H = \frac{p^2}{2M} + V_0(\sin(2k_L x). \tag{6.10}$$

The second Harmonic in the CDW-QKR is formed by considering, an additional, 2nd pair of laser beams, with the spatial phase of the resulting interference pattern with the first pair locked, in the following geometric configuration, figure 6.1,

In the experimental set up there is a large frequency difference between each laser ($\Delta f = 160MHz$) so the standing waves produced by each laser can be added incoherently, i.e. $I_{inc} = \langle E_1\rangle^2 + \langle E_2\rangle^2$. This produces the desired $\sin(2k_L x) + \sin(4k_L x) + \phi)$ potential surface.

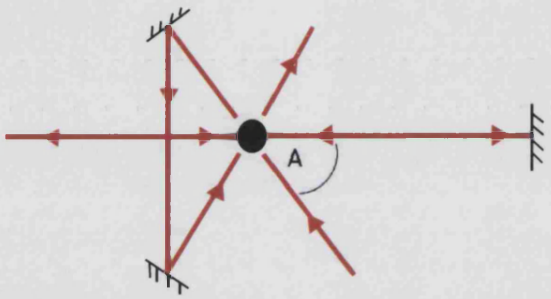

Figure 6.1: Shows the experimental set up for a kicked optical lattice. One laser is retro-reflected and one set in a 'bow-tie' configuration with a 160MHz frequency difference between the beams. The black circle in the center represents the interaction area. A=60 degrees.

This is the equation investigated below. For the CDW-CKR the chirped kicks are introduced by multiplying the term involving V_0 by $f(t)$ defined in equation 4.6 giving,

$$H = \frac{p^2}{2M} + V_0 F(2k_L x, t), \tag{6.11}$$

where $F(2k_L, t)$ give both the time dependence and the spatial form of the laser field. Following the same re-scaling transforms as in section 5.3 this Hamiltonian can be written as,

$$H' = \frac{p'^2}{2} + KV(x')f(\tau) \tag{6.12}$$

where this time $p' = -i\hbar'\partial/\partial x'$, $K = 2V_0 k_L^2 t^2/M$. The new effective Planck's constant satisfies $[x', p'] = i\hbar'$ and as such $\hbar' = 4k_L^2 t\hbar/M = 8\omega_R t$, where t is the period of the kicks and w_R atomic recoil frequency.

6.3 Momentum Basis and Bloch Functions

In the solution of the problem the spatial periodicity of the potential, $V(\hat{x})$, and hence the Hamiltonian, is used. Bloch's theorem states that because of this periodicity we can write the system wavefunction, ψ, in Bloch functions, such that ψ is expanded in plane waves,

$$\psi_q(x) = \exp(\imath q x)\phi_q(x), \tag{6.13}$$

where ϕ_q is a function periodic in x, which can be Fourier decomposed using the momentum basis,

$$|p\rangle = \frac{1}{\sqrt{2\pi}} \exp(-\imath p x), \tag{6.14}$$

such that the wavefunction can be written as the following superposition of the basis states,

$$\phi_q(x) = \sum_p A_{p,q} e^{\imath p x}. \tag{6.15}$$

Now, the wavefunction is written,

$$\psi(x) = \int_{-1/2}^{1/2} \exp(\imath q x)\phi_q(x) dq \tag{6.16}$$

Here, q represents the quasi-momentum and the range of the integral is over the first Brilliouin zone. Quasi-momenta outside of the first Brillouin zone are written $q' = q + Q$. The Bloch conditions are still satisfied as Q is defined, $\exp(2\imath Q\pi) = 1$ for $V(x) = V(x + 2\pi)$.

Since the kicking conserves quasi-momentum q, it is only the $\phi_q(x)$'s that need be evolved for each q to determine the state of the system. So, the probability amplitudes $A_{p,q}$ are evolved to find the wavefunction of the system at a later time or any dynamical variable such as the momentum or energy. The Schrodinger equation for $\phi_q(x)$, by direct substitution, takes the form,

$$-\imath\hbar\frac{\partial\phi_q}{\partial t} = \left\{\frac{(\hat{p} + \hbar q)^2}{2} + KV(\hat{x})g(t)\right\}\phi_q. \tag{6.17}$$

6.4 The Minimum Uncertainty Wavepacket

The quantum starting conditions are chosen to minimise initial uncertainty and hence gain the most information possible about the system at later times. The starting point is to consider a normalized Gaussian wavefunction in position space describing a free particle at time $t = 0$.

$$\psi(x,0) = \left\{\frac{1}{\beta^2\pi}\right\}^{1/4} e^{-\frac{x^2}{2\beta^2}} \tag{6.18}$$

where here β is the variance if the wavepacket. It should be noted that $\langle x\rangle = 0$ as the integrand,

$$\langle x\rangle = \int_{-\infty}^{\infty} dx|\psi(x,0)|^2 x \tag{6.19}$$

is an odd function in x. Also the value $\langle x^2\rangle_{t=0}$ is given by the integral,

$$\langle x^2\rangle_{t=0} = \left\{\frac{1}{\beta^2\pi}\right\}^{1/2} \int_{-\infty}^{\infty} dx e^{-\frac{2x^2}{2\beta^2}} x^2 \tag{6.20}$$

and using the integral,

$$\int_{-\infty}^{\infty} dx e^{bx^2} x^2 = \frac{\sqrt{\pi}}{2b^{3/2}} \tag{6.21}$$

can be shown to take the value $\langle x^2\rangle = \beta^2/2$. Correspondingly $\langle p^2\rangle_{t=0}$ is calculated,

$$\langle p^2\rangle_{t=0} = \int_{-\infty}^{\infty} dx\psi^*(-i\hbar\frac{\partial}{\partial x})^2\psi \tag{6.22}$$

$$\langle p^2\rangle_{t=0} = \hbar^2 \int_{-\infty}^{\infty} dx \frac{\partial\psi^*}{\partial x}\frac{\partial\psi}{\partial x} \tag{6.23}$$

$$\langle p^2\rangle_{t=0} = \frac{\hbar^2}{\beta^5\sqrt{\pi}} \int_{-\infty}^{\infty} dx e^{-\frac{2x^2}{2\beta^2}} x^2 = \frac{\hbar^2}{2\beta^2} \tag{6.24}$$

also noting $\langle p\rangle_{t=0} = 0$ since the integrand,

$$\langle p\rangle_{t=0} = \frac{\hbar}{i} \int_{-\infty}^{\infty} \psi^* \frac{\partial\psi}{\partial x} dx \tag{6.25}$$

is also odd in x. So now $\langle p^2\rangle\langle x^2\rangle = \hbar^2/4$ and the starting conditions have minimum uncertainty. For a generalized wavepacket centered at (x_0, p_0) in phase space the analytical form is,

$$\psi_{GWP}(x,0) = \frac{1}{\sqrt{\beta\sqrt{\pi}}} e^{-\frac{(x-x_0)^2}{2\beta^2}} e^{\frac{ip_0(x-x_0)}{\hbar}}, \tag{6.26}$$

where $\beta = \sqrt{\hbar}$ is chosen for a circular wavepacket in phase space i.e. $\Delta p = \Delta x$. Since the chosen basis vectors are the momentum basis the initial wavefunction can be written in terms of a linear superposition of the basis vectors. So taking account of the Bloch functions,

$$\psi_{GWP}(x) = \sum_p \int_{-1/2}^{1/2} dq A_{p,q} e^{i(p+q)x}, \tag{6.27}$$

where we have directly substituted for ϕ_q in equation (6.16). For the time iteration of the Schrödinger equation the initial amplitude coefficients are needed. These can be calculated through by working out the overlap integral $A_{p,q} = \langle p+q|\psi_{GWP}\rangle$. Which is written in full as,

$$A_{p,q} = \frac{1}{\sqrt{2\pi\beta\sqrt{\pi}}} \int_{-\infty}^{\infty} e^{i(p+q)x} e^{-\frac{(x-x_0)^2}{2\beta^2}} e^{\frac{ip_0(x-x_0)}{\hbar}} dx \tag{6.28}$$

The integrand is solved by making the substitution $z = x - x_0$ and completing the square in the exponential below,

$$A_{p,q} = \frac{1}{\sqrt{2\pi\beta\sqrt{\pi}}} \int_{-\infty}^{\infty} dz e^{z^2/2\beta^2} e^{i((p_0/\hbar)-q-p)z} \tag{6.29}$$

giving the expression for the amplitude coefficients,

$$A_{p,q} = \sqrt{\frac{\beta}{\sqrt{\pi}}} e^{-i(p+q)x_0} e^{-\frac{\beta^2}{2}(p+q-p_0/\hbar)^2}. \tag{6.30}$$

6.5 Time evolution of the Wavefunction

The evolution operator solves the time-independent Schrodinger equation:

$$\imath\hbar \frac{\partial\psi(t)}{\partial t} = \hat{H}\psi(t) \tag{6.31}$$

Equation (6.31) has the solution,

$$\psi(t) = \exp(-\imath\hat{H}t/\hbar)\psi(t_0) \tag{6.32}$$

Since the Schrödinger equation is a first order differential equation in time the state vector $|\psi(t)\rangle$ is determined for all t once it has been specified at any given time

t_0. As such an evolution operator $U(t, t_0)$ can be defined,

$$|\psi(t)\rangle = \hat{U}(t, t_0)|\psi(t_0)\rangle. \tag{6.33}$$

To preserve probability the evolution operator must be unitary. It should also be noted that it follows directly that the evolution operator can be applied repeatedly and that,

$$\hat{U}(t, t_0) = \hat{U}(t, t_1)\hat{U}(t_1, t_0). \tag{6.34}$$

For the particular case of the Hamiltonian being time independent the evolution operator can be written down directly as,

$$\hat{U}(t, t_0) = e^{-\frac{\imath}{\hbar}\hat{H}(t-t_0)}, \tag{6.35}$$

however, in the case of the CDW-QKR the Hamiltonian is time dependent and so by considering a sequence of infinitesimal time steps,

$$\hat{U}(t, t_0) = \hat{T}\exp(-\imath/\hbar \int_{t_0}^{t} \hat{H}dt) \tag{6.36}$$

where $\hat{T}$ is a time ordering operator which ensures that time is evolved consecutively.

6.5.1 The Evolution Operator

To derive the exact form of the evolution operator once again the Hamiltonian is split into two parts, the kick and the free evolution. As with the kicked rotor the evolution operator is written as a product of the these two halves of the evolution (2.9). $\hat{U}_{kick}$ is calculated by integrating across the kick for an infinitesimally short time δt, as a result the effect of the kinetic energy term, can be ignored.

$$\hat{U}_{kick} = \exp\left(\frac{-\imath}{\hbar}\int_{t-\delta t}^{t+\delta t} V(x)g(t)dt\right) \tag{6.37}$$

Since the time dependance, $g(t)$, is of the form $\delta(t - t')$,

$$\hat{U}_{kick} = \exp\left(\frac{-\imath V(x)}{\hbar}\right) \tag{6.38}$$

In rescaled units.

For the free evolution part, the kinetic energy is a constant between kicks. It is then straightforward to write,

$$\hat{U}_{q,free} = \exp(-\imath \int_{t_n}^{t_n+T_i} \frac{(p+\hbar q)^2}{2} dt) = \exp(-\frac{\imath \hbar T_i (l+q)^2}{2}) \tag{6.39}$$

Where the substitution $p = \hbar l$ is made to relate the quantum and classical mappings. T_i, $(i = 1, 2, 3, 4)$ is the period for the i-th kick of the cycle of N kicks.

The total evolution operator can now be immediately written for one complete kick-free evolution cycle, for the *ith* kick,

$$\hat{U}^i_{q,tot} = \exp(-\frac{\imath \hbar T_i (l+q)^2}{2}) \exp(-\frac{\imath K}{\hbar} \sin(x)) \exp(-\frac{\imath a K}{\hbar} \sin(2x + \Phi)) \tag{6.40}$$

So the evolution operator for one complete period, i.e N kicks in an N-kick cycle is written as the following product,

$$\hat{U}_q(T = \sum_i T_i) = \prod_i^N \hat{U}^i_{q,tot} \tag{6.41}$$

6.6 Matrix Method

In this chapter the method for extracting the results is explained for the quantum ratchet described is the Heisenberg matrix method. In this method the probability expansion amplitudes, $A^n_{l,q}$, are evolved by the evolution operator and used to calculate the observables momentum and energy. Firstly, the plane wavefunction, ϕ_q, is evolved over one kick,

$$\phi_q^{N+1}(x) = \hat{U}_q \phi_q^N(x) \tag{6.42}$$

and now for the wavefunction,

$$\psi_{n+1} = \hat{U}\psi_n(x) = \int_{-1/2}^{1/2} \exp(\imath q x) \hat{U}_q \phi_q dq \tag{6.43}$$

So the evolution for a kick cycle is carried out such that each plane wave is evolved individually by $\hat{U}_q$ and then integrated over the range of the quasi-momentum to form

the complete wavefunction for the system. This is done in accordance with Bloch's theorem. In practice the integral in equations (6.43) is replaced by a sum over a finite number of quasi-momenta.

6.6.1 Heisenberg Matrix Elements

The evolution operator defined in the previous sections is used to evolve the plane wavefunctions by means of a matrix, $\hat{U}_{l',l}$, the form of which is derived below. From equation (6.16) and again having made the substitution $p = l\hbar$,

$$A^{i+1}_{l',q} = \langle l'|\phi^i_q\rangle = \sum_l A^i_{l,q}\langle l'|\hat{U}_q|l\rangle \tag{6.44}$$

where the matrix element $\langle l'|\hat{U}_q|l\rangle$ is evaluated from,

$$\langle l'|\hat{U}_q|l\rangle = \frac{1}{2\pi}\int_0^{2\pi} \exp(-\imath l'x)\hat{U}_q \exp(\imath lx)dx \tag{6.45}$$

By direct substitution from equation (6.40) the matrix elements are written,

$$\begin{aligned}\langle l'|\hat{U}_q|l\rangle \;=\; & \frac{1}{2\pi}\int_0^{2\pi} dx \exp(-\imath l'x)\exp(-\frac{i\hbar T_i(l+q)^2}{2}) \\ & \exp(i\frac{K}{\hbar}\sin(x))\exp(i\frac{aK}{\hbar}\sin(2x+\phi))\exp(\imath lx).\end{aligned} \tag{6.46}$$

Now as before the evolution operator can be split into the free evolution part and the kicking part, $\hat{U}_q = \hat{U}_{free}\hat{U}_{kick}$, so it can be written,

$$\langle l'|\hat{U}_q|l\rangle = \langle l'|\hat{U}_{free}|l\rangle\langle l'|\hat{U}_{kick}|l\rangle \tag{6.47}$$

evaluating $\langle l'|\hat{U}_{free}|l\rangle$,

$$\langle l'|\hat{U}_{free}|l\rangle = \frac{1}{2\pi}\int_0^{2\pi} \exp(-il'x)\exp(-\frac{i\hbar T_i(l+q)^2}{2})\exp(ilx), \tag{6.48}$$

$$\langle l'|\hat{U}_{free}|l\rangle = \frac{1}{2\pi}\exp(-\frac{i\hbar T_i(l+q)^2}{2})\int_0^{2\pi}\exp(i(l-l')x), \tag{6.49}$$

$$\langle l'|\hat{U}_{free}|l\rangle = \exp(-\frac{i\hbar T_i(l+q)^2}{2})\delta(l-l'). \tag{6.50}$$

which gives a diagonal matrix for the free evolution in momentum space. Now to evaluate $\langle l'|\hat{U}_{kick}|l\rangle$ the Bessel function generating function is used,

$$\exp((\frac{y}{2})(t-\frac{1}{t})) = \sum_{m=-\infty}^{\infty} J_m(y)t^m \tag{6.51}$$

where J_m is an ordinary Bessel function. If y is set to $K/\hbar$ and t to e^{inx} then the generating function takes the form,

$$\exp(i\frac{K}{\hbar}\sin(nx)) = \sum_{m=-\infty}^{\infty} J_m(\frac{K}{\hbar})\exp(imnx). \tag{6.52}$$

which is a more convenient form to perform the integration $\langle l'|\hat{U}_{kick}|l\rangle$. So now,

$$\langle l'|\hat{U}_{kick}|l\rangle = \frac{1}{2\pi}\sum_{r,s=-\infty}^{\infty} J_r(\frac{K}{\hbar})J_s(\frac{aK}{\hbar})\exp(is\phi)\int_0^{2\pi}\exp(i(l-l')x)\exp(i(2s-r)x)dx \tag{6.53}$$

the integrand in (6.53) is zero unless $l-l'-r+2s=0$ so setting $r=l-l'+2s$ gives,

$$\langle l'|\hat{U}_{kick}|l\rangle = \sum_{s=-\infty}^{\infty} J_{l-l'+2s}(\frac{K}{\hbar})J_s(\frac{aK}{\hbar})\exp(is\phi). \tag{6.54}$$

All Bessel function orders are integer valued. So bringing everything together,

$$\langle l'|\hat{U}_q^i|l\rangle = \exp(\frac{-\imath\hbar T_i(l+q)^2}{2})\sum_s \exp(\imath s\Phi)J_{l-l'-2s}(\frac{K}{\hbar})J_s(\frac{aK}{\hbar}), \tag{6.55}$$

It should be noted that the form of $\langle l'|\hat{U}_{kick}|l\rangle$ is effectively a banded complex unitary matrix. For computational purposes, it should be noted that, the value that Bessel function returns sharply drops towards zero as its order increases. As a result, by choosing a suitable order limit i.e. limiting the maximum value of s the matrix becomes sparsely filled and can be transformed into a $2s$ x $lmax$ matrix where $lmax$ is the momentum basis size. This results in a significant reduction of computation time.

6.7 Observables

The calculation of the expectation values for the observables momentum and energy is now a simple task given the time evolved momentum amplitudes. For a

dynamical variable with an associated linear Hermitian operator,

$$A|a'\rangle = a'|a'\rangle, \tag{6.56}$$

the expectation value for the dynamical variable A is given by,

$$\langle A\rangle = \langle\psi|A|\psi\rangle \tag{6.57}$$

where ψ is the state vector for the wavefunction. Now,

$$\langle A\rangle = \sum_{a',a''}\langle\psi|a''\rangle\langle a''|A|a'\rangle\langle a'|\psi\rangle, \tag{6.58}$$

since $|\psi\rangle = \sum_{a'} C_{a'}|a'\rangle$ implies $C_{a'} = \langle a'|\psi\rangle$,

$$\langle A\rangle = \sum_{a'}|\langle\psi|a'\rangle|^2\langle a'|A|a'\rangle = \sum_{a'}|C_{a'}|^2 a' \tag{6.59}$$

so following this formalism the energy and momentum expectation values can be written as,

$$\langle E\rangle = \hbar^2\langle\psi_n|\frac{\hat{l}^2}{2}|\psi_n\rangle = \frac{\hbar^2}{2}\sum_{l,q}(l+q)^2|A^n_{l.q}|^2 \tag{6.60}$$

and,

$$\langle p\rangle = \hbar\langle l\rangle = \hbar\langle\psi_n|\hat{l}|\psi_n\rangle = \hbar\sum_{l,q}(l+q)|A^n_{l.q}|^2 \tag{6.61}$$

where the $|A^n_{l.q}|$ is the momentum and quasi-momentum dependent amplitude coefficient. The superscript n refers to the kick number.

As an illustration before the main results are presented in chapter 7, figure 6.2 shows 3 plots for the CDW-QKR. For all three plots the starting conditions used are the minimum uncertainty wavepacket described in section 6.4 with a value of $\hbar = 0.25$. In the top panel the value $\langle p^2\rangle$ is plotted against time. The tell-tale sign of dynamical localisation takes the form of the saturation of the growth in energy with time as the suppression in momentum space occurs at the break time t^*. The middle plot demonstrates the average current for the quantum ratchet. This graph too saturates after some time, this time due to the ratchet time t_r introduced in previous chapters, as in this case $t_r < t^*$. The bottom panel show the average displacement resulting from the ratchet effect.

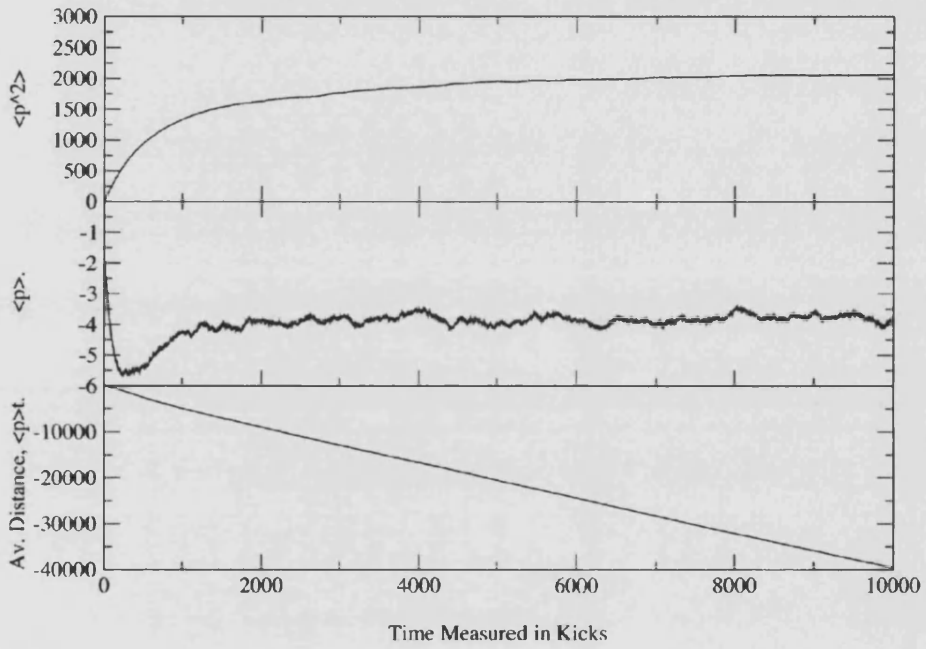

Figure 6.2: Displays in the top panel the quantum energy for the quantum ratchet. Note the saturation in energy which is indicative of dynamical localisation. The break time for the ratchet system is significantly larger than the corresponding time symmetry system. The middle panel shows the $\langle p \rangle$ for the ratchet and show that the non-zero current is not just a classical phenomenon. The current saturated after the ratchet time t_r. The bottom panel shows the calculated average displacement due to the ratchet effect and is calculated by $\langle p \rangle t$. All plots had initial system parameters of $\hbar = 0.25$, $a = 0.5$, $K = 1.6$, $b = 0.1$ and $N = 3$ and were started with a minimum uncertainty wavepacket.

6.8 Momentum Distribution

As the effect of dynamical localisation is understood in terms of a destructive interference that limits the spread of the wavefunction in momentum space it is very instructive to plot the time averaged amplitude coefficients. Also as from the diffusion analysis in chapter 4 there is expected to be an asymmetric distribution in momentum it serves as a doubly important study. For the CDW-QKR the time averaged absolute square of the momentum amplitudes after time $t = n$ kicks are calculated,

$$P_l = \frac{1}{NQ} \sum_{n=1}^{N} \sum_{-q}^{q} |A_{l,q}^{n}|^2 \tag{6.62}$$

where q is the quasi momentum, n the kick number and l the angular momentum basis. Figure 6.3 shows the momentum distribution for $\hbar = 0.25, K = 1.6, a = 0.5$ and $N = 3$. The bottom panel has the same result plotted against a log scale and show the characteristic straight sided shape associated with a localised wavefunction. The shape of the plot in the lower panel is well approximated by the equation,

$$P_p = \exp(-\frac{2\hbar|l|}{L}) \tag{6.63}$$

where L is the localisation length which for the three kick cycle is significantly longer than for the time symmetric case.

Also note the slight asymmetry due to the broken symmetries in the system which are now frozen in by the localisation of the wavefunction for all time $t > t^*$.

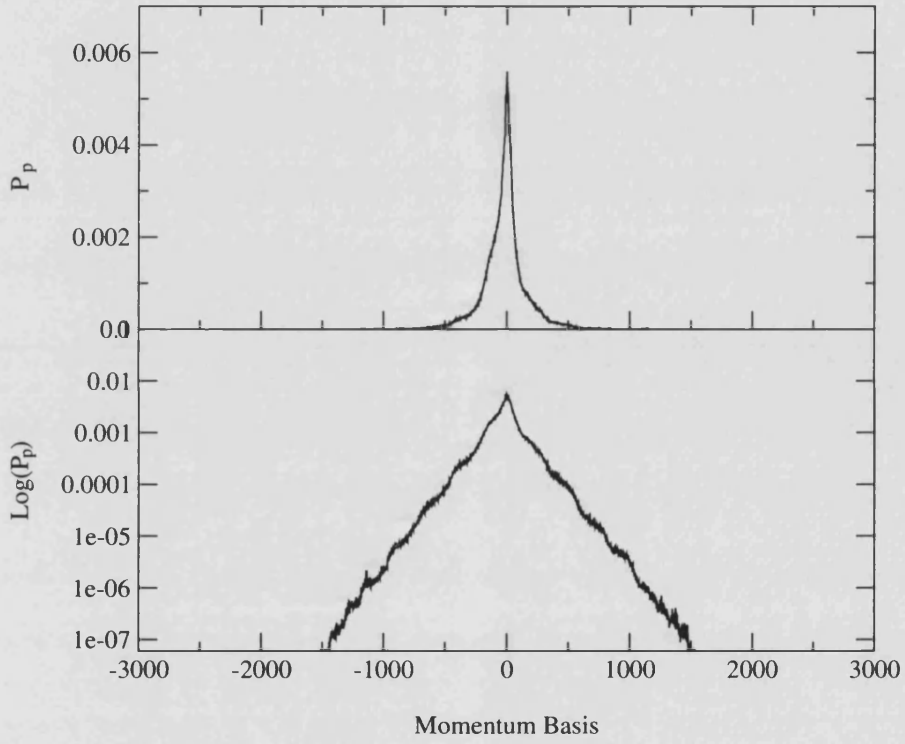

Figure 6.3: Displays the localised momentum wavepacket for the same initial starting conditions used in figure 6.2. The lower plot shows the same result but plotted on a logarithmic scale. This lower plot shows the easily recognisable straight side features of dynamical localisation.

Chapter 7

Quantum Results

7.1 Introduction

The quantum behaviour of the ratchet turns up some interesting results. The effect of dynamical localisation was shown to exist in the CDW-QKR (figs. 7.1-2). However, extra considerations arise when trying to predict the system behaviour. For instance, is the localisation length for the CDW-QKR of similar magnitude to that of the standard quantum kicked rotor? How do the break time t^* and the localisation length, L, depend on system parameters such as K or the number of kicks in a cycle, N? These questions are investigated in this chapter. As will be demonstrated through the following sections a good understanding of the behaviour of the localisation length is essential when considering the ratchet current. I examine in detail the effect of each system parameter on the localisation length for the ratchet. A study of the quantum current is presented. At every point a comparison between the quantum and classical results is given.

7.2 Dynamical localisation in the CDW-QKR

Now it has been shown that the CDW-QKR does indeed localise (despite broken time reversal symmetry) the extent and speed with which the system reaches a localised state needs to be investigated. The localisation of the system should be

compared qualitatively with that of the paradigm delta kicked rotor. As explained in chapter 2, the quantum dynamics of the δ-kicked rotor depend on only two parameters. The quantum kicked rotor's localisation behaviour with respect to K, the stochasticity parameter, and $\hbar$ is well known so this provides a good starting point for an analysis of the more complex nature of the CDW-QKR. As a follow-on from figs 6.1-2 at the end of the last chapter, figure 7.1 shows the localised momentum wavefunctions for the CDW-QKR as three of the system parameters are changed. Figure 7.1(a) shows a not unexpected increase in the localisation length as the effective Planck's constant is reduced. The corresponding increase in the quantum break time is shown in figure 7.2 (top panel). This shows the system follows the classical dynamics for longer times as $\hbar$ is reduced, as is expected by the correspondence principle. In the middle panel the parameter K is varied and as for the standard quantum kicked rotor the localisation length increases. In the third panel, the momentum distributions are shown for the system as the time symmetry is turned on ($b = 0.1$) and off ($b = 0$). A marked increase in the localisation length for the time asymmetric system, as well an asymmetry in the momentum distribution, is apparent. The fine detail (of order 1 in momentum) observable in the shape of both the quantum momentum distributions, in figure 7.1, is attributed to *scarring* by remnants of the most irrational cantori and tiny phase space islands still seen at moderate K. In fact, momentum values associated with winding numbers which are 2π multiples of the golden mean torus were found to leave the most pronounced scars in the momentum distribution. These scars are caused by regions of phase space where these highly irrational tori existed where there is a lower flux through very broken-down phase space barriers. These broken-up barriers cause a $traffic\ jam$ in the expansion of the momentum distribution, resulting in a noticeable change in number density either side of one these barriers.

Also of interest is the ratchet current for the CDW-QKR. As with the classical dynamics, the current produced by the system varies considerably with changing system parameters. However, the additional $\hbar$ dependence shows up some marked differences between quantum and classical behaviour for some parameter values. Figure 7.2 displays some quantum ratchet average momentum plots for various $\hbar$ (middle panel)

and K (bottom panel). In the middle panel it is clear to see that the ratchet current is highly dependent on the effective Planck's constant. This can be explained by a considering how the localisation interrupts the diffusive growth of the system and will be expanded on later in the chapter. From the plot there is a clear inverse relationship between the magnitude of the current and the value of $\hbar$ i.e. decreasing $\hbar$ leads to an increased current. In the bottom panel the correspondence with changing K and the ratchet current appears to back up the classical dynamics as the current once again falls away with increased K.

7.3 The Shepelyanski Relationship

Dynamical localisation for the CDW-QKR occurs for the same reasons as argued for the kicked rotor in section 2.4. Briefly, during the free evolution phase (represented by U_{free}) the phases of each of the wavefunction components evolve different amounts and for irrational $\hbar/2\pi$ these components quickly become pseudo-random. When U_{kick} now operates on the wavefunction and causes transitions between momentum states this randomislocaliseation cause transitions to large momenta to destructively interfere, causing the wavefunction to localise in momentum space.

A method for the estimation of the localisation length L, was argued first by Shepelyanski *et al* [63] and is now outlined. Numerical simulation and experimental results show a wavepacket that has dynamically localised (i.e. evolved to or beyond the break time t^*) is represented well by the form,

$$\psi(l,t) \sim \exp\left\{\frac{-\hbar|l-l_i|}{L}\right\}. \tag{7.1}$$

This can be represented as a superposition of Floquet states (which are the eigenfunctions of $U(\tau)$). The most excited states localised around $p = 0$ are within L, so there are $L/\hbar$ excited eigenfunctions. Each state has an associated quasi-energy phase $e^{-i\omega_i}$, where the ω_i lie within zero to 2π. This in turn results in a quasi-energy level spacing of $\delta\omega \sim 2\pi\hbar/L$. The system must now evolve for a time $t^* > 1/\delta\omega$ before the quantum effect of the discrete spectrum is felt. This time, defined as the

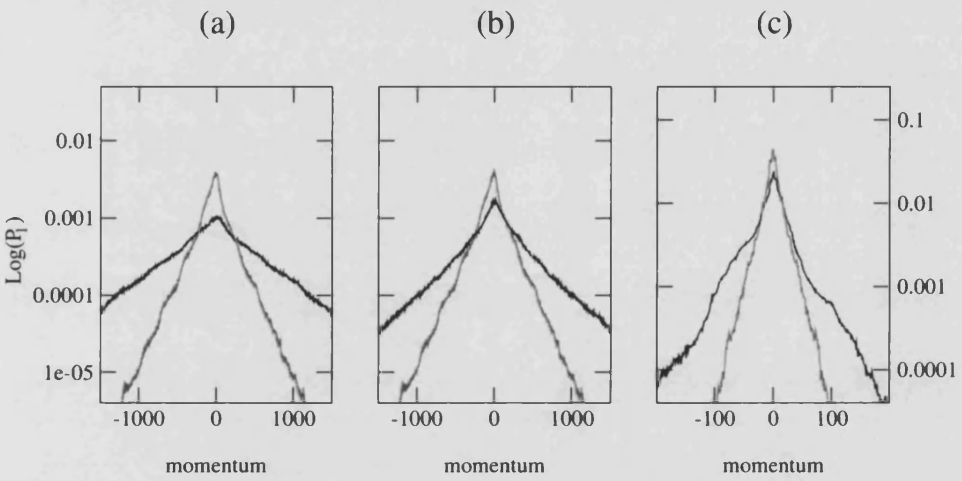

Figure 7.1: Shows the variation in localisation length with changing system parameters. Each plot shows, for the CDW-QKR, a localised momentum space wavefunction for $t > t^*$. a) In the far left hand panel the effective scaled Planck's constant is shown for $\hbar = 1/2$ (green) and $\hbar = 1/8$ (black). The significant increase in the localisation length, L, for small $\hbar$ is reflected in a longer break time, b) In the middle plot the stochasticity parameter is shown for $K_{eff} = 1.8\sqrt{2}$ (green) and $K_{eff} = 2.8\sqrt{2}$ (black) and illustrates the proportionality of L and D_{cl} , c) In the last plot, the presence/absence of the time reversal symmetry is demonstrated. $b = 0$ (green) and $b = 0.1$ (black) shows that, L, increases substantially as the time symmetry is destroyed. This is largely due to the effective tripling of the time periodicity of the system.

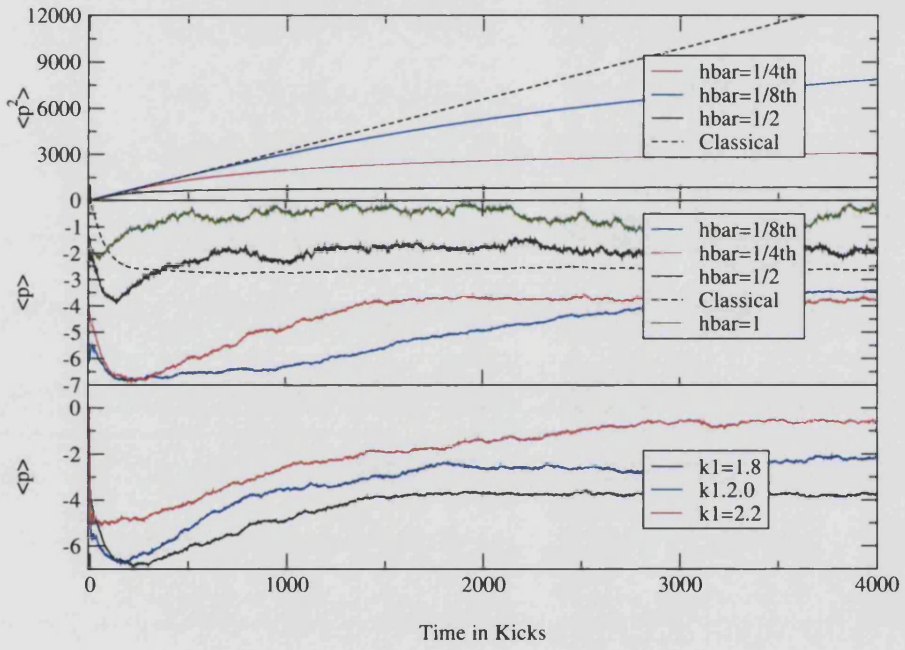

Figure 7.2: Shows graphs of energy, $\langle p^2 \rangle$ and average momentum, $\langle p \rangle$, against time, measured in the number of kicks. The top two panels compare various $\hbar$ with classical behaviour. The top panel shows that with decreasing $\hbar$, the quantum energy growth follows that of the classical for longer times. The middle panel compares quantum and classical average momentum. The values of high $\hbar$ shows significantly lower average final momentum as localisation sets in before t_r has been reached. The final plots shows that the quantum current also falls off with increasing K in the range 1.8 to 2.2. All plots were for parameter values $b = 0.1$, $a = 0.5$, $N = 3$ and $K = 1.8$ unless otherwise stated.

quantum break time, is now written,

$$t^* \sim L/\hbar. \tag{7.2}$$

Since the quantum diffusion of the system closely mirrors the classical diffusion D_{cl} well past the Ehrenfest time t_E up until t^* the approximation,

$$D_{cl}t^* \sim L^2 \tag{7.3}$$

can be made, where the quantum system evolves like the classical one until an energy $(p - p_0) \sim L^2$ is reached. From this the localisation length can be estimated,

$$L \sim \alpha D_{cl}/\hbar, \tag{7.4}$$

where α is a constant of proportionality, which was estimated to be $\alpha = 0.5$ by Shepelyanski for the standard quantum kicked rotor. The classical diffusion constant for the ratchet is somewhat more complex than that of the standard kicked rotor as explained in chapter 3. For the CDW-QKR the value D_{cl} will take arguments $D_{cl}(K, a, b, \phi)$ and a corresponding change in the quantum localisation length would be expected. Through the following sections each system parameter is varied in turn (with all others held constant) and the localisation and classical diffusion rates are plotted for each parameter. This should show the correspondence between the quantum localisation length and the classical diffusion rate and also highlight any purely quantum effects. As a result a value for the constant of proportionality α for the CDW-QKR can be determined.

7.3.1 Variation of K_{eff}

The stochasticity parameter K_{eff} has the largest effect on the rate of classical diffusion as it is the only parameter in the quasi-linear term in the diffusion constant D_{cl}. Here the value of K_{eff} is varied through a wide range for several different values of $\hbar$. In figure 7.3 the localisation length is plotted against each value for the quasi-linear diffusion constant $(D_{cl}^{ql}(K) \sim K_{eff}^2/2)$ so that the gradient of the line will give the value $\alpha/\hbar$ for the ratchet. The values for the localisation constant were obtained

by fitting the form $\exp(-2|l|\hbar/L)$ to the final momentum wavefunctions (the 2 arises as it is the modulus squared of the expansion amplitudes which is used). The initial wavepacket starting conditions were as described in section 6.5. Both negative and positive momentum *wings* of $P(p)$ where used in the fit so that in instances where there is a strong asymmetry in the momentum distribution, such as in figure 7.1c, a corresponding decrease (or increase) in the estimate of L was avoided. The resulting value of α taken from the gradients of the graphs is $\alpha \sim 6.4$. The constancy of the value for α in each graph is consistent with the quantum kicked ratchet relationship between L, D and $\hbar$ in equation 7.4. This relation between the localisation length and D_d^{ql} ignores corrections to the diffusion constant which can be significant for some values of the system parameters, notably for low K_{eff}. In this case, the effect of changing the values of b, ϕ and a can be important and are explored in sections 7.3.3-5.

7.3.2 Variation of $\hbar$

Here the effective Planck's constant, $\hbar$, is varied. The expected behaviour resulting from the Shepelyanski relationship given by equation 7.4 is an inverse relationship. The quantum system was numerically simulated for values of $\hbar$ ranging from 0.1 to 1 and the results plotted against L in figure 7.4. Parameters were chosen to be $K = 1.8$, $b = 0.1$, $a = 0.5$ and $N = 3$, and as such the expected proportionality constant is $\alpha D = 20.73$. This value is plotted in figure 7.4 (red line) and shows an excellent agreement across the range of $\hbar$ used. This result adds substantial weight to the other results in the chapter as the system is behaving as expected, backed by the great amount of numerical results seen for other kicked Hamiltonian systems such as the quantum kicked rotor. This result underlines the finding that for lower $\hbar$ the quantum system will follow the behaviour of its classical counterpart. This is demonstrated by the increasing localisation length, showing that the wavefunction spreads further in momentum before the quantum destructive interference is felt.

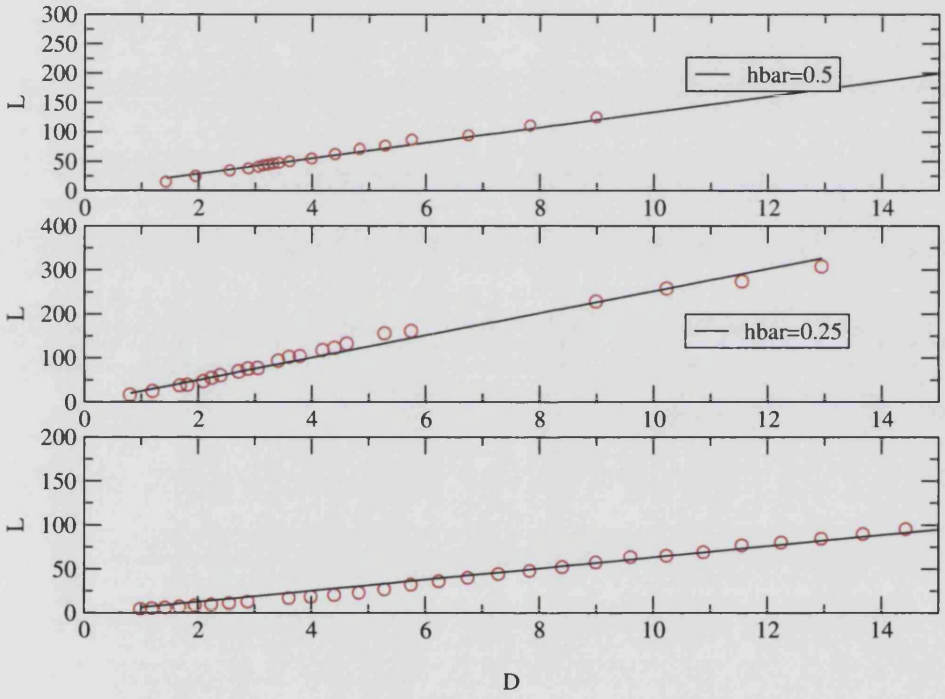

Figure 7.3: Displays the linear D vs L relationship for $\hbar = 1, 1/2, 1/4$ the gradient of the curve will be $\alpha/\hbar$ according to the Shepelyanski relationship. From measurement by a line of best fit this proportionality constant α is found to be ~ 6.4. The x-axis shows the quasi-linear diffusion and as such ignore all kick-to-kick correlations in D_{cl}.

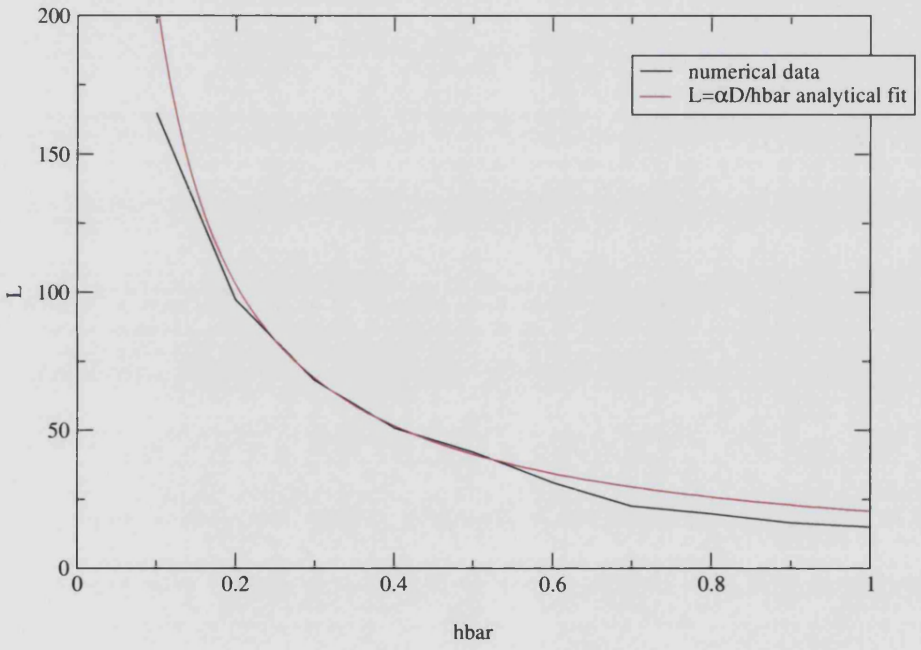

Figure 7.4: Parameters were chosen to be $K = 1.8$, $b = 0.1$, $a = 0.5$ and $N = 3$ and L plotted against $\hbar$. A good correspondence to the expected proportionality constant is shown by the red curve taking the values $L = 20.73/\hbar$.

7.3.3 Variation of a

It is shown here that the value of a has a significant effect on the localisation length. The ratio between the two harmonics in the ratchet potential is an important parameter in the correction term to the diffusion constant (equation 4.51) for low values of K. Numerically, for values of $a = 1.6$ compared to $a = 0.4$, there is a 25 percent increase in classical ratchet energy after ~ 4000 iterations when the effective kicking strength, $K_{eff} = 2.2$. However, when K_{eff} is increased to 12.2 this energy difference is reduced to the order of 1 percent. Since, as was shown in chapter 5, there is a strong current seen in the classical ratchet for values of $K \sim 1.6$ or $K_{eff} \sim 2.25$, a can be expected to be an important parameter when considering the quantum ratchet current. As a result the behaviour of the localisation length needs to be considered for varying a for this important range in K_{eff}. Figure 7.5 shows the behaviour of L and D_{cl} (both numerically calculated) as the parameter a is varied from zero (where the second harmonic is removed altogether) until a value $a = 2$. The form of the top and bottom plots in figure 7.5 show a close resemblance and give weight to the argument for the direct proportionality between L and D_{cl} shown in equation 7.4. Both graphs start at their lowest value for $a = 0$ where the potential takes the form of $\sin x$ alone. Saturation is seen for increasing a as the second harmonic begins to dominate the dynamics.

7.3.4 Dependence on ϕ

The variation of the localisation length with the parameter ϕ, the relative phase of the $\sin x$ and $\sin 2x$ terms in the potential, like the behaviour for a, follows closely the classical behaviour for the diffusion constant. In figure 7.6 it can be seen that as ϕ is increased from $-\pi$ to π the localisation length and classical diffusion constant both go from a minimum at $\pm\pi$ and rise towards maximum around $\pm\pi/2$ before falling to another minimum at zero phase difference. It can be noted that the minima of the curves (smallest localisation length and diffusion constant) roughly correspond to maximum spatial asymmetry and maximum ratchet current. Conversely the maxima in the plots matches zero ratchet current and maximum symmetry. These trends are

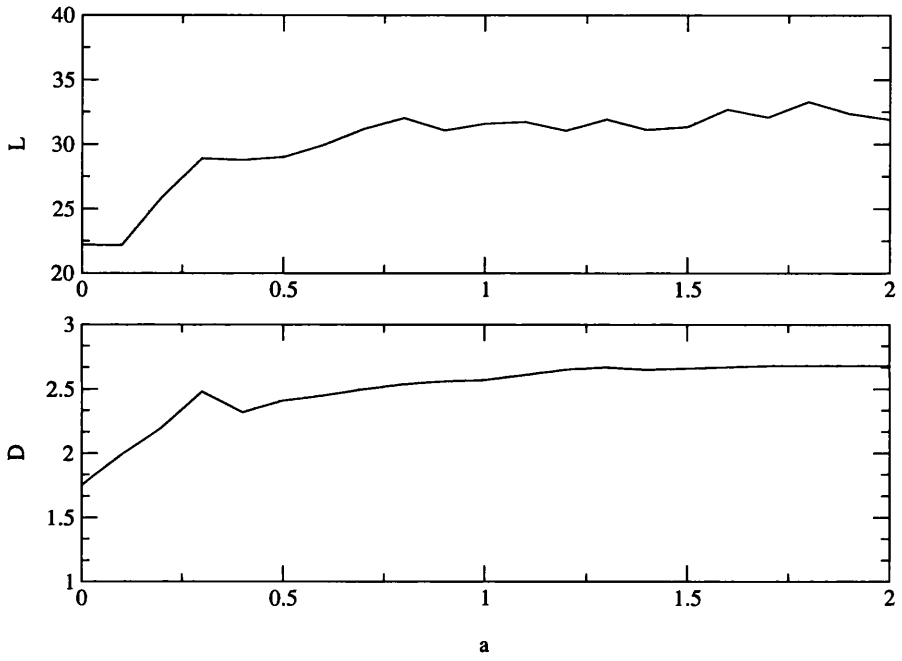

Figure 7.5: Demonstrates the same trend for increasing a in both the quantum localisation length and the classical diffusion constant. This shows that the variation of localisation length with a can be traced to a classical effect. The explanation for the shape of both plots can be seen from equation (4.51) where a is in the argument of second Bessel function in the product of Bessel functions.

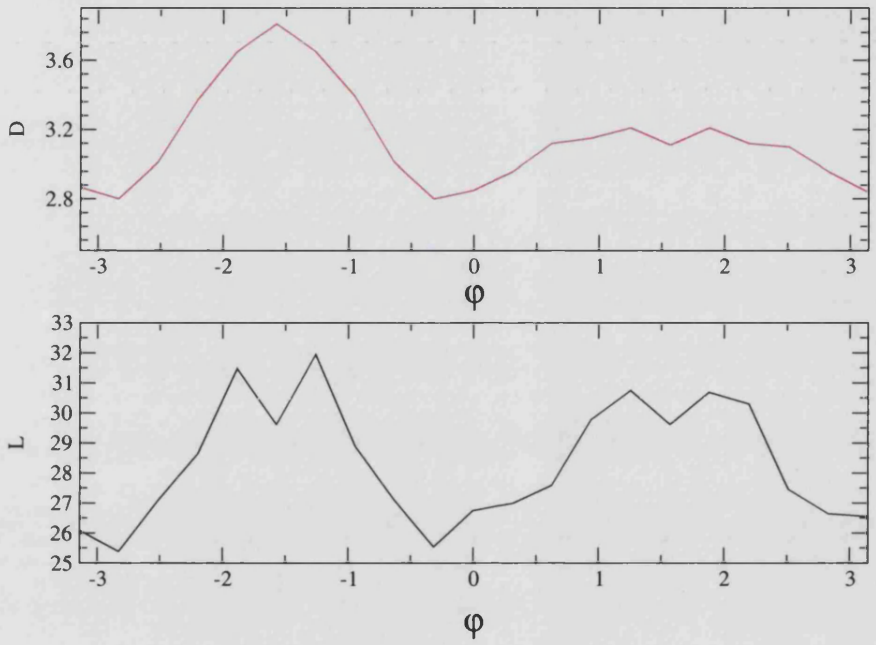

Figure 7.6: Shows that again the variation in localisation length for varying ϕ has classical roots. Note that in the figure the phases which produce maximum asymmetry and ratchet current have the largest L. Each graph was produced for $K = 1.7$, $a = 0.5$, $b = 0.1$ and $N = 3$. The quantum plots are for $\hbar = 0.5$

explained by noting that the correction to the diffusion constant with respect to ϕ acts to reduce the diffusion and that maximum correction is seen at $\pm\pi$ and 0. Both plots in figure 7.6 were calculated with $N = 3$, $a = 1/2$, $K = 1.7$ and $b = 0.1$. For the quantum plot $\hbar$ was set to 0.5.

7.3.5 b - Dependence

As for ϕ and a discussed above, b, the deviation from period one kicks, also affects the correction terms in the classical diffusion constant for small values of K_{eff},

however, it does so to a lesser extent. As for a this parameter also forms part of the arguments of the Bessel functions in equation (4.51) and is in fact seen in all terms in the $C(2,p)$ correction term. What might initially be expected to be a complex behaviour for the classical D_{cl} as b is varied turns out to be a simple smooth fall-off in D_{cl} as b is increased from 0 to 0.30, shown in the lower panel of figure 7.7, in fact the variation in D_{cl} becomes almost constant for values of $b > 0.05$. The quantum behaviour of the localisation is the same general form as predicted from equation 7.4, but is somewhat more erratic. This volatility could be due to quantum sensitivity to the changes in the kick to kick time scales as the quantum behaviour is dependent on the time periods in the system. The value of $\hbar = 1/2$ was again used in the numerical calculations performed for the localisation plot in figure 7.7, other system parameters take the values $K = 1.8$, $a = 0.5$, $N = 3$ and $\phi = 0$.

7.3.6 Variation of N

Perhaps the most significant of all the system parameters with regard to the localisation length is N the number of sequence kicks. For an N-kick cycle the kicks come at times: $T = 1 + (N/2 - 1)b, ..., 1, ...1 - (N/2 - 1)b$. So it is clear the value N determines the overall system periodicity in time. The system's time periodicity is related the value of the scaled Planck's constant for the system. The effect of doubling the time period for the system, or doubling the value of N, is equivalent to reducing the value of $\hbar$ by two: in the quantum evolution T and $\hbar$ appear as a product in $U^{tot}_{free} = \exp(-i(l+q)^2\hbar T)$. Figure 7.8 shows the localisation length plotted against increasing N and gives the expected linear relationship. A new approximation for the localisation length for the CDW-QKR can now be defined,

$$L = \frac{\alpha_N D_{cl}}{\hbar} N. \tag{7.5}$$

The gradient from figure 7.8 gives a value $\alpha D_{cl}/\hbar = 13.18$. For the system parameters used, $K = 2.5$, $a = 1/2$ (which from equation (4.3) gives the quasi-linear approximation to the diffusion as $D^{ql}_{cl} = 6.25$), $b = 0.1$ and $\hbar = 1$ and writing $\alpha_N = \alpha/N \sim 2.13$ from previous results, expression 7.4 gives a gradient of 13.31 which is in good agreement with the result from figure 7.8. The variation of the classical diffusion constant

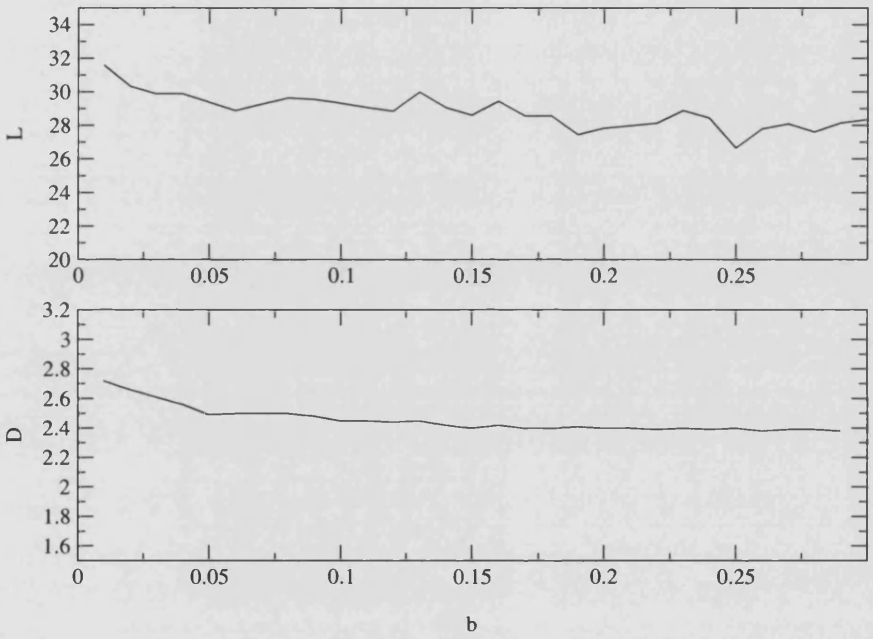

Figure 7.7: As with the values of ϕ and a the graph shows the variation in the localisation length compared to classical diffusion constant. The lower panel shows classical D_{cl} plotted against b. Once again the quantum behaviour mimics the classical. However, the top panel quantum plots shows a much more erratic behaviour which can be argued to be as a result of the quantum system's time sensitivity. Both plots were calculated numerically for values of $K = 1.7$, $a = 0.5$, $\phi = 0$ and $N = 3$. The quantum plots takes a value of $\hbar = 0.25$.

with N shows an entirely different behaviour. This underlines the quantum nature of the effect of varying N. The classical behaviour grows rapidly with increasing N for N small, but quickly saturates at $N = 8$. This can be explained by considering that with each additional increase in N there will be proportionally smaller influence from the new 2-kick correlation terms introduced into the diffusion constant.

7.4 Quantum Ratchet Current

For sufficiently long break times the current for the ratchet in the quantum regime follows closely the behaviour of the classical ratchet. Each classical system parameter (except N), when varied, will affect the magnitude and direction of the final current in a similar way to those seen in chapter 5. This result is due to the classical origin of the ratchet effect. In the quantum ratchet the asymmetry in the diffusion constant with respect to p means that negative momentum states will gain more energy than their positive momentum counter parts, in complete analogy to the classical asymmetric momentum distribution. Rather than effectively repeating all the results from chapter 5 again in this chapter, as an illustration, the quantum ratchet current for various ϕ is shown in figure 7.10. The reader is referred to figure 5.8 for a qualitative comparison.

However, if the system parameters are chosen such that the localisation length and hence the quantum break time are short, the momentum wavefunction can localise before sufficient asymmetry has been built up across the momentum states of the system. This freezing out of the ratchet momentum asymmetry, if it occurs well before t_r, prevents any significant ratchet current being produced in the quantum system. The effect of dynamical localisation is not necessarily a negative phenomenon for the quantum ratchet current and can in fact be used advantageously. The effect of dynamical localisation can be used to enhance the ratchet effect by limiting the energy growth beyond the ratchet time, t_r. The classical momentum distribution continues to grow indefinitely as the atoms gain more and more energy with each kick, hence, the classical trajectories become very spread out in momentum space. After many kicks the net current of the ratchet is very small compared to the total energy, so the effective asymmetry in the momentum distribution can be considered

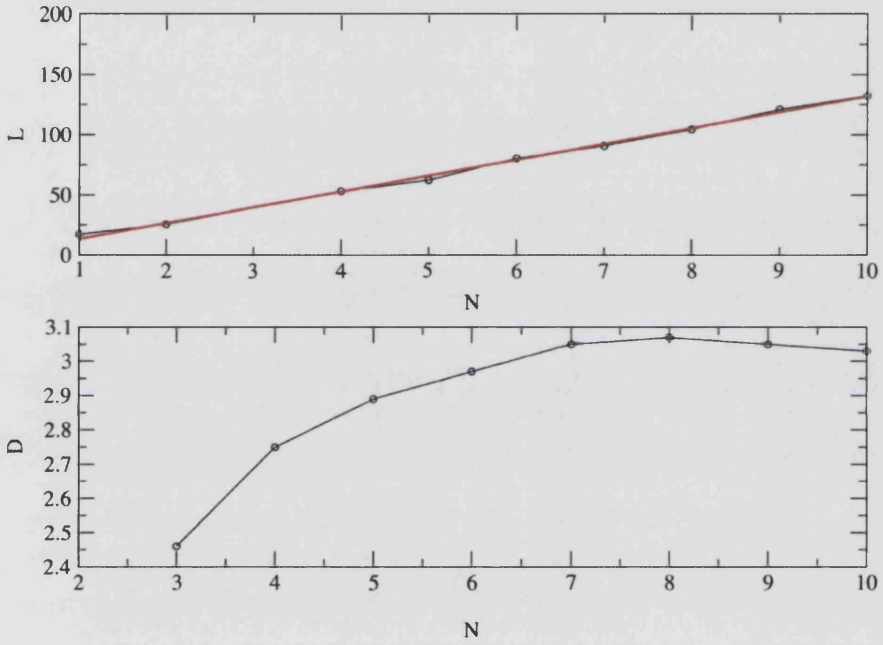

Figure 7.8: The variation of the system parameter N produces the most marked variation in the localisation length. The quantum results vary dramatically from the classical. The gradient of the quantum line is measured at ~ 13.18 which is consistent with previous numerical results and the Shepelyanski relationship, which together produce a prediction of 13.31 for the gradient. The system parameters used were $K = 2.5$, $a = 0.5$, $\hbar = 1$, $b = 0.1$ and zero phase. This system parameters were mirrored in the classical calculation in the lower panel which shows only a very small increase in D with increasing N.

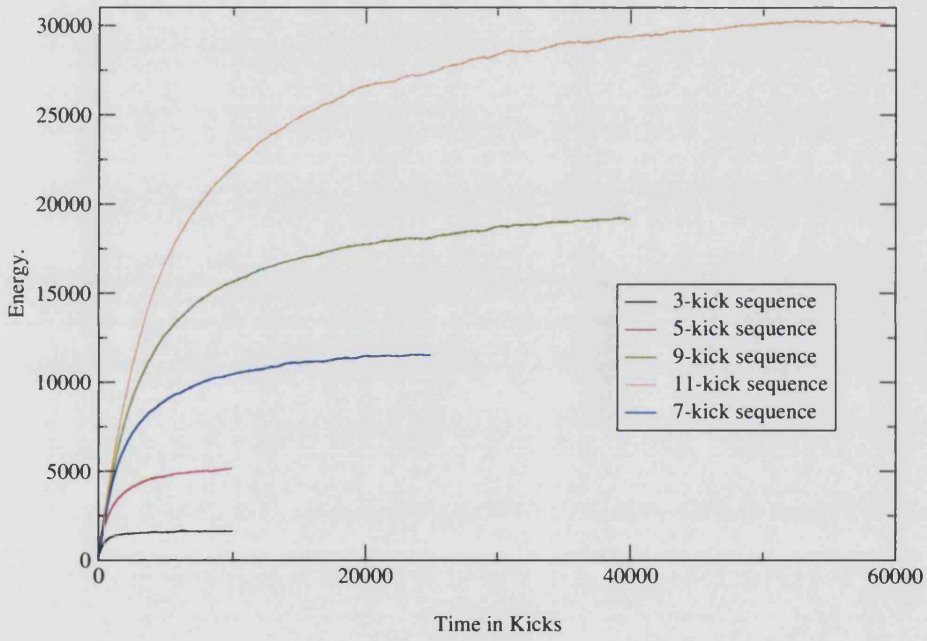

Figure 7.9: The figure shows how quantum break time increases with number of kicks in sequence. The break time is shown to increase significantly, for the ratchet parameters $K = 2$, $b = 0.1$, $a = 0.5$ and zero ϕ.

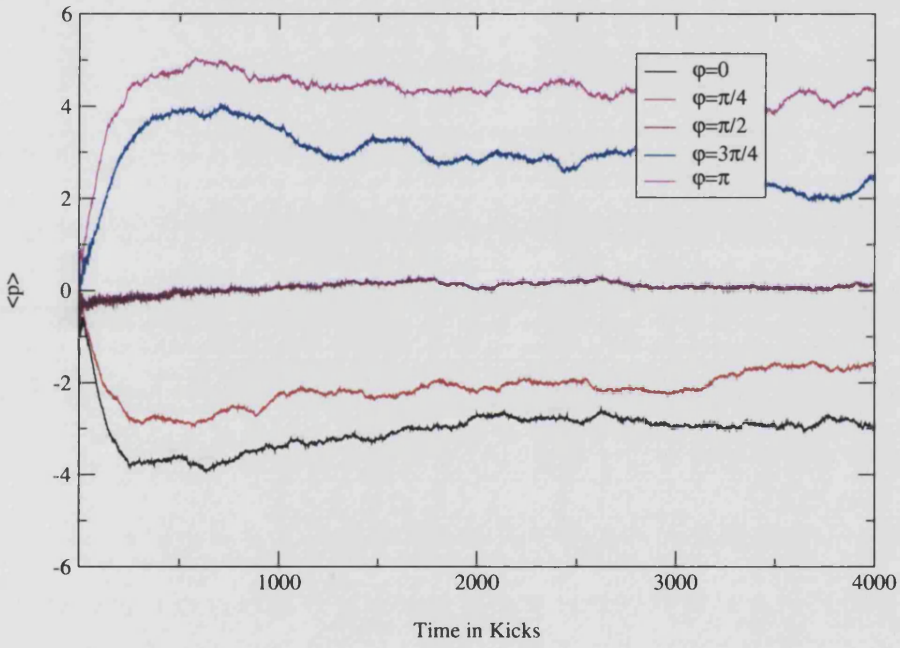

Figure 7.10: (a) Quantum graph of $\langle p \rangle$ vs time in kicks for system parameters $K = 1.8$, $\phi = 0$, $a = 0.5$, $\hbar = 0.25$, $b = 0.1$ and varying phase. The plots shows agreement with the classical behaviour - current is reversed for $\phi > \pi/2$. Also current magnitudes match well with larger currents seen for positive net currents.

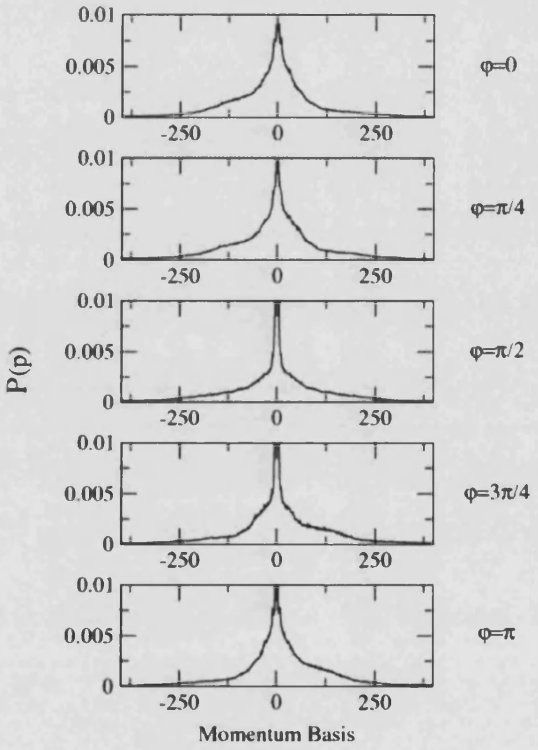

Figure 7.11: Quantum probability distributions for $K = 1.6$, $b = 0.1$, $a = 0.5$, $\hbar = 0.25$ and changing ϕ for t t^*. In the discretised momentum basis, $\psi = \sum_p e^{ipx}$, $P(p) = |A(p)|^2$. The asymmetry in momentum can be seen to reverse as the phase is increase. The greater the asymmetry matches to greater ratchet current.

to be small. By taking advantage of the quantum effect of dynamical localisation, the effective quantum momentum asymmetry can be kept as high as possible by freezing the momentum distribution of the system. In turn this limits the energy growth after t^* has been reached. The ratchet effect can, therefore, be enhanced by the effect of dynamical localisation. The quantum dynamics merely mimic the classical, then become frozen in time after t_r is reached. In the quantum ratchet a meaningful way to quantify the asymmetry is to use a re-scaled momentum such that $p_L = \langle p \rangle / L$. This value tends to a constant for long times $t > t^*$. It is this value that should be maximised for the best experimental signature of the ratchet.

7.5 Quantum - Classical Comparison

It is now clear that a good understanding of how system parameters affect both the classical and quantum behaviour is needed to produce the optimum current from the quantum ratchet. Figure 7.12 shows plots of quantum final $P(\psi(p)).p$ for various $\hbar$ versus classical $N(p).p$ after varying number of kicks (t_{cl}) corresponding to t^* for each $\hbar$. The figure demonstrates well the matching between the classical and quantum distributions as t_{cl} is matched to t^*. Also clear is the visible *washing out* of momentum asymmetry as the system energy is allowed to grow for the high values of t^* corresponding to the bottom panels in the figure. The asymmetry built up in momentum up until the ratchet time t_r is dwarfed when the system evolves for a much longer time. This corresponds to values where t^* is significantly larger than t_r. It would seem logical that in order to maximise the current ($\propto t_r$) to total energy ($\propto L$) ratio resulting from the ratchet, parameters should be chosen to set the ratchet time t_r and the quantum break time t^* to be roughly equal. Setting these two times equal should not only allow all possible momentum asymmetry to accumulate but also halt the energy growth of the system at that point. Some system parameters will be set according to the classical behaviour: there would be little point choosing a value for K that produces no momentum asymmetry classically as no current would be produced no matter how well t_r and t^* are matched.

Figure 7.13 displays the variation of average quantum momentum in the top panel

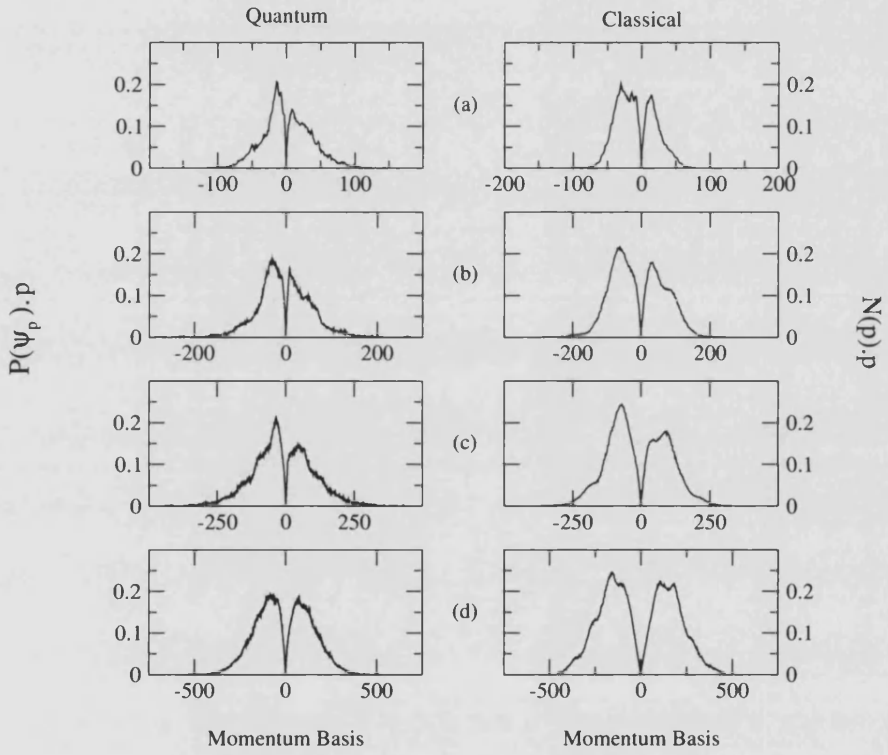

Figure 7.12: Shows corresponding momentum distributions for classical and quantum regimes. Each plot was run from system parameters taking the values $K = 2.0$, $b = 0.07$, $a = 0.5$, $\phi = 0$ and $N = 3$. The results show how for lower and lower values of $\hbar$ the quantum system evolves as the classical does for longer times. The lower plots for $\hbar = 0.125$ shows how the asymmetry in the system can become small compared to the spread in the wavefunction. The optimum condition is to arrest the wavefunction spread just as maximum asymmetry is accumulated.

Table 7.1: displays the quantum localisation and diffusion constant maxima and minima for all system parameters. Also comment is made as to whether the quantum behaviour follows that seen in the classical system.

Parameter	L (min)	D (min)	Quant. Class. Correspondence
N	1	3	no
a	0	0	yes
b	$b > 0.1$	$b > 0.1$	yes
ϕ	$0, \pm\pi/2$	0	yes
K	low K	low$K$	yes
$\hbar$	large $\hbar$	no effect	no

against the classical results from chapter 5 in the lower panel. While the quantum and the classical curves have the same basic shape, sharing the same axis crossings with current reversals at $K = 2.6$ and the same regions for their maxima and minima, there are some important differences. The quantum plots in the top panel show an improving fit to the classical results for decreasing $\hbar$. This shows the interplay between the two time scales t_r and t^*. The classical curve for matching system parameters has a minimum at $K = 1.5$. For each successive reduction in the value of $\hbar$ the break time is increased. For the low $K \sim 1.5$ and for $\hbar = 0.125$ the quantum wavepacket is allowed to evolve for long enough (i.e. t^* is sufficiently long) for all the possible momentum asymmetry (from the momentum dependent diffusion) to be built in. This is demonstrated by minima at matching values of K for the classical and quantum $\hbar = 1.125$ curves. In the $\hbar = 0.25$ and $\hbar = 0.5$ plots, for this value of K, the value of t^* is too short and the wavepacket localises before t_r. As K is increased for these higher $\hbar$ plots the classical dynamics are recovered at the point where $t^* > t_r$. For higher $\hbar$ higher values of K are required for this inequality to be met. Classically higher values of b lead to t_r small and as a result the current reversal after $K = 2.6$ shows only a very small positive current for $b > 0.1$.

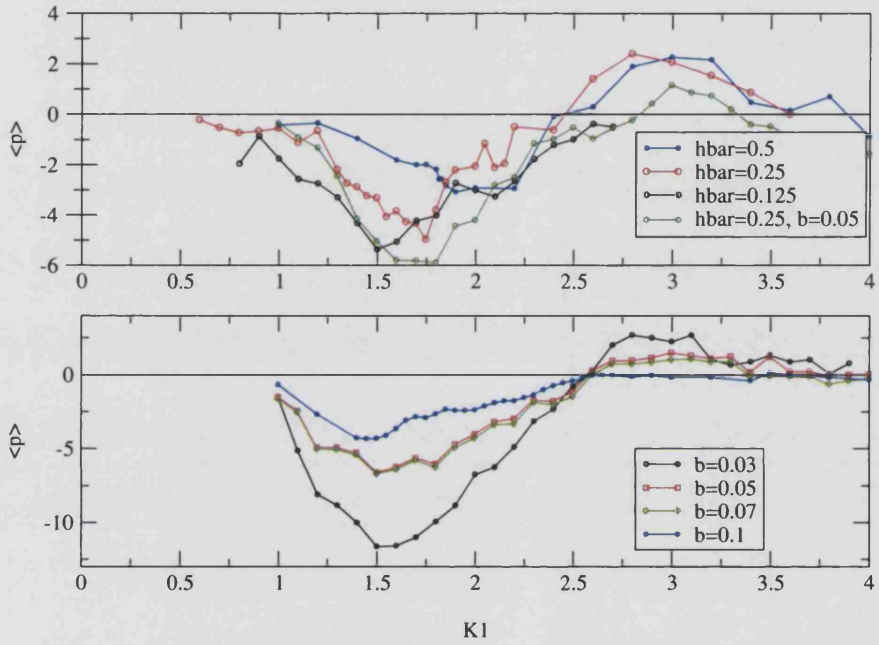

Figure 7.13: Displays average ratchet final momentum against variations in the stochasticity parameter K. The figure shows in the upper panel quantum results for $b = 0.1$ for several different values of $\hbar$. When compared to the classical plots in the lower panel for varying b insight is gained into the interplay between the time scales t_r and t^*. In the quantum plots the local minimum of the curve move closer and closer to that of the classical results for smaller $\hbar$. For higher $\hbar > 0.5$ the value of t^* is too short and insufficient asymmetry is built up resulting in small net current. It requires a higher K for the quantum to 'catch up' with the classical. For $\hbar = 0.125$ the value of t^* has met or exceeded t_r and the quantum current matches the classical for $K \sim 1.6$. Both plots show a current reversal after $K = 2.6$. The net classical current is reduce for increasing b corresponding to lower t_r at high K.

7.6 The Optimum Quantum Ratchet

To produce the best quantum ratchet (i.e. the set of system parameters which would produce the clearest experimental signature of non-zero current) values for $t_r > t^*$ must be met as well as the second condition, maximise $p_L = \langle p \rangle / L$. Firstly, in order to maximise the value p_L, parameters for which L shows the greatest sensitivity must be chosen carefully. Hence, the value for K should be chosen to be small, therefore the maxima or minima for $\langle p \rangle$ corresponding to the lowest K so, $K \sim 1.6$ is chosen. Happily this also produces the greatest current magnitude. The value for $\hbar$ should not be too small due to the inverse relationship with L. A value of $\hbar = 0.5$ is suggested as this also produces a sizeable quantum current at $K = 1.6$, values of $\hbar$ greater than this localise too quickly preventing sufficient asymmetry build up. Also, N is chosen as $N = 3$ as not only does this provide by far the smallest L (as there is a linear relationship $L \propto N$) but also the maximum classical current. The parameter a should be set to achieve maximum current (as the is a relatively small penalty in increased L) which from chapter 6 was seen to be $a = 0.4$. Parameters responsible for current inversions should be chosen such that maximum current is achieved, so ϕ is chosen as zero. The value for b should be set below a minimum value which can be approximated as follows: for $t_r > t^*$,

$$\frac{2\pi}{Db^2} > \frac{L^2}{D} \tag{7.6}$$

so, from equation 7.5,

$$\frac{2\pi}{\alpha_N^2} > \frac{D^2 b^2 N^2}{\hbar^2}. \tag{7.7}$$

α_N has been numerically estimated at 2.1, so,

$$\frac{DbN}{\hbar} < \frac{\sqrt{2\pi}}{2.1}, \tag{7.8}$$

so putting in $K = 1.6$, $N = 3$ and $\hbar = 0.5$ one finds that $b < 0.08$.

There is a good argument for choosing a value of b as close to this maximum limit as possible. Before t_r is reached the ratchet current is increasing, or, the particles are subject to a net acceleration. It is noticed that although for smaller b the ratchet time is longer, resulting in greater final classical currents, the initial gradient on the $\langle p \rangle$

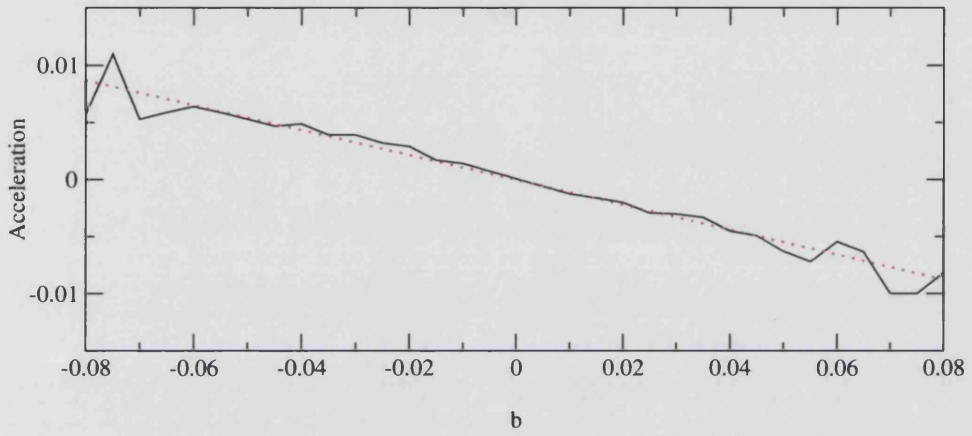

Figure 7.14: Shows the initial ratchet acceleration for $t < t_r$. System parameter values used are $K =$, $a = 0.5$, $N = 3$, $\phi = 0$.

vs. t curves is higher for higher b. This can be expected, as at the ratchet saturation time, t_r, which is $\propto 1/b^2$, the final $\langle p \rangle$ is reached which is $\propto -1/b$, from figure 5.4. The average gradient up until t_r is given by $\langle p \rangle / t_r \propto b$. Using the analytical fits in figure 7.14 and the ratchet parameters of the plots, the constant of proportionality is estimated ~ -0.1. The average gradient for $t = t_r$ is plotted (classically) for values of $-0.08 < b < 0.08$ in figure 7.14.

Experimental constraints need to be considered for the proposed kicked optical lattice experiment: there may be limiting factors on measurement magnitudes and

experimental time scales. Firstly, what momentum range can be feasibly measured? A typical CCD camera used in atom optics experiments has a width corresponding to $\pm 200\hbar k_L$ [112]. Which in the dimensionless units used here means a momentum scale of ± 100 momentum units at $\hbar = 1$. So, L should be restricted to be less than 100, which is consistent with the parameter values listed above. Secondly, the experimental time scale sets a limit for the number of kicks at $\sim$ 1000 before the atoms move away from the centre of the laser beam. This time scale is also consistent with the selected parameter range.

7.7 Conclusions

In summary, in this chapter a numerical study of all parameter dependencies for L has been carried out. A new form of the well known Shepelyanski relationship has been derived numerically. Also a comparison between the classical and quantum times scales of t_r and t^* is given, classical and quantum momentum evolutions are compared in figure 7.13. Ratchet current numerically calculated for a range of quantum parameters in figure 7.14 showing the best quantum current and a closer quantum correspondence to the classical behaviour as $\hbar$ is reduced. Finally, a range of experimental system parameters are suggested (in dimensionless units) to produce the clearest experimental signature for the ratchet effect for a kicked optical lattice experiment.

Chapter 8

Conclusions

8.1 Overview of Completed Work

A new type of ratchet system has been presented, modelled and analysed in detail. The chirped double well kicked ratchet (CDW-KR) is a noise-free, Hamiltonian, dissipationless, fully chaotic ratchet. This type of system was previously thought to be non-current producing. In this thesis the CDW-KR is demonstrated both numerically and analytically to be current producing. In fact, the CDW-KR was not only shown to produce a net current for the correct parameter values, but, current reversals as some of these parameters are varied. This is the first system of its type and the mechanism by which non-zero current is produced is quite generic. As a result similar behaviour can be expected in other systems of its type, [69].

The CDW-KR is also experimentally realisable and was actually inspired by the recent developments in the area of atom optics, expanded on in chapter 2. The Hamiltonian for the system was derived from consideration of cold atoms in an optical lattice. Also, system parameters are estimated at the end of chapter 7 that should provide the best experimental signature for detection of non-zero current.

The system was analysed in both the classical an quantum regimes with each system parameter considered in turn. Classically the parameters were classified as those whose variation produces a current reversal and those that are non-current reversing. Parameter values are also given that maximise t_r and $\langle p \rangle$. Quantum

mechanically the ratchet effect was found to be enhanced for well chosen parameters. This is due to the freezing of the momentum space wavefunction in time as the system is dynamically localised. This effect allows for the asymmetry in the system to be maximised for the best experimental detection. The localisation of the CDW-QKR was examined in detail. All trends that were shown in numerical simulations were explained physically and with reference to the system diffusion constant. A numerically derived modified Shepelyanski relationship was presented which follows all trends predicted in previous work. All codes written to perform the numerical calculations in this thesis were developed in FORTRAN 90.

The ratchet mechanism for the CDW-KR was explained in terms of asymmetric diffusion in momentum before the onset of dynamical localisation. The momentum dependent diffusion constant was given, up to the 2-kick correlation correction term, as well as a qualitative argument as to the origin of the *ratchet terms*. This was verified by numerical calculations of energy for positive and negative momentum particles respectively. These calculations showed the striking splitting of the positive and negative momentum curves over short time scales, see figure 5.2.

8.2 Points of Interest

The most significant findings in this thesis are reiterated here:

1. The discovery and analysis of a new ratchet type.
2. This ratchet is quantum enhanced, fully chaotic, experimentally realisable and noise free.
3. The ratchet displays the dynamical phenomena of current reversal and a new momentum dependent quantum localisation.
4. A modified Shepelyanski relationship including the parameter N.
5. The mechanism for the ratchet is explained in terms of momentum dependent diffusion and is found to be generic for its type.

6. System parameters are proposed to produce the optimal experimental ratchet signature.

8.3 Future Directions

There are possibilities to extend the work presented in this thesis in the following ways. To better simulate the proposed experimental work the replacement of the δ-kick by an experimentally feasible pulse of finite duration could be included. Classically this is shown to produce a modified momentum dependent K_{eff} which scales as a sinc function. In the resulting phase space features the reappearance of KAM tori at high values of momentum is found, [24].

The addition of noise into the system may well be of significant interest. Could weak noise enhance transport properties in the ratchet without completely destroying the quantum dynamical localisation effects? Much work has been done with noise in the standard kicked rotor. This work could be extended to the ratchet system proposed here.

The dynamical localisation in the ratchet was found to be momentum dependent. Strongly localised states occur at diffusion constant minima in p, where as more weakly localised states are observed where the diffusion constant peaks. The study of Floquet states and energy level dynamics may prove interesting. The possibility of new level statistics for a ratchet system of this type could be investigated.

Bose-Einstein condenstates (BEC's) have been achieved in an optical lattice, [114]. The inclusion, in the system Hamiltonian, of an extra non-linear term from the BEC could destroy the dynamical localisation in the system if it is too large. Further work in this area could answer the question: Could a BEC be survive in the CDW-QKR in devices such as *atom chips*? Conversely, would ratchet transport survive the non-linearity in the Gross-Pitaevski equation?

8.4 Possible Future Applications

The momentum dependence of the diffusion constant allows a possible application for the CDW-KR and other systems of this type, [69]. Since the localisation length in the quantum system are dependent on the local diffusion constant (in momentum), both the rate at which energy is absorbed and the length of time this energy is absorbed for are controlled by a particle's initial momentum. As a result atoms started at one momentum may pass through such an atom optic device relatively unaffected compared to atoms at different starting momenta. This forms a *velocity selector* [69] which could have a potential application in atom chips. Atom chips are a result of recent work in atom optics where cold atoms are trapped and guided by fields above a solid substrate, [113, 114]. Possibly, one day, an atom optics analogy for an integrated circuit will be possible where devices, like the velocity selector, may provide an important rôle in trafficking atoms. Already experimental work is being carried out taking advantage of the momentum dependence of the diffusion constant for this type of system, see figure 8.1. In the figure momentum dependent variations in diffusion are used to produce non-zero currents for a double kick system. Initial wavepackets are started at different momenta to produce asymmetric distributions in momentum, much like those presented in this thesis.

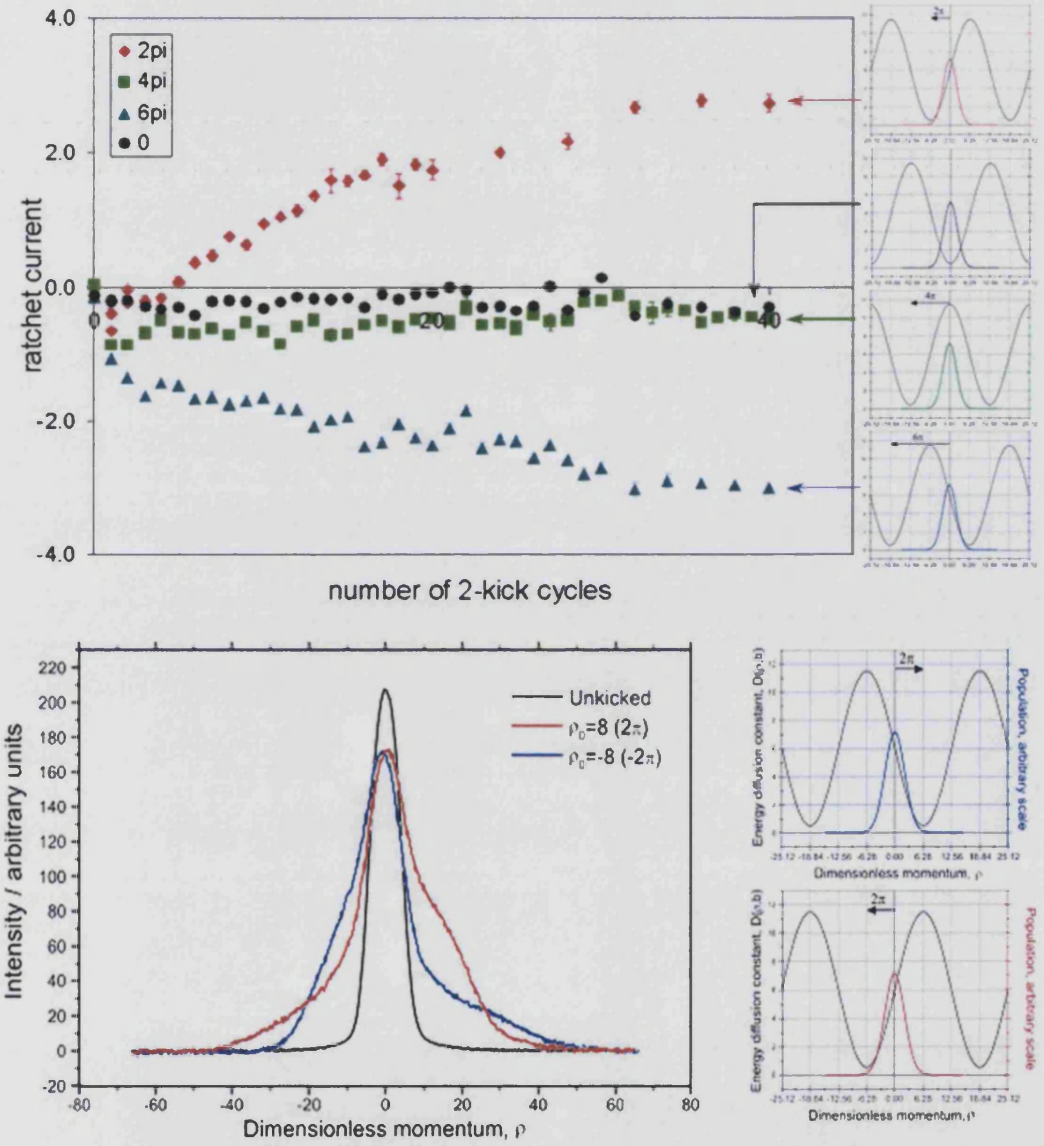

Figure 8.1: In the top panel currents for varying initial momentum starting points are displayed. Strong change in momentum is seen for those starting conditions which begin where there is a strong gradient in the momentum diffusion constant. The lower panel shows the momentum asymmetries corresponding to the strong currents seen above, [112].

Chapter 9

Appendix: Papers

Two Papers are presented in this appendix:

Proposal for a Chaotic Ratchet Using Cold Atoms in Optical Lattices
T. S. Monteiro, P. A. Dando, N. A. C. Hutchings and M. R. Isherwood
Physical Review Letters
Volume 89, Number 19

Chaotic Hamiltonian Ratchets for pulsed periodic double-well potentials : classical correlations and the ratchet current
N. A. C. Hutchings, M. R. Isherwood, T. Jonckheere and T. S. Monteiro
To be submitted to Physics Review E.

Proposal for a Chaotic Ratchet Using Cold Atoms in Optical Lattices

T. S. Monteiro, P. A. Dando, N. A. C. Hutchings, and M. R. Isherwood
Department of Physics and Astronomy, University College London, Gower Street, London WC1E 6BT, United Kingdom
(Received 5 April 2002; published 22 October 2002)

We investigate a new type of quantum ratchet which may be realized by cold atoms in a double-well optical lattice, pulsed with unequal periods. The classical dynamics is chaotic and we find the classical diffusion rate D is asymmetric in momentum up to a finite time t_r. The quantum behavior produces a corresponding asymmetry in the momentum distribution which is "frozen-in" by dynamical localization provided the break time $t^* \geq t_r$. We conclude that the cold atom ratchets require $Db/\hbar \sim 1$, where b is a small deviation from period-one pulses.

DOI: 10.1103/PhysRevLett.89.194102 PACS numbers: 05.45.Mt, 05.40.Jc, 05.60.-k, 32.80.Pj

Cold atoms in optical lattices provide an excellent experimental demonstration of the phenomenon of *dynamical localization* [1,2]. Dynamical localization (DL) has been described as the so-called "quantum suppression of classical chaos." In the usual realizations, a periodically driven or kicked system makes a transition to chaotic classical dynamics for sufficiently strong perturbation. The classical energy is unbounded and grows diffusively with time. For the corresponding quantum system, in contrast, the diffusion is suppressed after an $\hbar$-dependent time scale, the "break time" t^*. The final quantum momentum distribution is localized with a characteristic exponential profile. The formal analogy established with Anderson localization [2] forms a key analysis of this phenomenon. A series of recent experiments on cesium atoms in pulsed optical lattices [3] gave a classic demonstration of this effect.

The possibility of experiments with asymmetric lattices, in particular, with asymmetric double wells [4,5], leads us to investigate the possibility of constructing a "clean" atomic ratchet, where the transport results purely from the chaotic Hamiltonian dynamics, with no Brownian or dissipative ingredients. Ratchets are spatially periodic systems which, by means of a suitable spatial-temporal asymmetry, can generate a current even in the absence of a net force. There is already an extensive body of work on Brownian and deterministic ratchets with dissipation [6,7], driven by the need to understand biophysical systems such as molecular motors and certain mesoscopic systems. Some of this work encompasses the quantum dynamics [8]. For a full review see [9]. However, to date there has been very little work on Hamiltonian ratchets. One notable exception is the work by Flach *et al.* [10] where the general form of the spatial and temporal desymmetrization required to generate transport was investigated. The only substantial study of *quantum* Hamiltonian ratchets, however, is the work of Dittrich *et al.* [11] which showed how transport can occur in mixed phase spaces. They demonstrated that transport is zero if starting conditions cover all regions of phase space uniformly. A key result was a sum rule showing transport in the chaotic manifold is balanced by transport in the adjoining regular manifolds (stable islands/tori). Very recently [12], it was shown that a kicked map with a "rocking" linear potential leads to confinement in the chaotic region between a pair of tori which are not symmetrically located about $p = 0$.

Here we propose a new type of Hamiltonian ratchet which, classically, is completely chaotic. This ratchet is not inconsistent with the rules established in [10,11], but has a quite different mechanism. It is the first example of a clean, nondissipative ratchet which is fully chaotic and, hence, does not require initial preparation on a specific set of islands/tori.

The basic mechanism relies on a hitherto unnoticed effect. In brief: consider particles in the asymmetric lattice, subject to a repeating cycle of kicks, of strength K_{eff}, perturbed from period one by a small parameter b. We find that the *classical* diffusion rates for positive and negative momenta (D^+ and D^-, respectively) are (in general) different *up to a finite time*, t_r. For $t < t_r$, an asymmetry in the classical momentum distribution $N_{\text{cl}}(p)$ accumulates with kick number. Beyond this "ratchet" time t_r, the rates equalize, we have $D^+ \sim D^- \sim D$ (where $D \sim K_{\text{eff}}^2/2$ is the total diffusion rate), and the net classical current $\langle p_{\text{cl}} \rangle$ saturates to a constant, nonzero value. The energy, of course, continues to grow with time as $\langle p_{\text{cl}}^2 \rangle \sim Dt$. The corresponding quantum current depends on t^*/t_r: if the quantum break time is too short, no asymmetry in the quantum $N_{\text{qm}}(p)$ accumulates and there is no quantum transport. If $t^* \gg t_r$, the localization length L becomes large and the effective quantum momentum asymmetry $\sim \langle p_{\text{qm}} \rangle / L$ decreases. We find that $t_r \sim \frac{1}{b^2 D}$. A quantum ratchet will have the clearest experimental signature if $t^* \sim t_r$. Since $t^* \sim D/\hbar^2$, the main conclusion of our Letter is that the cold atom ratchets need $Db/\hbar \sim 1$.

Consider the quantum dynamics for a Hamiltonian given by $H = \frac{p^2}{2} + KV(x) \sum_{n,i} \delta(t - nT_i)$. The ratchet potential is given by $V(x) = \{\sin x + a \sin(2x + \Phi)\}$. In the usual realization of DL, the quantum kicked rotor (QKR), the kicks are equally spaced. For the ratchet,

they are unequal but we can use a rescaled time such that, without loss of generality, we take $\langle T_i \rangle = 1$ over each cycle. We take a repeating cycle of "chirped" kick period spacings, $1 + jb$, $1 + (j-1)b \ldots$, $1 - (j-1)b$, $1 - jb$ where $j > 0$ is an integer and b is a small time increment. $N = 2j + 1$ for N odd and $N = 2j$ for N even. Then, our $N = 3$ cycle corresponds to a repeating set of kick spacings $T_1 = 1 + b$, $T_2 = 1$, $T_3 = 1 - b$ while an $N = 2$ cycle corresponds to $T_1 = 1 + b$, $T_2 = 1 - b$, and so forth.

The time-evolution operator for the ith kick of the nth cycle factorizes into a free and a "kick" part $U_i = U_i^{\text{free}} U^{\text{kick}}$. In the usual plane wave basis, for a given quasimomentum q, the matrix elements of U_i can be shown to take the form:

$$U_{ml}^{(i)}(q) = e^{-i[\hbar T_i (l+q)^2/2]} \sum_s e^{is\Phi} J_{l-m-2s}\left(\frac{K}{\hbar}\right) J_s\left(\frac{aK}{\hbar}\right), \tag{1}$$

where the J are ordinary Bessel functions. The time-evolution operator for one period $U(T = \sum_i T_i) = \prod_{i=1}^{i=N} U_i$. In the experiments, an important parameter is an effective $\hbar_{\text{eff}} = 8\omega_r T$, where ω_r is the recoil frequency. In [3], $\hbar_{\text{eff}} \sim 1$, so here we have considered the range $\hbar = 1 \rightarrow 1/10$.

In Fig. 1 we compared the evolution of a quantum wave packet with equal kick times ($T_i = 1$) with a corresponding unequal-kick case with $N = 3$, $b = 0.1$. Since $V(x)$ in general represents a double-well potential, we refer to it as the dw-QKR to distinguish it from the standard map case with $V = K \sin x$. We refer to the unequal-kick case as the chirped or cdw-QKR.

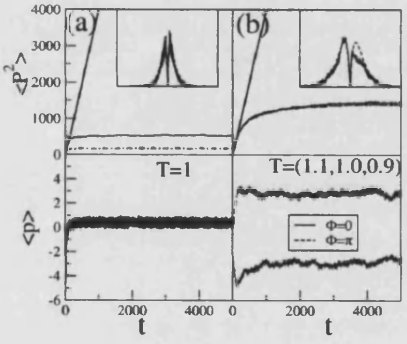

FIG. 1. Effect of equal and unequal kick spacings on a minimal uncertainty Gaussian wave packet with $\hbar = 1/2$ with initial $\langle p \rangle = 0$, for kick strength $K = 2$ and $a = 1/2$, for different Φ. (a) Evolution of energy and momentum for $T = 1$ (dw-QKR). (b) Evolution of energy and momentum for a repeating $N = 3$ cycle of kicks with $b = 0.1$, hence $T_i = 1.1, 1.0, 0.9$ (cdw-QKR). (a) and (b) show that there is no transport for the equal kick case, but that there is a substantial net momentum ($\sim$ constant if $t > t^*$) for the cdw-QKR. Setting $\Phi = \pi$ reverses the current relative to $\Phi = 0$. The insets show the first moment of the p distribution: The current is the difference in area between the positive p and negative p "bumps." The DL form $|p|.N(|p|) = \frac{|p|}{2L} \exp -|p|/L$ [with $L = 27.5 \sim 3.5 D_0/\hbar$ (see Fig. 3)] is superposed, showing the DL form is regained for large enough p.

The upper graph in Fig. 1 shows that, in both cases, the average *quantum* energy initially increases linearly, i.e., $\langle p^2 \rangle \sim Dt$. The straight line corresponding to the classical energy is also shown. Neglecting all classical correlations, we find $D \sim D_0 = K_{\text{eff}}^2/2$, where $K_{\text{eff}} = K\sqrt{(1 + 4a^2)}$. The Φ dependence lies in neglected correlations, which in this case appear as products of Bessel functions [13]. However, beyond a time scale $t \sim t^*$, the *quantum* energy saturates to a constant value $\langle p^2 \rangle \sim L^2$, where L is the localization length.

The dw-QKR shows a typical, exponentially localized, momentum distribution. However, for the cdw-QKR, the quantal $N(p)$ is evidently asymmetric, but regains the DL form at large p. There is no net current in the $T = 1$ case: asymptotically, $\langle p \rangle \simeq 0$. However, for the chirped case, for $t > t^*$, in general we have $\langle p \rangle \sim$ constant. A meaningful way to quantify the asymmetry is a rescaled momentum $p_L = \langle p \rangle / L$ which also tends to a constant for $t > t^*$ [e.g., $p_L \simeq 1/8$ in Fig. 1(b) for $\Phi = 0$]. Taking $\Phi = \pi$ reverses the symmetry of $V(x)$ and the direction of motion relative to $\Phi = 0$. Intermediate values of Φ typically give $\langle p \rangle$ within these extremes.

In summary, the cdw-QKR shows a ratchet effect *and* dynamical localization, with an asymmetric profile at short range, but a DL form for large p. The quantal current increases from zero for a finite time, then saturates to constant magnitude. This is surprising, since it is thought that in the fully chaotic regime a Hamiltonian ratchet current should not persist. In order to understand this behavior, we now compare with the corresponding classical current.

In Figs. 2(a) and 2(b) we show that, in fact, *both* quantum and classical currents $\langle p \rangle$ increase in magnitude, then saturate to a constant value after a finite time; but the saturation time is generally different: t^* in the quantum cases in Fig. 2(a) and another, ratchet time scale t_r in the classical cases shown in Figs. 2(a) and 2(b). Figure 2(a) shows, in particular, the dependence on $\hbar$. The $\langle p_{\text{qm}} \rangle$ are negligible for $\hbar > 1$ but increase rapidly with decreasing $\hbar$, up to $\hbar \sim 0.25$. This is important for any experiment : for these parameters ($D \sim 2.5$, $b = 0.1$), an experiment with $\hbar_{\text{eff}} \sim 0.8$ would show little asymmetry, but just halving $\hbar_{\text{eff}}$ to $\sim$0.4 would show substantial asymmetry. Beyond $\hbar \sim 0.4$, $\langle p_{\text{qm}} \rangle$ is comparable to the saturated classical value. But since the most experimentally "detectable" ratchet is one which maximizes the asymmetry $N(p)$, this means maximizing a rescaled momentum $p_L = \langle p_{\text{qm}} \rangle / L$, so there is no advantage in reducing $\hbar$ much below $\sim$0.4 since $L \sim \hbar^{-1}$. Figure 2(b) shows that, for a given b ($b = 0.05$ in this graph), the classical saturation time t_r falls with

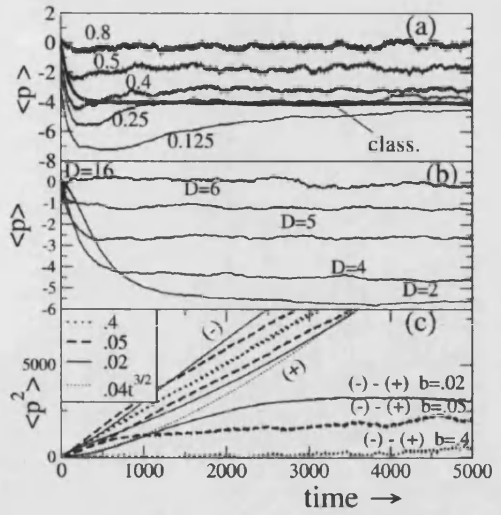

FIG. 2. Quantal versus classical ratchet currents are compared in (a) and (b) for $N = 3$. Both the classical and quantum $\langle p\rangle$ reach a constant value after a finite time (t^* and t_r, respectively). (a) The quantum current is very sensitive to $\hbar$ if the quantum (Gaussian) wave packet localizes before the classical equivalent saturates. The values of $\hbar$, ($0.8 \rightarrow 0.125$) are indicated. $K = 1.6$, $a = 0.5$ (hence, $D_0 \sim 2.5$), and $b = 0.1$. The asymptotic quantum $\langle p\rangle$ increases with $\hbar$ and "catches" up with the classical results for $\hbar \sim 0.25$ where $t^* \sim t_r$. (b) Evolution of $\langle p\rangle$ for a classical "wave packet" (500 000 particles with a Gaussian random distribution in x, p, of width $\sigma = 1.5$ for $b = 0.05$ but different D). The current increases and then saturates for $t > t_r \sim 1/(Db^2)$. (c) Differential classical diffusion rates $[D^+(t, b), D^-(t, b)]$: $\langle p^2\rangle$ is evaluated separately at each kick for particles with positive and negative momenta for $K = 1.6$, $a = 0.5$, $D_0 \sim 2.5$, and different b. We see that $\langle p^2\rangle^{\pm}$ diverge from linear growth by a quantity, which is similar in magnitude but opposite in sign for the negative and positive components. The + and − indicate $\langle p^2\rangle^+$, $\langle p^2\rangle^-$, respectively. But once $t > t_r$, we see linear growth: $D^+ \sim D^- \sim D \sim 2.5$. The lower graphs show $\delta(b) = \langle p^2\rangle^{(-)} - \langle p^2\rangle^{(+)}$ (for these parameters, $D^- > D^+$ so the current is negative). $\delta(b) \propto bt^{3/2}$ for small t.

increasing D. The fact that $\langle p_{\rm cl}\rangle$ saturates at all is surprising: after all, the ensemble of classical trajectories is continually expanding and exploring new phase-space regions corresponding to higher momenta.

While t^* is well studied, t_r is quite new; we find that it can be understood in terms of differential rates of absorption of energy for particles moving left or right. To illustrate this, we calculated—separately—$\langle p^2\rangle^{(-)}$ for those particles with $p < 0$ and $\langle p^2\rangle^{(+)}$ for those with $p > 0$. The results are shown in Fig. 2(c) for $D_0 \sim 2.5$ and different b. They are quite striking: $\langle p^2\rangle^{(-)}$ and $\langle p^2\rangle^{(+)}$ separate gradually, more or less symmetrically, about the line $\sim 2.5t$, but beyond a certain time, they run parallel to each other and their slopes become equal with $D^+ \sim D^- \sim 2.5$. Also in Fig. 2(c) we plot $\delta(b) = \langle p^2\rangle^{(-)} - \langle p^2\rangle^{(+)}$ for each b since this shows the saturation effect more clearly. We find numerically and from theory that, for small t, $\delta(b) \simeq b(D_0 t)^{3/2} f(K, a)$, where $f(K, a)$ is a function of K, a.

The so-called "quasilinear" approximation for the energy diffusion $D_0 \simeq K^2/2$ [14] neglects correlations between sequences of consecutive kicks; for the standard map, these give well known corrections to the diffusion constant in the form of Bessel functions: $D = \frac{K^2}{2}\{1 - 2[J_1(K)]^2 - 2J_2(K)\ldots\}$ [14,15]. These corrections have even been measured experimentally with cold cesium atoms in pulsed optical lattices [16,17]. For example, the $2J_2(K)$ term originates from two-kick correlations of the form $C(2) = 2\langle V'(x_i)V'(x_{i+2})\rangle$. In general, if we work out the change in $\langle p^2\rangle$ for successive kicks, we obtain a diffusion rate D which is the same whether we average the momentum from $0 \rightarrow \infty$ or from $0 \rightarrow -\infty$. Odd terms in p such as $\langle \sin 2p\rangle$ average to zero once the cloud has an appreciable spread, while the even terms $\langle \sin^2 p\rangle = \langle \cos^2 p\rangle \simeq 1/2$ are insensitive to the sign of p: in the standard map, $D^+ = D^-$. But if we consider the first kick of the nth cycle of the cdw-QKR, we have:

$$x_{n1} = x_{n0} + P_{n0}(1 + b), \tag{2}$$

$$P_{n1} = P_{n0} - KV'[x_{n0} + P_{n0}(1 + b)]. \tag{3}$$

The unequal kicks allow free evolution for an additional small distance $\delta_1 = P_{n0}b$. To first order,

$$P_{n1} = P_{n0} - K\{V'(x_{n0} + P_{n0}) + P_{n0}bV''(x_{n0} + P_{n0})\}. \tag{4}$$

Hence, we now have correlations which depend on the sign of p and which scale with b. More precisely, we have averages of typical form $I(p) = \langle \sin pb \sin^2 p\rangle$. For pb small, $I(p) \simeq \langle p_{\pm}\rangle b/2 \simeq \pm \frac{b}{2}\sqrt{D_0 t}$ when we average positive and negative momenta separately. The average over x yields a function $f(K, a)$. Hence, clearly the corresponding energy $\langle p^2\rangle^{\pm} \sim D_0 t \pm (D_0 t)^{3/2} b f(K, a)$. $f(K, a)$ is a very complicated function involving sums of products of Bessel functions [13], but yields good estimates of $\delta(b)$. In [18] we have investigated the rocking ratchet of [12] in the *chaotic regime* and found the same physics. We obtained excellent agreement between a curve $\propto bt^{3/2}$ and numerics and can predict successfully repeated current reversals without any detailed study of phase space.

For pb large, $I = \langle \sin pb \sin^2 p\rangle \simeq 0$, so there is no ratchet correction. The associated saturation time t_r is very important since then the classical ratchet speed reaches its maximum and for $t > t_r$, $\langle p_{\rm cl}\rangle \sim cst.$ We identify it as a point where $I \sim 0$; hence, we take $b\sqrt{\langle p^2\rangle^{(+)}} \sim \pi$ for the positive component and $b\sqrt{\langle p^2\rangle^{(-)}} \sim \pi$ for the negative component. For an order of magnitude estimate of the mean time scale involved, we take $b\sqrt{Dt} \sim \pi$. Hence, we obtain $t_r \sim \frac{\pi^2}{Db^2}$. In [12]

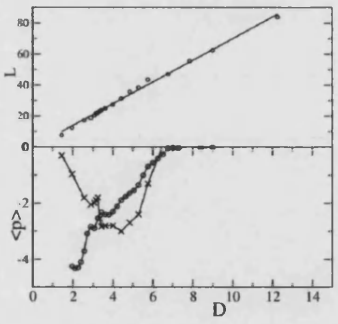

FIG. 3. (a) Relation between classical diffusion rate D and the quantum localization length L for the cdw-QKR. The solid line corresponds to $L = \frac{3.5D}{\hbar}$. (b) Current against D for a quantum wave packet (crosses) and a classical "Gaussian wave packet" (circles). The graph illustrates the fact that if the quantum break time is too short (low D) the quantum momentum is small, but catches up with the classical momentum at $t^* \sim t_r$.

a long-ranged periodicity in p, of order $2\pi/b$, was identified. We note that for our study of systems with zero initial current, this is not significant, since by the time the periodicity boundary is sampled $I(p) \simeq 0$. However, it is an important consideration if we start with nonzero initial current [18].

Numerically, we estimated $t_r \sim \frac{5}{Db^2}$ which is not inconsistent with the above. This explains the counterintuitive behavior that the larger deviation from period-one kicking (i.e., the larger b) give a smaller ratchet effect. Though the perturbation scales as b, the time for which it is important scales as b^{-2}.

For the standard map/QKR, there is a well known relation between the quantum localization length and the classical diffusion constant: $L \sim \frac{\alpha D}{\hbar}$, where the constant α was found to be $1/2$ [15]. The $N = 3$, $b = 0.1$ cdw-QKR takes a modified proportionality constant, i.e., $L \sim \frac{3.5D}{\hbar}$.

In Fig. 3(a) we plot a set of calculated L (which range from $L \sim 10$–80) against D for $\hbar = 1/2$ together with the line corresponding to $L = \frac{3.5D}{\hbar}$. The agreement is excellent. From $L^2 \sim Dt^*$ we obtain $t^* \sim 12D/\hbar^2$.

In Fig. 3(b), for the quantum distributions in Fig. 3(a), we have also plotted the current as a function of D, together with their classical equivalents, obtained from an ensemble of 500 000 classical particles. We see that the classical $\langle p \rangle$ fall monotonically with D, apart from fine structure which we attribute to cantori. The quantum results, however, for low D are much smaller than the classical values but increase in magnitude until there is a "crossover" point at $D \sim 3$, after which they are much closer to the classical values.

We do not expect perfect agreement with the classical results for $\hbar = 1/2$; a cleaner comparison might be obtained for smaller $\hbar$, but this might be harder to achieve in an experiment.

We estimate the quantum break time at the crossover $t^* \sim 12D/\hbar^2 \sim 150$ kicks. The ratchet time $t_r \sim 5/(Db^2) \sim 160$ kicks. Such good agreement is somewhat fortuitous, since there are larger uncertainties in the time scales. Nevertheless, it does provide us with a useful guide for the best parameters for an experiment.

So one of our key results is that the requirement $t^* \sim t_r$ implies that we need $Db/\hbar \sim 1$. The L values should, of course, be experimentally plausible ($L \sim 10$–100), so this places a constraint on $D/\hbar$.

In conclusion, we have proposed a mechanism for the first generic, completely chaotic Hamiltonian ratchet.

We thank Professor S. Fishman for helpful advice. The work was supported by EPSRC Grant No. GR/N19519.

[1] G. Casati, B.V. Chirikov, F.M. Izraelev, and J. Ford, in *Stochastic Behavior in Classical and Quantum Hamiltonian Systems*, Lecture Notes in Physics Vol. 93 (Springer, Berlin, 1979), p. 334.
[2] S. Fishman, D.R. Grempel, and R.E. Prange, Phys. Rev. Lett. **49**, 509 (1982).
[3] F.L. Moore, J.C. Robinson, C.F. Bharucha, B. Sundaram, and M.G. Raizen, Phys. Rev. Lett. **75**, 4598 (1995).
[4] C. Mennerat-Robilliard *et al.*, Phys. Rev. Lett. **82**, 851 (1999).
[5] We thank Dave Meacher for explaining possible experiments with driven double-well lattices.
[6] F. Julicher, A. Adjari, and J. Prost, Rev. Mod. Phys. **69**, 1269 (1997).
[7] J.L. Mateos, Phys. Rev. Lett. **84**, 258 (1999).
[8] P. Reimann, M. Grifoni, and P. Hänggi, Phys. Rev. Lett. **79**, 10 (1997); P. Reimann and P. Hänggi, Chaos **8**, 629 (1998).
[9] P. Reimann, Phys. Rep. **361**, 57 (2002).
[10] S. Flach, O. Yevtushenko, and Y. Zolotaryuk, Phys. Rev. Lett. **84**, 2358 (2000).
[11] T. Dittrich, R. Ketzmerick, M.-F. Otto, and H. Schanz, Ann. Phys. (Berlin) **9**, 755 (2000); H. Schanz, M.-F. Otto, R. Ketzmerick, and T. Dittrich, Phys. Rev. Lett. **87**, 070601 (2001).
[12] T. Cheon, P. Exner, and P. Seba, cond-mat/0203241.
[13] N. Hutchings *et al.* (to be published).
[14] A.J. Lichtenberg and M.A. Lieberman, *Regular and Chaotic Dynamics* (Springer-Verlag, New York, 1992).
[15] D.L. Shepelyansky, Phys. Rev. Lett. **56**, 677 (1986).
[16] B.G. Klappauf, W.H. Oskay, D.A. Steck, and M.G. Raizen, Phys. Rev. Lett. **81**, 4044 (1998).
[17] M.B. d'Arcy, R.M. Godun, M.K. Oberthaler, D. Cassetari, and G.S. Summy, Phys. Rev. Lett. **87**, 074102 (2001).
[18] M.R. Isherwood and T.S. Monteiro, physics/0206072.

Chaotic Hamiltonian Ratchets for pulsed periodic double-well potentials : classical correlations and the ratchet current

N.A.C. Hutchings,[1] M. R. Isherwood,[1] T. Jonckheere,[2] and T.S. Monteiro[1]

[1]*Department of Physics and Astronomy, University College London, Gower Street, London WC1E 6BT, U.K.*

[2]*Centre de Physique Théorique,Campus de Luminy case 907, 13288 Marseille cedex 9, France*

(Dated: May 5, 2004)

Abstract

We present analytical derivations of the diffusion rates, ratchet currents and timescales of a new type of chaotic Hamiltonian ratchet, introduced in [Phys. Rev. Lett. **89**, 194102 (2002)], with a proposed implementation using atoms in pulsed standing waves of light. The origin of this type of ratchet current is in asymmetric momentum diffusion rates which result when a 'double-well' lattice is pulsed with unequal 'kick' periods. The form of the new short-time correlations which modify the diffusion rates are derived. The resulting formulae for the classical energy diffusion rates are shown to give good agreement with numerical simulations. A closed analytical formula for the ratchet current is also obtained, which predicts correctly the current magnitudes and current reversals. The characteristic *ratchet time*, a classical timescale associated with the momentum-diffusion ratchet is derived analytically. The competition between the *ratchet time*, t_r, and the quantum break-time, t^*, is investigated further.

PACS numbers: PACS number(s): 03.65.Sq, 05.45.+b, 32.60.+i

I. INTRODUCTION

Recent advances in cold atom physics, such as techniques for manipulating atoms in optical lattices, have led to experimental implementation of a rich variety of quantum dynamical phenomena. One particular example is the successful demonstration of Dynamical Localization [1–3], the so-called quantum suppression of classical chaotic diffusion.

The current interest in coherent atomic dynamics in periodic potentials has been paralleled by burgeoning activity in the area of ratchet dynamics. However, most ratchet studies were motivated by interest in biophysical or mesoscopic systems and involved some form of Brownian motion combined with dissipation [4]. There was little work, in comparison, on Hamiltonian ratchets; the latter are of especial significance in cold atom physics since they alone can preserve quantum coherence over longer timescales.

Two exceptions are recent proposals for mixed-phase space ratchets [5, 6]. In [5], the spatio-temporal symmetries which must be broken to generate directed motion were considered. Directed motion was attributed to the de-symmetrization of Levy flights. In [6] a sum rule was obtained for the currents carried by different invariant manifolds in a mixed phase space. From this it was deduced that directed transport in a Hamiltonian system must originate from an inbalance between currents in stable regions (eg. islands) and currents in the chaotic regions. The fully averaged current for a uniform phase space density of a Hamiltonian system must be zero; this, one can argue, may exclude directed transport in a fully chaotic system [4, 6].

In [7] it was demonstrated that a type of, fully chaotic, Hamiltonian directed transport is possible. The proposed system involves broken spatio-temporal symmetries as stipulated in [5] and does not violate the sum rule since it is unbounded in momentum and therefore does not attain a uniform phase-space distribution. An implementation was proposed using cold atoms in double-well lattices pulsed with unequal periods. The characteristic of this system is an asymmetric diffusion in momentum: in other words, equal numbers of particles would diffuse right or left, say, but one direction would do so with larger momenta, hence generating a net current. Hence we term this a momentum-diffusion ratchet.

A key result of our previous work [7] was to show that there is a distinctive time-scale associated with this process: starting from an ensemble of particles with, initially, zero average momentum current $< p(t = 0) >$, we found the current grows with time. However,

eventually, a finite classical current was obtained, with a maximum value reached after a characteristic time-scale, the "*ratchet time*", t_r.

In this system, asymmetry in the momentum distribution accumulates until a finite non-zero value is reached at t_r. While the value of the current saturates to a constant value, the average kinetic energy of the classical ensemble grows without limit. Hence practical implementation of the classical version of the chaotic Hamiltonian ratchet is less interesting. However, for the corresponding quantum system, the phenomenon of Dynamical Localization "freezes in" this momentum asymmetry, ensuring that the current is not diluted by continual expansion of the momentum distribution. For the maximal quantum current, one must ensure that the quantum *break-time*, t^*, at which Dynamical Localization occurs, is approximately the same as the *ratchet time*, t_r, in order to suppress momentum diffusion at the point where the asymmetry is largest.

A related system, an optical lattice with a rocking linear potential, with a similar directed motion mechanism was later investigated by us in [8]. An experimental version of the latter was demonstrated using cesium atoms in an optical lattice [9]. The double-well ratchet presented here has not yet been investigated experimentally, but is in principle amenable to existing techniques in cold atom physics.

In [7], only a heuristic derivation of the timescale t_r was presented. While it was explained that the asymmetric diffusion originates in neglected corrections to the diffusion rate which are obtained when one considers correlations between short sequences of kicks, no expressions were presented. Here we provide formal derivations for t_r and the analytical form to the asymmetric diffusion rate. We also derive a closed analytical expression for the current itself and show that we can predict current reversals without resorting to a numerical study of the dynamics. These are the main new results in this paper.

We show below that the current-generating diffusive correlations of the double-well ratchet are significantly more complicated than for the rocking ratchet in [8]. For instance, we find that there are in fact several significant timescales corresponding to the different important correction terms. The observed saturation point corresponds simply to the longest one among these.

In Section II, we outline the basic features of the physical system. In Section III we derive corrections to the diffusion coefficient which give rise to momentum-dependent diffusion rates. We obtain an analytical form for the diffusion coefficient (Eq.3.9) that yields

close agreement with numerical simulations. We also investigate the timescales involved in the system, and derive the form for t_r (Eqs.3.12 - 3.13). In Section IV we obtain a closed formula for the momentum current (Eq.4.2) which yields good results and enables us to analyse features of the numerical results such as current reversals. Hence, Eqs. (3.9)-(3.11) and Eq.(4.2) represent the main new equations. In Section V we briefly review the quantum behaviour of this system and present a few additional results showing the competition between Dynamical Localization and the classical asymmetric diffusion process. Finally, in Section VI, we conclude.

II. THE CHAOTIC HAMILTONIAN RATCHET WITH PULSED DOUBLE-WELLS

The ratchet system introduced in [7] is based on a modified form of the well-studied Kicked Rotor system, where we have replaced the sinusoidal motion of the rotor with a double well potential:

$$V(x) = \sin x + a\sin(2x + \phi) \tag{2.1}$$

and introduced unequally spaced kicks, such that the Hamiltonian for the system becomes:

$$H = \frac{p^2}{2} + K(\sin x + a\sin(2x+\phi))\sum_{s=0}^{\infty}\sum_{M=1}^{ncyc}\delta\left(t - \left(sT_{tot} + \sum_{i=1}^{M} T_i\right)\right) \tag{2.2}$$

In effect, we have a kicked rotor (the QKR in the quantum case), with a spatially asymmetric potential, kicked with a repeating cycle of unequally spaced 'kicks'. The T_i are the time intervals between successive kicks, which form a cycle of length *ncyc*, with $T_{tot} = \sum_{i=1}^{ncyc} T_i$. This 'kicked ratchet' is associated with an effective kicking strength: $K_{eff} = K\sqrt{1+4a^2}$. In the lowest order of approximation, the energy of an ensemble of classical particles grows linearly with time as $< p^2/2 >= \frac{K_{eff}^2}{4}t$.

The introduction of unequally spaced kicks breaks the time reversal symmetry, which is necessary to generate a non-zero current in the system [7]. In this paper, we focus (as in [7]) on a cycle of three kicks such that the spacings are : $T_1 = (1+b)$, $T_2 = 1$ and $T_3 = (1-b)$, with b a small parameter.

For low values of the kicking strength K, the classical phase space demonstrates the momentum-asymmetry in the dynamics, with islands and tori having no partners at corre-

sponding negative momenta. A key feature of our system is that it works in the regime of global chaos and does not depend on the presence of regular structures in phase space. A typical Poincaré surface of section from the parameter space we have studied is shown in Fig. 1, showing the absence of visible islands or KAM tori.

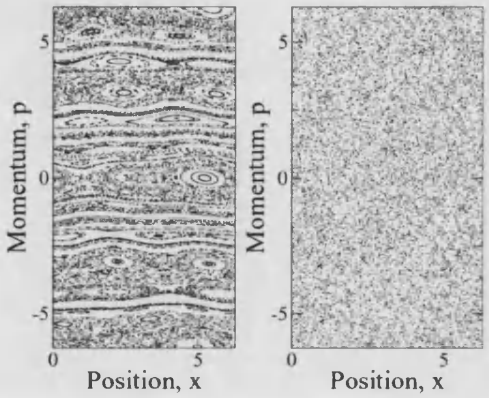

FIG. 1: Poincaré surfaces of section for the chaotic hamiltonian ratchet. (a) At low kicking strength ($K = 0.1$) the asymmetry in the system is already apparent. (b) At $K = 2$ the system is in the globally chaotic regime; note the absence of any islands/tori. It is in this regime that our numerical simulations are performed. Each plot was calculated by starting 400 initial trajectories evenly spaced over a range of x:[0,2π] and p:[-10,10] then kicking each trajectory 200 times.

The observed build-up, with time, of asymmetry in the momentum distribution is due to differing classical momentum diffusion rates for particles with positive momenta relative to those with negative momenta. For physical insight (and before we derive a more rigorous treatment of the diffusion process in the next section), we show in Fig. 2 the energy absorbed by an ensemble of particles for a typical set of parameters. At $t = 0$ all the particles had $p = 0$. We plot separately the total energy of the particles with negative momenta and those with positive momenta, as a function of time. The figure shows clearly that for $b = 0.05$, and time $t < 2000$ or so, particles with positive momenta absorb kinetic energy significantly more slowly than particles with negative momenta. But the average is close to the well known "quasi-linear" rate $< E >= D_{ql}t = \frac{K_{eff}^2}{4}t$, associated with a random-walk in momentum space. These rates appear to equalize after a certain time and to revert to $D \simeq D_{ql}$.

From Fig. 2 one can clearly see that the energy splitting is not only momentum-dependent,

but that the corresponding ratchet time is dependent on b,the perturbation to the kicking-period. In [7] we attributed the cause of these differing diffusion rates to correlations between short sequences of kicks in the evolution sequence, yielding corrections to overall diffusion rate. In effect, the diffusion rate for this system becomes local in momentum $D \equiv D(p,t)$. It is also not linear in time - as seen below, except for very short times and for very long times. In the next section we derive in detail these corrections, investigate the timescales involved and hence can analyse the general behaviour seen in Fig. 2.

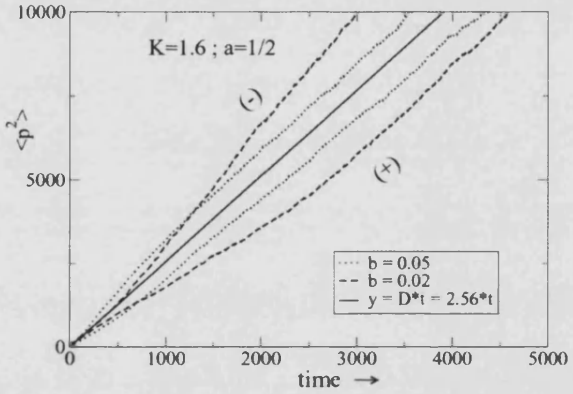

FIG. 2: Figure illustrates differential energy absorption for particles with positive and negative momenta. An ensemble of particles (all with $p = 0$ at initial time, $K = 1.6$, $a = 0.5$) is evolved, and $\langle p^2 \rangle$ is calculated separately, at each time, for particles with positive and negative momenta. The two upper curves (near the (-) sign) show $\langle p^2 \rangle$ as a function of time for particles with negative momentum and two different values of b, the two lower curves (near the (+) sign) show the corresponding curves for particles with positive momentum. We see that particles with negative momenta, for a certain time period absorb energy faster than those with negative momenta. Note also that the behaviour become linear after a certain time.

III. THE MOMENTUM DIFFUSION COEFFICIENT

At the lowest level of approximation in ratchet and rotor systems, the growth of the average energy, in the absence of phase space barriers, can be approximated by the quasi-linear formula: $D_{ql} \approx K^2/4$ [10]. However, this approximation neglects the effect of correlations

between consecutive kicks which can significantly modify the diffusion coefficient. In the case of the Standard Map (corresponding, in Eq. (2.2) to $a = 0, b = 0$), the energy growth for an ensemble of classical particles with initial momentum p_0 is given by:

$$\left\langle \frac{(p-p_0)^2}{2} \right\rangle = Dt \equiv D_0 t + t\sum_{l=1}^{\infty} C(l,p), \tag{3.1}$$

where the $C(l)$ terms are corrections to the quasi-linear diffusion resulting from correlations between successive kicks.

These corrections have been studied extensively for the Standard Map, resulting in an adjusted diffusion coefficient [10, 11]:

$$D = \frac{K^2}{4}\{1 - 2[J_1(K)]^2 - 2J_2(K)...\} \tag{3.2}$$

Here, for example, the $-J_2(K)$ term arises from the 2-kick correlation which has the form: $C(2,p) = \langle V'(x_i)V'(x_{i+2})\rangle$. Here x_i is the x coordinate after kick i and the average is carried out over all phase-space coordinates. One can clearly see that for the Standard Map, the diffusion coefficient is momentum-independent. As the results below show, in our case, the diffusion coefficient becomes momentum-dependent. The calculation, outlined below, is an extension of the method of Rechester and White [12], and is detailed in full in the appendix.

Starting with an initial momentum p_0, the diffusion coefficient can be written in terms of the conditional probability density Q that the system evolves to a state (x_N, p_N) at time $t = N$ (that is, after N kicks):

$$D(N) = \frac{1}{2N}\int Q(x_N, p_N, N|x, p, 0)P(x, p, 0)(p_N - p)^2 dx_N dp_N\, dx dp \tag{3.3}$$

where the initial probability distribution is given by:

$$P(x,p,0) = (2\pi)^{-1}\delta(p - p_0),$$

Using the recursion property of the conditional probability Q, and the 2π periodicity in the x variable, we can write the diffusion coefficient as (see appendix):

$$D = \lim_{N\to\infty}\frac{1}{2N}\sum_{m_N=-\infty}^{\infty}\cdots\sum_{m_1=-\infty}^{\infty}\prod_{i=0}^{N}\int_0^{2\pi}\frac{dx_i}{(2\pi)}S_N^2 \exp\left(\sum_{j=1}^{N}[im_j(x_j - x_{j-1} - (t_j - t_{j-1})(p_0 + S_{j-1}))]\right) \tag{3.4}$$

where we define:

$$S_j = -\sum_{l=0}^{j} V'(x_l). \tag{3.5}$$

By setting $m_j = 0$ for all j in the above formula, one simply recovers the quasi-linear diffusion. In order to examine the contribution of various correlations one must look at the product of terms where the m_j are set to an appropriate non-zero value.

The main corrections to the diffusion rate for the ratchet are found by considering the 2-kick correlations, $C(2,p)$, ie. choosing the term $2V'(x_i)V'(x_{i+2})$ in the product $S_N^2 = S_N S_N$. For small b, the leading contribution to this correction comes by taking $m_{i+2} = \pm 1$ and $m_{i+1} = -m_{i+2}$ (all other m_j zero; this gives the contribution of the $K \sin x$ part of the potential), or $m_{i+2} = \pm 2$ and $m_{i+1} = -m_{i+2}$ (contribution of the $\sin 2x$ part of the potential). Since there are three different time intervals possible between kicks i and $i+2$ ($T_1 + T_2$, or $T_2 + T_3$, or $T_3 + T_1$), one has to calculate three different contributions for these three cases. Summing the results for all kicks i between 1 and N, we get a contribution from the $\sin x$ part of the potential (the full derivation is contained in the appendix):

$$\begin{aligned} C_{\sin x}(2,p) = -\frac{K^2}{6}\Bigg[& \sum_{-\infty}^{\infty} J_{2-2s}(K(1+b))J_s(2Ka(1+b))\cos(2p_0 b + \frac{\pi}{2}s) \\ & + \sum_{-\infty}^{\infty} J_{2-2s}(K)J_s(2Ka)\cos(p_0 b - \frac{\pi}{2}s) \\ & + \sum_{-\infty}^{\infty} J_{2-2s}(K(1-b))J_s(2Ka(1-b))\cos(p_0 b - \frac{\pi}{2}s)\Bigg] \end{aligned} \tag{3.6}$$

The sum over s formally spans the range $s = \pm\infty$, but for typical K values converges for $|s| < 20$. This result is valid for short times. For longer times (that is, larger kick value N), the correction to the average energy growth is no longer linear in time, and eventually saturates to a given value. This is discussed later, together with the ratchet time.

The cosines in equation (3.6) can be expanded; for example the first term in Eq. (3.6) becomes:

$$C^{(1)}_{\sin x} = \frac{K^2}{6}\sum_s J_{2-2s}(K(1+b))J_s(2Ka(1+b))(\cos 2p_0 b \cos\frac{\pi}{2}s - \sin 2p_0 b \ \sin\frac{\pi}{2}s)$$

If we wish to consider only the build-up of asymmetry in the system about $p = 0$, we can neglect the even terms. The asymmetry which drives the directed transport is due solely to the $\sin np_0 b$ ($n = 1, 2, 4$) dependent terms in the diffusion coefficient (those which are odd

with respect to reflection about $p = 0$). We therefore simplify Eq. (3.6) to:

$$C_{\sin x}^{(asymm)}(2,p) = \frac{K^2}{6}\Bigg[\sum_s J_{2-2s}(K(1+b))J_s(2Ka(1+b))\sin 2p_0 b\ \sin\frac{\pi}{2}s - \sum_s J_{2-2s}(K)J_s(2Ka)\sin p_0 b\ \sin\frac{\pi}{2}s - \sum_s J_{2-2s}(K(1-b))J_s(2Ka(1-b))\ \sin p_0 b \sin\frac{\pi}{2}s\Bigg] \quad (3.7)$$

A similar equation is obtained for the $Ka\sin 2x$ part of the ratchet potential:

$$C_{\sin 2x}^{(asymm)}(2,p) = \frac{(2Ka)^2}{6}\Bigg[-\sum_s J_{4-2s}(2K(1+b))J_s(4Ka(1+b))\sin 4p_0 b\ \sin\frac{\pi}{2}s + \sum_s J_{4-2s}(2K)J_s(4Ka)\sin 2p_0 b\ \sin\frac{\pi}{2}s + \sum_s J_{4-2s}(2K(1-b))J_s(4Ka(1-b))\sin 2p_0 b\ \sin\frac{\pi}{2}s\Bigg] \quad (3.8)$$

These formulae can now be rearranged to give the total correction to the diffusion coefficient as a function of the three $\sin npb$ present (note that we use $s' = 2-2s$ and $s'' = 4-2s$ for clarity):

$$C^{(asymm)}(2,p) = -\frac{K^2}{6}\Bigg[\sin p_0 b\Bigg\{\sum_s [J_{s'}(K)J_s(2Ka)+J_{s'}(K(1-b))J_s(2Ka(1-b))]\ \sin\frac{\pi}{2}s\Bigg\} - \sin 2p_0 b\Bigg\{(2a)^2\sum_s [J_{s''}(2K)J_s(4Ka) + J_{s'}(K(1+b))J_s(2Ka(1+b))+ (2a)^2 J_{s''}(2K(1-b))J_s(4Ka(1-b))]\ \sin\frac{\pi}{2}s\Bigg\} + \sin 4p_0 b\Bigg\{(2a)^2\sum_s J_{s''}(2K(1+b))J_s(4Ka(1+b))\sin\frac{\pi}{2}s\Bigg\}\Bigg] \quad (3.9)$$

The form above does not incude the time dependence or information on the ratchet time scales. An analytical form for these time scales is obtained by taking the full time dependence into account in the calculations (see appendix). For each $\sin np_0 b$ term, there is a time-dependent function $\Phi(N, bK, n)$. We re-write Eq. 3.9 as a Fourier series, with the Bessel function products replaced by coefficients A_n.

$$C^{(asymm)}(2,p) = -\frac{K^2}{6}\Big[A_1\sin p_0 b - A_2\sin 2p_0 b + A_4\sin 4p_0 b\Big] \quad (3.10)$$

The Bessel sum can easily be evaluated: for example, for $K = 14, a = 1/2, b = 0.005$, we find $A_1 = 0.13$ so the $\sin p_0 b$ term is weighted by a coefficient $\frac{K^2}{6} A_1 = 4.3$, which will later be compared to numerical values.

To go beyond the form valid only at short times, we must weight each term by $\Phi(N, bK, n)$, where N is the number of kicks and $N = t$. Hence:

$$C^{(asymm)}(2,p) = -\frac{K^2}{6}\left[A_1\Phi(N,bK,1)\sin p_0 b - A_2\Phi(N,bK,2)\sin 2p_0 b + A_4\Phi(N,bK,4)\sin 4p_0 b\right] \tag{3.11}$$

The leading term is the time-behaviour function $\Phi(N, bK, 1)$, which can be shown to take the form (see appendix):

$$\Phi(N,bK,1) = \frac{3}{N}\frac{1-[J_0(bK)J_0(2abK)]^{N-1}}{1-[J_0(bK)J_0(2abK)]^3} \tag{3.12}$$

(to obtain the form for $\Phi(N, bK, 2)$ we would simply double the arguments of the Bessel functions above and for $\Phi(N, bK, 4)$ we would quadruple them).

For small b and small N, $\Phi(N, bK, n) \simeq 1$, which leads to the linear correction to the energy: in this regime we could write $< \frac{(p-p_0)^2}{2} > \simeq Dt \equiv D_0 t + C(2,p)t$ as in Eq.(3.1). We recall that $C(2,p) = C^{(asymm)}(2,p) + C^{(symm)}(2,p)$ and only the $C^{(asymm)}(2,p)$ term represents diffusion asymmetric about $p = 0$ and hence the ratchet effect.

However, for larger N, eventually $\Phi(N, bK) \sim 1/N$ so the contribution of the 2-kick correction, $C^{(asymm)}(2,p)\Phi(N,bK)\ t$, tends to saturate to a constant value. The saturation time for the leading term $\Phi(N, bK, 1)$ (which is the most long-lived) is the ratchet time.

The ratchet time can be estimated by finding the time at which $\Phi(N, bK, n = 1)\ t$ reaches 95% of its value at $N = \infty$. This is found to be, for $a = 1/2$:

$$t_r^{(\sin pb)} = \frac{2\ln(20)}{(Kb)^2} \approx \frac{6}{(Kb)^2} \tag{3.13}$$

The heuristic arguments in [7] gave a timescale $t_r \sim \frac{2\pi}{(Kb)^2}$ which is not too different. The same analysis can now be repeated to obtain the separate (shorter) time scales corresponding to the $\sin 2pb$, $\sin 4pb$ corrections. It is straightforward to show that $4t_r^{(\sin 2pb)} \simeq t_r^{(\sin pb)}$ and $16t_r^{(\sin 2pb)} \simeq t_r^{(\sin pb)}$.

Note that for large N, $\Phi(N)\ t$ saturates to the value of $\sim 1/[(bK)^2]$. The energy growth is no longer affected by the two-kick correlations and contains no asymmetric diffusion component. This results in a progressive dilution of the asymmetry in the classical case

(but not the quantum case). One also notes that the ratchet effect is clearly dominated by the time-scale corresponding to the $\sin pb$ term (the two other ratchet times are respectively 1/4 and 1/16 smaller).

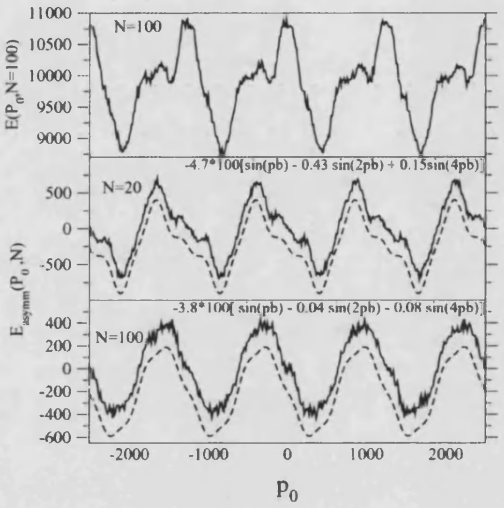

FIG. 3: (a) Average classical kinetic energy $E(p_0, N = 100)$ plotted as a function of initial momentum p_0, calculated numerically for an ensemble of 10^6 particles with $K = 14$, $a = 1/2$, b=0.005 time $t = 100$. In (b) and (c) we have removed the momentum-independent and symmetrical $\cos npb$ contributions by plotting $E_{asymm}(P_0, N) = \frac{1}{2}[E(p_0, N) - E(-p_0, N)]$. The energy spread after 20 kicks is shown in (b) and after 100 kicks in (c). The dashed curves, are obtained by Fourier analysis of the numerical results. For clarity, these curves have been shifted vertically.

Figure 3(a) plots $E(p_0, N = 100)$, the average kinetic energy of an ensemble of 10^6 particles which all had $p = p_0$ at $N = 0$, as a function of p_0. These numerics enable us to obtain numerical estimates of the coefficients $\frac{K^2}{6}A_n$. Now at short times, $E(p_0, N) \simeq D_0\ t + C(2,p)t$ and includes both the symmetric and asymmetric terms in the diffusion coefficient. In Figs. 3(b) and (c) we have removed the symmetric contribution (and $D_0\ t$) by plotting $E(N)_{asymm} = \frac{1}{2}[E(p_0, N) - E(-p_0, N)]$. Figure 3(b) shows $5E_{asymm}(p_0, N = 20)$, whereas Figure 3(c) shows $E_{asymm}(p_0, N = 100)$ (the $N = 20$ values were re-scaled for ease of comparison). We can now fit a Fourier series in $\sin p_0 b$ to each curve and obtain the relative amplitudes for each of the three terms that appear in our analytical formula (3.9);

$\sin p_0 b$, $\sin 2p_0 b$ and $\sin 4p_0 b$. One can clearly see that for the example given, the relative amplitudes of the terms vary with time: at 20 kicks there is a strong contribution from the $\sin 2pb$ term, whereas after 100 kicks the $\sin 2pb$ contribution is an order of magnitude smaller and the curve is almost a pure $\sin pb$. The $\sin pb$ weighting coefficients estimated from the graphs, 4.7 and 3.8 compare favourably with the estimate of Eq. 3.10, where we calculate $\frac{K^2}{6} A_1 = 4.3$.

Fig 4 shows the dependence of the amplitudes of each of the sine terms on kick strength, K, after 20, 40 and 100 kicks. Also shown is the analytical form for each term as predicted in Eq. (3.9). It can be clearly seen that the $\sin pb$ contribution persists beyond 100 kicks for all values of K. The $\sin 2pb$ contribution is still significant at 40 kicks for all values of K, but has been significantly damped by 100 kicks for $K > 10$. The timescale over which the $\sin 4pb$ contribution is appreciable is shorter still. For $K > 6$ the amplitude at 100 kicks is virtually negligible whilst at 20 and 40 kicks it is heavily damped.

In Fig. 5 the ratchet time is plotted against the parameters b and K. Each point on the graph corresponds to a measurement of t_r for a given parameter set. The value of t_r was estimated by taking a running average over 50 kicks and measuring the standard deviation in $< p >$ of the ensemble of 400,000 trajectories. When the deviation fell to below 5 percent of the maximum the value of t_r was assigned. In Fig 5(a) the value of b is varied across a wide range while the kicking strength K is kept constant. The plot shows clear numerical evidence of the $1/b^2$ proportionality of the ratchet time. A fit of $t_r = 2\pi/(Kb)^2$ is plotted against the numerical results and very good agreement can be seen. In the lower panel (Fig. 5(b)) the parameters are exchanged and K^2 is varied against a constant b. Once again the numerical results bear out an excellent correspondence to the expected $t_r \simeq 6/(Kb)^2$ relationship obtained from the $\sin pb$ term above.

IV. THE RATCHET CURRENT

It is possible to obtain an analytical form for the classical ratchet current shown in Fig 7, using a very similar method to that used to obtain the diffusion coefficient. In this case we define the average current at a given time to be:

$$\langle p(N) \rangle = \int Q(x_N, p_N, N | x_0, p_0, 0) P(x_0, p_0, 0)(p_N - p_0) dx_N dp_N. \qquad (4.1)$$

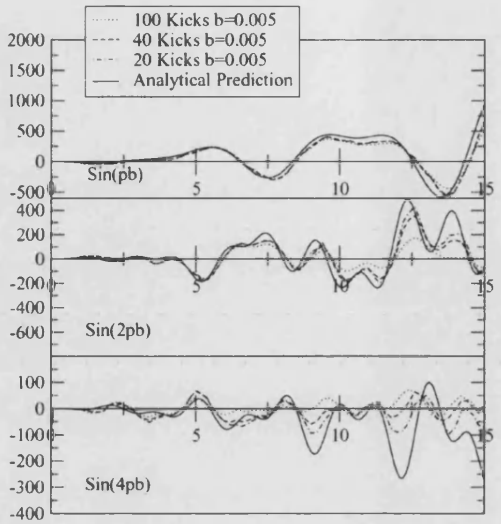

FIG. 4: Contributions to classical asymmetric energy diffusion that arise from $\sin(npb)$ terms in the 1st order correction to the diffusion constant are shown as a function of K. Analytical predictions are compared with numerical results for varying numbers of kicks (all scaled to 100 kicks) to highlight the time scales involved. One can see in (a) that the numerical results for the $\sin(pb)$ term show excellent agreement with the analytical prediction for all K, suggesting that this term continues to influence the final current past 100 kicks. In (b) one sees good agreement for both 20 kicks and 40 kicks up to fairly high K, whereas after approximately K=10 the 100 kick curve begins to depart markedly from the analytical prediction. This suggests that for high kick strength the contribution to the final current from the $\sin(2pb)$ term has been damped by 100 kicks. This effect is even more noticeable for $\sin(4pb)$ as shown in figure (c). Good agreement between numerics and analytics exists only up to approximately K=5 with the 100 kick curve becoming heavily damped soon after. One can clearly see the 40 kick curve departing from the analytical result more quickly and completely than the 20 kick result. These plots show that for increasing kick strength, the time scale over which each term contributes to the final current changes.

It is easily shown that, like the asymmetric energy diffusion, the momentum current increases with N and then saturates after a time scale $t_r \sim 1/(Kb)^2$. This is unsurprising, since the two share a common physical origin.

We evaluate the saturated current, $\langle p(N \to \infty) \rangle$. The leading order term for the average

saturated current obtained using the modified Rechester and White approach is then:

$$\langle p(N \to \infty) \rangle = K \frac{J_1(bK)J_0(2abK)}{1-(J_0(bK)J_0(2abK))^3} \sum_s \sin(p_0 b - \frac{\pi}{2}s) J_{2-2s}(K) J_s(2aK)$$
$$-2Ka \frac{J_0(2bK)J_1(4abK)}{1-(J_0(2bK)J_0(4abK))^3} \sum_s \sin(p_0 b - \frac{\pi}{2}s) J_{4-2s}(2K) J_s(4aK), \tag{4.2}$$

where the approximation $1 - b \approx 1$ has been made. The first term in equation (4.2) arises from the $K \sin x$ part of the potential, and the second term is the contribution from $Ka \sin 2x$.

We note that the momentum current tends to a constant value as $t \to \infty$. However the width of the momentum distribution continues to grow as $D_0 t$. Hence the momentum current, normalised to the width of the momentum distribution, will tend to zero in the classical case, but - as discussed in the next section- will tend to a constant in the quantum case.

The top panel of Figure 6 shows a comparison of this result with numerical simulation for

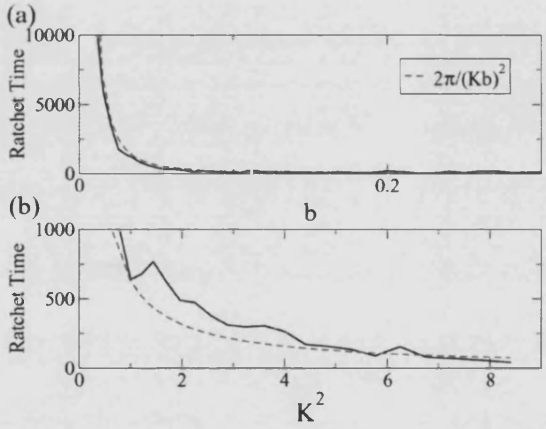

FIG. 5: Classical ratchet saturation time, measured in kicks, versus system parameters b (a) and K^2(b). (a) the classical ratchet time is measured when the deviation of a 100 kick running average fall below 2 percent of its maximum value. A very good numerical agreement (solid line) is shown to a fit of $2\pi/K^2b^2$ (dashed line). The value of K was fixed at 1.6. (b) using the same measurement technique for (a) the ratchet time is plotted against K^2 for a fixed $b = 0.1$. Again a non-linear curve fit of $2\pi/K^2b^2$, (dashed line) is compared to the numerical results (solid line). Each point on each graph is a result of a classical calculation of 500,000 trajectories run over 10,000 kicks.

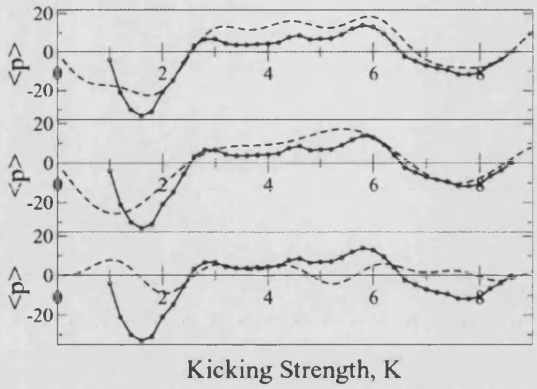

FIG. 6: Comparison of numerical and analytical average current as a function of kicking strength, K. In (a) the leading order analytical term (dashed line) given by equation (4.2) is shown with the numerical result (circles) for $b = 0.01$ and $a = 1/2$. Note that the current reversals are accurately predicted, as is the general trend of the numerical curve. Panel (b) shows the contribution from the 1st term in equation (4.2), due to the $\sin x$ part of the potential. The final panel (c) shows the contribution from the second term, due to $\sin 2x$. Both curves are plotted with the numerical result.

$b = 0.01$, $a = 0.5$ and zero initial momentum. The individual contributions from each term in Eq. (4.2) are shown in the lower two panels of the figure. The shape of the curve is clearly dominated by the $K \sin x$ part of the potential, but one can easily see where the $Ka \sin 2x$ part competes - for example, to create the dips between $K = 3 \rightarrow 6$. Whilst the current reversals are accurately predicted and the general trend of the curve is in keeping with the numerical results, there are some features which are not in keeping with expectation. In the region $0 \leq K \leq 2$ the numerical current appears to decrease much more rapidly than the analytical prediction. This is possibly due to the increasing regularity of the system inhibiting the build up of asymmetry. Once beyond the current reversal at $K = 2.6$, the magnitude of the current never reaches that of the analytical curve. In this region the ratchet time is short, and the asymmetry in the system is washed out by the expansion of the classical momentum distribution. Also, Eq. (4.2) is the leading order term for the current, resulting from the second order correlations. One would expect that including higher order terms might well affect the predicted current, and improve the accuracy of the

result. Furthermore, the analytical form is valid in the regime of small b, and one would anticipate that the numerical curve will tend to the theoretical prediction as $b \to 0$.

V. COMPETITION BETWEEN t_r AND t^*

Having considered exclusively the *classical* diffusion mechanism underpinning this ratchet in the previous sections, we must now examine the corresponding *quantum* behaviour. The implementation of this type of ratchet is best done using cold atoms in optical lattices, a system far from the classical limit. Here we review in brief the quantum results obtained in [7] and extend those calculations to test a wider parameter range.

In the quantum case, in addition to the dynamical parameters K, a, b we must consider $\hbar$ (note that in the experiment, a rescaling of coordinates introduces an effective value of $\hbar$. In a typical experiment $\hbar \sim 0.25 - 2$). A conclusion of [7] was that the key to achieving the most distinctive experimental asymmetry lies in approximately equalizing the two time scales of the system: the classical ratchet time, t_r and the quantum break-time t^*. We recall that for the standard Quantum Kicked Rotor (QKR), $t^* \sim \frac{D}{\hbar^2}$. In our case we still have a time-periodic system (though with a time-period in effect three times longer than the QKR) so its time evolution can be determined by an expansion over the underlying Floquet states: in the long-time limit its behaviour is quasi-periodic and diffusion is suppressed as in the QKR.

A numerical study in [7] found that Dynamical Localization proceeds in a similar way to the QKR. For each particular set of dynamical parameters K, a, b and $\hbar$, the time evolution of a minimal uncertainty wavepacket was calculated in a plane-wave basis. A quantum probability distribution for the momentum $N(p,t)$ was obtained as a function of time. From this it is simple to compute the expectation values of the momentum $< p >$, the energy $< p^2 >$ as well as the saturation time for the energy, t^*. In our system, unlike the QKR, we have a local (in momentum) diffusion rate $D(p)$ which oscillates with momentum (with period $2\pi/b$, see Fig.3) about the uncorrelated value $D_0 = K_{eff}^2/4$. For the parameters considered here, the amplitude of these oscillations is not large compared with D_0. In that case, we found from numerics in [7] that the break time corresponds closely to the averaged value $t^* \sim 20\frac{D_0}{\hbar^2}$ [13].

It is interesting to contrast this with the rocking lattice system and experiment in [8,

9] which corresponded to the opposite limit: if the amplitude oscillations in the 2-kick correlations are large relative to the uncorrelated rate D_0, and $b \sim 0.01$ is small, the typical width of $N(p)$ is small relative to $2\pi/b$. For a narrow momentum distribution $N(p_0 - p)$, strongly peaked about a momentum $p = p_0$, one needs to consider a local break-time $t(p_0)^* \sim \frac{D(p_0)}{\hbar^2}$ which can vary by a factor of ~ 100 as one varies the initial drift momentum p_0 of the atoms relative to the optical lattice [8]. However, this is not the situation here. For this system we find that $t^* \simeq 20\frac{K_{eff}^2}{\hbar^2}$ represents a good approximation, for all values of b.

If the quantum diffusion persists as long as t_r, the quantum system acquires the full classical asymmetry. Hence the condition $t^* \sim t_r$ ensures that the maximal classical asymmetry is frozen in and that the asymmetry is not diluted by the continual spread of the classical momentum distribution. Evidence for this criterion is shown in Fig 7, where the classical and quantum currents (after saturation) are shown for various parameter choices. For the quantum case, $\hbar$ is decreased from $\hbar = \frac{1}{2}$ to $\hbar = \frac{1}{8}$ whilst keeping b, the perturbation to the period, constant at $b = 0.1$. For the lower values of the kicking strength, $K \sim 2.5$ or less, one can see that the quantum current approaches the classical current for $b = 0.1$ as $\hbar$ is decreased. Recalling that $t^* \propto 1/\hbar^2$ we see the effect of the changing break-times: in the range $K = 2 - 2.5$ all the curves ($\hbar = 1/2, 1/4, 1/8$ and classical) are roughly in agreement. In this range all values of $\hbar$ allow time for asymmetry to accumulate. However, for $K = 1.5 - 2$, for $\hbar = 1/2$ and $1/4$, in this range, $t^* < t_r$ so the quantum current falls below the classical value. The quantum momentum distribution localises before the full asymmetry is achieved. However, $\hbar = 1/8$ follows quite closely the classical behaviour in this range since it has a break time 16 times longer than for $\hbar = 1/2$.

As the kick strength is increased beyond the crossing (approx. $K \approx 2.6$) one notes that there is once again a large discrepancy between the classical and quantum results. The ratchet time decreases with increasing K (as shown by the scaled t_r curve shown in the figure), and when the ratchet time is too short, the calculated classical asymmetry is negligible. Perhaps surprisingly though, the corresponding quantum system still exhibits significant asymmetry. In fact the quantum behaviour corresponds more closely to the classical current for somewhat smaller values of $b < 0.1$: when t_r is very small we get poor agreement between classical and quantal results, even with small $\hbar$. It is clear that some details of the quantum classical correspondence here will only be understood from a detailed study of the properties of the Floquet states of this quantum system, which is

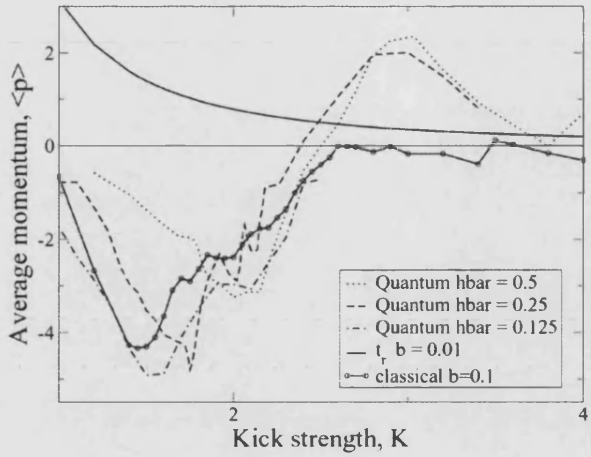

FIG. 7: Variation of average classical and quantum currents as a function of kick strength K. In the quantum case, where $b = 0.1$ for each curve, one notes that there is an improving fit with the classical $b = 0.1$ curve for decreasing $\hbar$. At low K the break-time for $\hbar = 0.5, 0.25$ is too short, and the system localises before the maximum amount of classical asymmetry has been reached. As K is increased, t^* increases and the classical and quantum plots show good agreement once $t^* \approx t_r$. Whilst both the quantum and classical curves share the same crossing, the classical curve for $b = 0.1$ does not show the positive peak that features in both quantum graphs. This is due to the fact that the ratchet time is now too short to allow any appreciable build-up of classical asymmetry (shown by the scaled ratchet time curve). The classical peak is recovered at smaller b (not shown), and therefore increasing t_r for a given value of K.

currently underway.

By decreasing the parameter b (and therefore increasing t_r) the classical current for high K once again approaches the quantum current. In broad terms however, we conclude that while the basic ratchet mechanism is a classical one, the best experimental results will be obtained with $t^* \sim t_r$. The best quantum-classical agreement will be obtained in the parameter ranges where neither t^* nor t_r are too small.

VI. CONCLUSION

We have derived analytical expressions for the energy diffusion rates, the classical ratchet currents and the ratchet time. We have shown that we can fully characterise the behaviour

of the only chaotic Hamiltonian ratchet mechanism proposed to date. This new type of Hamiltonian ratchet is in fact a momentum-diffusion ratchet. The current is generated by differential acquisition of kinetic energy by particles moving right or left, rather than an asymmetry in the global numbers of particles moving right or left. Finally we have have analysed the corresponding quantum behaviour. We have demonstrated the importance of an appropriate choice of ratchet time and quantum break-time in obtaining the best experimental momentum asymmetries.

APPENDIX A: DERIVATION OF CORRECTION TERMS

In order to obtain the Diffusion Coefficient for the ratchet we begin by defining the generalized map:

$$x_{j+1} = x_j + p_{j+1}(t_{j+1} - t_j) \tag{A1}$$

$$p_{j+1} = p_j - V'(x_j) \tag{A2}$$

where $t_{j+1} - t_j$ is the time between successive kicks $j+1$ and j. For the Standard Map, these intervals are the same for all kicks. However, this is not true for our chirped sequence. As explained in the text, we consider explicitly a cycle of three different intervals : $(1+b)$, 1 and $(1-b)$, with b a small parameter. From the map we have:

$$\begin{aligned} p_N &= p_0 - V'(x_0) - V'(x_1) \ldots - V'(x_{N-1}) \\ &= p_0 - \sum_{l=0}^{N-1} V'(x_l) \end{aligned}$$

and so we define:

$$S_j = -\sum_{l=0}^{j} V'(x_l) \tag{A3}$$

We use the standard definition of the diffusion coefficient:

$$\left\langle \frac{(p-p_0)^2}{2} \right\rangle = D(t)t, \tag{A4}$$

and assume that the systems starts at $p = p_0$ at time $t = 0$.

If we consider the diffusion in terms of the conditional probability density Q that the system evolves from the state $(x \in [0, 2\pi], p = p_0)$ at time $t = 0$ to the state $(x = x_N, p = p_N)$

at time $t = t_N$ we find:

$$D(t_N) = \frac{1}{2t_N} \int Q(x_N, p_N, t_N | x, p, 0) P(x, p, 0)(p_N - p)^2 dx_N dp_N dx dp \qquad \text{(A5)}$$

where the initial probability distribution is given to be:

$$P(x, p, 0) = (2\pi)^{-1} \delta(p - p_0),$$

Q obeys the recursion property:

$$Q(x_N, p_N, t_N | x_0, p_0, 0) = \int Q(x_N, p_N, t_N | x_i, p_i, t_i) Q(x_i, p_i, t_i | x_0, p_0, 0) dx_i dp_i \qquad \text{(A6)}$$

Inserting this property successively for each kick between N and 0 in equation (A6), and using:

$$Q(x_N, p_N, t_N | x_{N-1}, p_{N-1}, t_{N-1}) = \sum_{n_N=-\infty}^{+\infty} \delta(p_N - p_{N-1} + KV'(x_{N-1})) \\ \delta(x_N - x_{N-1} - (t_N - t_{N-1})(p_{N-1} - KV'(x_{N-1})) + 2\pi n_N) \qquad \text{(A7)}$$

where the sum over n_N occurs because of the periodic boundary condition for x_N ($0 \leq x_N \leq 2\pi$), we obtain:

$$Q(x_N, p_N, t_N | x_0, p_0, 0) = \sum_{n_N=-\infty}^{+\infty} \cdots \sum_{n_1=-\infty}^{+\infty} \int_0^{2\pi} \frac{dx_0}{2\pi} \delta(p - p_0) \int_0^{2\pi} dx_1 \ldots \int_0^{2\pi} dx_{N-1} \delta(p_N - p_0 - S_{N-1}) \\ \delta(x_N - x_{N-1} - (t_N - t_N - 1)((p_{N-1} - KV'(x_{N-1})) + 2\pi n_N) \ldots \\ \delta(p_1 - p_0 - S_0) \delta(x_1 - x_0 - (t_1 - t_0)(p_1 - KV'(x_0)) + 2\pi n_1) \qquad \text{(A8)}$$

Inserting the above equation into (A5) and taking into account the δ-function restraint on p_N, we find:

$$D = \frac{1}{2N} \sum_{n_N=-\infty}^{+\infty} \cdots \sum_{n_1=-\infty}^{+\infty} \prod_{i=0}^{N} \int_0^{2\pi} \frac{dx_i}{2\pi} S_N^2 \delta(x_N - x_{N-1} - (t_N - t_N - 1)(p_0 + S_{N-1}) + 2\pi n_N) \\ \ldots \delta(x_1 - x_0 - (t_1 - t_0)(p_0 + S_0) + 2\pi n_1) \qquad \text{(A9)}$$

By making use of the Poisson Summation formula:

$$\sum_{n=-\infty}^{+\infty} \delta(y + 2\pi n) = \frac{1}{2\pi} \sum_{m=-\infty}^{+\infty} \exp[imy] \qquad \text{(A10)}$$

we can write equation (A9) as:

$$D = \frac{1}{2N} \sum_{m_N=-\infty}^{\infty} \cdots \sum_{m_1=-\infty}^{\infty} \prod_{i=0}^{N} \int_0^{2\pi} \frac{dx_i}{(2\pi)} S_N^2 \exp\left(\sum_{j=1}^{N} [im_j(x_j - x_{j-1} - (t_j - t_{j-1})(p_0 + S_{j-1}))] \right) \tag{A11}$$

The term where $m_j = 0$ for all j corresponds to the quasi-linear diffusion:

$$\begin{aligned} D &= \frac{1}{2N} \prod_{i=0}^{N} \int_0^{2\pi} \frac{dx_i}{(2\pi)} S_N^2 \\ &= \frac{1}{2N} \prod_{i=0}^{N} \int_0^{2\pi} \frac{dx_i}{(2\pi)} K^2[-V'(x_0) - V'(x_1) - \ldots V'(x_{N-1})]^2 \\ &= \frac{1}{2N} K_{eff}^2 \frac{N}{2} \\ &= \frac{K_{eff}^2}{4} \end{aligned} \tag{A12}$$

where we recall that $K_{eff} = K\sqrt{1+4a^2}$.

All the other terms, where some of the m_j are non-zero, give corrections to this result. As noted in the text, the main corrections to the diffusion coefficient for the ratchet arise from correlations of the form $C(2,p) = \langle 2V'(x_j)V'(x_{j+2})\rangle$, obtained from equation (A11) by evaluating the contribution of $2V'(x_j)V'(x_{j+2})$ in the term S_N^2. The leading part of this contribution is obtained by setting $m_{j+2} = \pm 1$ and $m_{j+1} = -m_{j+2}$ (all other m are zero) for the $K \sin x$ part of the potential $V(x)$, and $m_{j+2} = \pm 2$ and $m_{j+1} = -m_{j+2}$ (all other m are zero) for the $Ka \sin 2x$ part of the potential $V(x)$ [12]. These corrections have to be summed over all kicks $j = 1 \ldots N$. Since there are three different time intervals between kicks ($T_1 = 1 + b$, $T_2 = 1$, $T_3 = 1 - b$), there are three different contributions to calculate. We now address individually each of these three contributions.

1. Correlation between kicks i, $i+2$

We choose the following map for this section:

$$\begin{aligned} x_i &= x_{i-1} + p_i(1+b) \\ x_{i+1} &= x_i + p_{i+1} \\ x_{i+2} &= x_{i+1} + p_{i+2}(1-b) \end{aligned} \tag{A13}$$

$$
\begin{aligned}
p_i &= x_{i-1} - V'(x_{i-1}) \\
p_{i+1} &= x_i - V'(x_i) \\
p_{i+2} &= x_{i+1} - V'(x_{i+1})
\end{aligned} \tag{A14}
$$

We consider first the correction that arises as a result of the $K \sin x$ part of the potential. Setting $m_{i+2} = -1$ and $m_{i+1} = +1$ in (A11), and keeping the $2V'(x_{i+2})V'(x_i)$ term of S_N^2 we obtain

$$
\begin{aligned}
C(2,p)^{i:i+2}_{m_{i+2}=-1} &= \frac{1}{2N}\prod_{j=0}^{N}\int_0^{2\pi}\frac{dx_j}{2\pi}2V'(x_{i+2})V'(x_i)\mathrm{e}^{-i(x_{i+2}-x_{i+1}-(1-b)(p_0+S_{i+1}))}\mathrm{e}^{+i(x_{i+1}-x_i-p_0-S_i)} \\
&= \frac{1}{N}\prod_{j=0}^{N}\int_0^{2\pi}\frac{dx_j}{2\pi}V'(x_{i+2})V'(x_i)\mathrm{e}^{-i(x_{i+2}-2x_{i+1}+x_i)}\mathrm{e}^{-ip_0b}\mathrm{e}^{i((1-b)S_{i+1}-S_i)}
\end{aligned} \tag{A15}
$$

Now we use the fact that:

$$
S_{i+1}(1-b) + S_i = -(1-b)V'(x_{i+1}) - bS_i \tag{A16}
$$

Therefore the correction becomes:

$$
C(2,p)^{i:i+2}_{m_{i+2}=-1} = \frac{1}{N}\prod_{j=0}^{N}\int_0^{2\pi}\frac{dx_j}{2\pi}V'(x_{i+2})V'(x_i)\mathrm{e}^{-i(x_{i+2}-2x_{i+1}+x_i)}\mathrm{e}^{-ip_0b}\mathrm{e}^{i(-(1-b)V'(x_{i+1})-bS_i)} \tag{A17}
$$

One can further simplify this equation by using the identity ($J_n(x)$ is the standard Bessel function):

$$
\exp[\pm iz\cos\theta] = \sum_n i^{\pm n}J_n(z)\exp[\pm in\theta], \tag{A18}
$$

to obtain:

$$
\begin{aligned}
C(2,p)^{i:i+2}_{m_{i+2}=-1} &= \frac{1}{N}\prod_{j=0}^{N}\int_0^{2\pi}\frac{dx_j}{2\pi}V'(x_{i+2})V'(x_i)\mathrm{e}^{-i(x_{i+2}-2x_{i+1}+x_i)}\mathrm{e}^{-ip_0b} \\
&\qquad \mathrm{e}^{-i((1-b)[K\cos(x_{i+1})+2Ka\cos(2x_{i+1})]+bS_i)} \\
&= \frac{1}{N}\int_0^{2\pi}\frac{dx_j}{2\pi}V'(x_{i+2})V'(x_i)\mathrm{e}^{-i(x_{i+2}-2x_{i+1}+x_i)}\mathrm{e}^{-ip_0b}\sum_n i^{-n}J_n((1-b)K)\mathrm{e}^{-inx_{i+1}} \\
&\qquad \sum_s i^{-s}J_s((1-b)2Ka)\mathrm{e}^{-i2sx_{i+1}}\mathrm{e}^{-ibS_i}
\end{aligned} \tag{A19}
$$

The integration over x_{i+1} gives

$$
\begin{aligned}
-nx_{i+1} - 2sx_{i+1} + 2x_{i+1} &= 0 \\
\Rightarrow n &= 2 - 2s
\end{aligned}
$$

So, we finally obtain:

$$C(2,p)^{i:i+2}_{m_{i+2}=-1} = \frac{1}{N}\prod_j \int_0^{2\pi} \frac{dx_j}{2\pi} V'(x_{i+2})V'(x_i)\mathrm{e}^{-i(x_{i+2}+x_i)}\mathrm{e}^{-ip_0 b} \sum_s i^{-2+s} J_{2-2s}((1-b)K)J_s((1-b)2Ka)\mathrm{e}^{-ibS_i} \quad \text{(A20)}$$

The integrations over x_j with $j > i+2$ give simply 1. The integrations over x_j with $j < i$ are all identical. They give a contribution:

$$(J_0(Kb)J_0(Kb2a))^i \quad \text{(A21)}$$

Since $Kb \ll 1$, $J_0(Kb) \simeq 1$, and one can neglect this term for short times (when the exponent i is not too large). We show however at the end of the appendix that the longer time behavior (and so the ratchet time) can be obtained from this term. Finally, we are left with the integration over x_{i+2} and x_i. For the x_i part, it is easy to show that the term $\exp(-ibS_i)$ can be neglected for small b. The exponentials $\exp(-ix_{i+2} - ix_i)$ must be combined with the product $V'(x_{i+2})V'(x_i)$ to give a non-zero result. We expand the product in the following way:

$$\begin{aligned} V'(x_{i+2})V'(x_i) &\equiv (K\cos x_{i+2} + 2Ka\cos 2x_{i+2})(K\cos x_i + 2Ka\cos 2x_i) \\ &= K^2\cos x_{i+2}\cos x_i + 2K^2 a\cos x_{i+2}\cos 2x_i \\ &\quad +2K^2 a\cos 2x_{i+2}\cos x_i + 4(Ka)^2\cos 2x_{i+2}\cos 2x_i \end{aligned} \quad \text{(A22)}$$

The first term, which arises from the $K\sin x$ part of the potential, is here the appropriate one to use:

$$K^2\cos x_{i+2}\cos x_i = \frac{K^2}{4}\left\{\mathrm{e}^{i(x_{i+2}-x_i)} + \mathrm{e}^{-i(x_{i+2}-x_i)} + \mathrm{e}^{i(x_{i+2}+x_i)} + \mathrm{e}^{-i(x_{i+2}+x_i)}\right\} \quad \text{(A23)}$$

The integrations are now trivial, and we get :

$$C(2,p)^{i:i+2}_{m_{i+2}=-1} = \frac{K^2}{4N}\mathrm{e}^{-ip_0 b}\sum_s i^{-2+s} J_{2-2s}((1-b)K)J_s((1-b)2Ka) \quad \text{(A24)}$$

The same calculation for the case: $m_{i+2} = 1$, $m_{i+1} = -1$ simply gives the complex conjugate of this expression.

Combining these results, we get :

$$C(2,p)^{i:i+2}_{K\sin x} = \frac{K^2}{4N}\sum_s J_{2-2s}((1-b)K)J_s((1-b)2Ka)\{i^{-2+s}e^{-ip_0b} + i^{2-s}e^{ip_0b}\}$$
$$= -\frac{1}{2N}\sum_s J_{2-2s}((1-b)K)J_s((1-b)2Ka)\cos(p_0b - \frac{\pi}{2}s) \quad \text{(A25)}$$

Since we have $N/3$ terms of this kind (only for $1/3$ of the N kicks do we have the map chosen in this section, eq. (A13) and (A14)), we obtain the final form of the $i{:}i+2$ correction to the quasi-linear diffusion resulting from the $K\sin x$ part of the potential as:

$$C(2,p)^{i:i+2}_{K\sin x} = -\frac{K^2}{6}\sum_s J_{2-2s}((1-b)K)J_s((1-b)2Ka)(\cos p_0b\cos\frac{\pi}{2}s + \sin p_0b\sin\frac{\pi}{2}s) \quad \text{(A26)}$$

Taking now $m_{i+2} = \pm 2$ and $m_{i+1} = -m_{i+2}$ and following the same analysis we pick out the correction to the diffusion coefficient due to the $Ka\sin 2x$ part of the potential, which is:

$$C(2,p)^{i:i+2}_{Ka\sin 2x} = \frac{(2Ka)^2}{6}\sum_s J_{4-2s}(2(1-b)K)J_s(4(1-b)Ka)(\cos 2p_0b\cos\frac{\pi}{2}s + \sin 2p_0b\sin\frac{\pi}{2}s) \quad \text{(A27)}$$

2. Correlation between kicks $i+1$, $i+3$

The analysis for the correlation between kicks $i+1$ and $i+3$ of our cycle follows the same pattern as that given above, starting from the following 3-kick map:

$$x_{i+1} = x_i + p_{i+1} \quad \text{(A28)}$$
$$x_{i+2} = x_{i+1} + p_{i+2}(1-b) \quad \text{(A29)}$$
$$x_{i+3} = x_{i+2} + p_{i+3}(1+b) \quad \text{(A30)}$$

$$p_{i+1} = x_i - V'(x_i) \quad \text{(A31)}$$
$$p_{i+2} = x_{i+1} - V'(x_{i+1}) \quad \text{(A32)}$$
$$p_{i+3} = x_{i+2} - V'(x_{i+2}) \quad \text{(A33)}$$

One therefore obtains the diffusion correction due to $K\sin x$ for kicks $i+1 : i+3$ to be:

$$C(2,p)^{i+1:i+3}_{K\sin x} = -\frac{K^2}{6}\sum_s J_{2-2s}((1+b)K)J_s((1+b)2Ka)(\cos 2p_0b\cos\frac{\pi}{2}s - \sin 2p_0b\sin\frac{\pi}{2}s) \quad \text{(A34)}$$

with the $Ka\sin 2x$ correction being:

$$C(2,p)^{i+1:i+3}_{Ka\sin 2x} = \frac{(2Ka)^2}{6}\sum_s J_{4-2s}(2(1+b)K)J_s(4(1+b)Ka)(\cos 4p_0 b\cos\frac{\pi}{2}s - \sin 4p_0 b\sin\frac{\pi}{2}s) \tag{A35}$$

Note that in this case we obtain correction terms that are dependent on $\sin 2pb$ and $\sin 4pb$, rather than $\sin pb$ and $\sin 2pb$ obtained from the $i:i+2$ correlation.

3. Correlation between kicks $i+2$, $i+4$

Once again, we begin by defining the map:

$$x_{i+2} = x_{i+1} + p_{i+2}(1-b) \tag{A36}$$

$$x_{i+3} = x_{i+2} + p_{i+3}(1+b) \tag{A37}$$

$$x_{i+4} = x_{i+3} + p_{i+4} \tag{A38}$$

$$p_{i+2} = x_{i+1} - V'(x_{i+1}) \tag{A39}$$

$$p_{i+3} = x_{i+2} - V'(x_{i+2}) \tag{A40}$$

$$p_{i+4} = x_{i+3} - V'(x_{i+3}), \tag{A41}$$

The analysis then follows precisely the same procedure given above, resulting in the $K\sin x$ correction:

$$C(2,p)^{i+2:i+4}_{K\sin x} = -\frac{K^2}{6}\sum_s J_{2-2s}(K)J_s(2Ka)(\cos p_0 b\cos\frac{\pi}{2}s + \sin p_0 b\sin\frac{\pi}{2}s), \tag{A42}$$

and the $Ka\sin 2x$ correction:

$$C(2,p)^{i+2:i+4}_{Ka\sin 2x} = \frac{(2Ka)^2}{6}\sum_s J_{4-2s}(2K)J_s(4Ka)(\cos 2p_0 b\cos\frac{\pi}{2}s + \sin 2p_0 b\sin\frac{\pi}{2}s) \tag{A43}$$

4. Total correction from the two-kick correlation

Combining these contributions together one obtains:

$$
\begin{aligned}
C(2,p) = \frac{1}{6}\Big(& K^2 \sum_s J_{2-2s}((1-b)K) J_s((1-b)2Ka)(\cos p_0 b \cos\tfrac{\pi}{2}s + \sin p_0 b \sin\tfrac{\pi}{2}s) \\
& +(2Ka)^2 \sum_s J_{4-2s}(2(1-b)K) J_s(4(1-b)Ka)(\cos 2p_0 b \cos\tfrac{\pi}{2}s + \sin 2p_0 b \sin\tfrac{\pi}{2}s) \\
& -K^2 \sum_s J_{2-2s}((1+b)K) J_s((1+b)2Ka)(\cos 2p_0 b \cos\tfrac{\pi}{2}s - \sin 2p_0 b \sin\tfrac{\pi}{2}s) \\
& +(2Ka)^2 \sum_s J_{4-2s}(2(1+b)K) J_s(4(1+b)Ka)(\cos 4p_0 b \cos\tfrac{\pi}{2}s - \sin 4p_0 b \sin\tfrac{\pi}{2}s) \\
& -K^2 \sum_s J_{2-2s}(K) J_s(2Ka)(\cos p_0 b \cos\tfrac{\pi}{2}s + \sin p_0 b \sin\tfrac{\pi}{2}s) \\
& +(2Ka)^2 \sum_s J_{4-2s}(2K) J_s(4Ka)(\cos 2p_0 b \cos\tfrac{\pi}{2}s + \sin 2p_0 b \sin\tfrac{\pi}{2}s)\Big)
\end{aligned}
$$

As the build-up of asymmetry in the system is a short-time effect, we can neglect any terms that are symmetric with respect to momentum over this period. We therefore attribute the onset of transport solely to the $\sin pb$ dependent terms in the Diffusion Coefficient. We therefore simplify equation 3.6 to:

$$
\begin{aligned}
C(2,p)_{asymm} = \frac{K^2}{6}\Big(& -\sum_s J_{2-2s}((1-b)K) J_s((1-b)2Ka) \sin p_0 b \sin\tfrac{\pi}{2}s \\
& +(2a)^2 \sum_s J_{4-2s}(2(1-b)K) J_s(4(1-b)Ka) \sin 2p_0 b \sin\tfrac{\pi}{2}s \\
& +\sum_s J_{2-2s}((1+b)K) J_s((1+b)2Ka) \sin 2p_0 b \sin\tfrac{\pi}{2}s) \\
& -(2a)^2 \sum_s J_{4-2s}(2(1+b)K) J_s(4(1+b)Ka) \sin 4p_0 b \sin\tfrac{\pi}{2} \\
& -\sum_s J_{2-2s}(K) J_s(2Ka) \sin p_0 b \sin\tfrac{\pi}{2}s \\
& +(2a)^2 \sum_s J_{4-2s}(2K) J_s(4Ka) \sin 2p_0 b \sin\tfrac{\pi}{2}s\Big)
\end{aligned}
\qquad \text{(A44)}
$$

These formulae can now be rearranged to give the total correction to the diffusion coefficient as a function of the three $\sin npb$ present (note that we use $s' = 2 = 2s$ and $s'' = 4 - 2s$

for clarity):

$$C(2,p)_{asymm} = -\frac{K^2}{6}\Big[\sin p_0 b\Big\{\sum_s [J_{s'}(K)J_s(2Ka) + J_{s'}(K(1-b))J_s(2Ka(1-b))]\sin\frac{\pi}{2}s\Big\}$$
$$-\sin 2p_0 b\Big\{(2a)^2\sum_s [J_{s''}(2K)J_s(4Ka) + J_{s'}(K(1+b))J_s(2Ka(1+b)) +$$
$$(2a)^2 J_{s''}(2K(1-b))J_s(4Ka(1-b))]\sin\frac{\pi}{2}s\Big\}$$
$$+\sin 4p_0 b\Big\{(2a)^2\sum_s J_{s''}(2K(1+b))J_s(4Ka(1+b))\sin\frac{\pi}{2}s\Big\}\Big] \quad \text{(A45)}$$

5. Derivation of Ratchet Time t_r

We now come back to the time-dependence of the corrections to the diffusion coefficient, to calculate the ratchet time. When calculating the corrections coming from the $(i,\ i+2)$ correlations, we have neglected the terms like:

$$(J_0(Kb)J_0(Kb2a))^k \quad \text{(A46)}$$

In Eq. A25 if we included these terms we would have:

$$C(2,p)^{i;i+2}_{K\sin x} = -\frac{1}{4N}\sum_s J_{2-2s}((1-b)K)J_s((1-b)2Ka)\cos(p_0 b - \frac{\pi}{2}s)$$
$$\cdot\sum_{k=1}^{k=N/3}(J_0(Kb)J_0(Kb2a))^k \quad \text{(A47)}$$

In the previous sections we assumed $J_0(Kb) \simeq J_0(Kb2a) \simeq 1$ so the sum over k simply yielded a factor of $N/3$. Although $J_0(Kb) \simeq 1 - (Kb)^2/4$ is very close to 1, when the number of kicks (and so, i) increases, this term becomes eventually much smaller than 1. The sum can't then simply be equated to $N/3$. We must sum between kicks N and kick 1 (with only 1 kick over 3 contributing to this correction) :

$$(J_0(Kb)J_0(Kb2a))^N + (J_0(Kb)J_0(Kb2a))^{N-3} + (J_0(Kb)J_0(Kb2a))^{N-6} + \ldots \quad \text{(A48)}$$

This is just a geometrical series, summing up to:

$$\frac{1-(J_0(Kb)J_0(Kb2a))^N}{1-(J_0(Kb)J_0(Kb2a))^3} \quad \text{(A49)}$$

As a function of the kick number N, this increases linearly for small N (and thus gives a correction to the diffusion coefficient), but saturates for large N at the value

$(1-(J_0(Kb)J_0(Kb2a))^3)^{-1}$ (where the diffusion coefficient is not affected by these correlations anymore). Note that for the $\sin 2pb$ and $\sin 4pb$ terms the Bessel functions have arguments two or four times larger respectively. Hence in the main paper we introduce the time dependence function

$$\Phi(N,bK,n)=\frac{3}{N}\frac{1-[J_0(nbK)J_0(2nabK)]^{N-1}}{1-[J_0(bK)J_0(2nabK)]^3} \tag{A50}$$

This multiplies the diffusion rates $C(2,p)$ which were obtained with the approximation $(J_0(Kb)J_0(Kb2a))^k \simeq 1$.

We define the *ratchet time*, t_r, as the time needed for the function $\Phi(N,b,n)N$ to attain 95% of its saturated value as $N \to \infty$. This gives :

$$t_r \simeq \frac{\ln(5/100)}{\ln(J_0(bK)J_0(2abK))} \tag{A51}$$

Keeping only the lowest order in b, we get :

$$t_r = \frac{4\ln(20)}{b^2K_{eff}^2} \tag{A52}$$

where we recall $K_{eff}^2 = K^2(1+4a^2)$. Note that this is the ratchet time for the dominant $\sin pb$ contribution to the diffusion coefficient. One can calculate in the same way the ratchet times for the $\sin 2pb$ and $\sin 4pb$ contributions. For $a = 1/2$ we get :

$$t_r^{(\sin pb)} = \frac{2\ln(20)}{(Kb)^2} \tag{A53}$$

$$t_r^{(\sin 2pb)} = \frac{2\ln(20)}{(2Kb)^2} \tag{A54}$$

$$t_r^{(\sin 4pb)} = \frac{2\ln(20)}{(4Kb)^2} \tag{A55}$$

---

[1] G. Casati, B.V. Chirikov, Izraelev F.M., and J. Ford in "Lecture notes in Physics", Springer, Berlin **93** , 334 (1979).

[2] S. Fishman, D.R. Grempel, R.E. Prange, Phys. Rev. Lett. **49**, 509 (1982).

[3] F.L. Moore, J.C. Robinson, C.F. Bharucha, Bala Sundaram, and M.G.Raizen, Phys. Rev. Lett. **75**, 4598 (1995).

[4] P. Reimann, Phys.Rep.**361**,57 (2002).

[5] S. Flach, O. Yevtushenko, Y. Zolotaryuk, Phys. Rev. Lett. **84**, 2358 (2000). S.Denisov, S. Flach, A. A. Ovchinnikov, O. Yevtushenko, Y. Zolotaryuk, Phys. Rev. E **66**, 041104 (2002).

[6] T. Dittrich, R. Ketzmerick, M.-F.Otto, and H. Schanz, Ann. Phys. (Leipzig) **9**,1 (2000); H. Schanz, M.-F.Otto, R. Ketzmerick T. Dittrich, Phys. Rev. Lett. **87**, 070601 (2001).

[7] T.S. Monteiro, P. A. Dando, N. A. C. Hutchings and M. R. Isherwood, Phys. Rev. Lett **89**, 194102 (2002).

[8] T. Jonckheere, M. R. Isherwood and T. S. Monteiro, Phys. Rev. Lett. **91**, 253003 (2003).

[9] P.H.Jones, M.Goonasekera, H.E. Saunders-Singer and D.Meacher *quant-phys/0309149*

[10] A.J. Lichtenberg and M.A. Lieberman, 'Regular and Chaotic Dynamics', Springer-Verlag, New York (1992).

[11] D. Ł. Shepelyansky Phys. Rev. Lett. **56**, 577 (1986).

[12] A. B. Rechester and R. B. White, Phys. Rev. Lett. **44**, 1586 (1980).

[13] Matthew Isherwood, PhD thesis, UCL (2004).

Bibliography

[1] E. Ott, Chaos in Dynamical Systems, Cambridge University Press, (1993).

[2] B.V. Chirikov, Phys. Rep. **52** 263 (1979).

[3] G. Casati, B.V. Chirikov, Izraelev F.M., and J. Ford in *Lecture notes in Physics*, Springer, Berlin **93** , 334 (1979).

[4] R. Blümel in *Chaos in Atomic Physics*, Springer, Berlin **93** , 334 (1979).

[5] S. Fishman, D.R. Grempel, R.E. Prange, Phys. Rev. Lett. **49**, 509 (1982).

[6] D.R. Grempel, S. Fishman, R.E. Prange, Phys. Rev. Lett. **49**, 833 (1982).

[7] Baruch Fischer, A. Rosen, A. Bekker and S. Fishman, Physics Review. E. **61**, 4694 (2000).

[8] S.Wimberger, I. Guarneri and S. FIshman, preprint, Physics/0012013, Dec 7, 2000.

[9] I.H. Deutsch, J. Grondalski and P.M. Alsing Physics Review. E. **56**, 1705 (1997).

[10] G. Schmidt, J.Bialek, Physica D **5**, 397 (1982).

[11] F.L. Moore, J.C. Robinson, C.F. Bharucha, Bala Sundaram, and M.G.Raizen, Phys. Rev. Lett. **75**, 4598 (1995).

[12] M.G. Raizen, J.Koga, B, Sundaram, Y. Kishimoto, H. Takuma and T.Tajima, Physics Review A **58**, 4757 (1998).

[13] J.C. Robinson, C.F. Bharucha, F.L. Moore, R.Jahnke, G.A. Georgakis, Q.Nui and M.G.Raizen, Phys. Rev. Lett. **74**, 3963 (1995).

[14] B.G. Klappauf, W.H. Oskay, D.A. Steck and M.G.Raizen, Phys. Rev. Lett. **81**, 1203 (1998).

[15] F.L. Moore, J.C. Robinson, C.F. Bharucha, Bala Sundaram, and M.G.Raizen, Quantum Semiclass. Opt. **8**, 687 (1996).

[16] B.G. Klappauf, W.H. Oskay, D.A. Steck, and M.G.Raizen, Phys. Rev. Lett. **81**, 4044 (1998).

[17] C.F. Bharucha, K.W. Madison, P.R. Morrow, S.R. Wilkinson, Bala Sundaram, and M.G.Raizen, Physical Review A. **55**, 857 (1997).

[18] K.W. Madison, M.C. Fisher, R.B. Diener, Q.Niu and M.G.Raizen, Phys. Rev. Lett. **81**, 5093 (1998).

[19] J.Zhong, R.B. Diener, D.A. Steck, W.H. Oskey, M.G.Raizen, E. Ward Plummer, Z. Zhang and Q.Niu, Phys. Rev. Lett. **86**, 2485 (2001).

[20] M.Beinert, F. Haug, W.P.Schleich and M.G. Raizen, Phys. Rev. Lett. **89**, 050402-1 (2002).

[21] C.F. Bharucha, F.L. Moore, J.C. Robinson, Bala Sundaram, Q. Niu and M.G.Raizen, Physics Review. E. **60**, 3881 (1999).

[22] V.Milner, D.A. Steck, W.H. Oskay and M.G.Raizen, Physics Review. E. **61**, 7223 (2000).

[23] D.A. Steck, V.Milner, W.H. Oskay and M.G.Raizen, Physics Review. E. **62**, 3461 (2000).

[24] F.L. Moore, J.C. Robinson, C.F. Bharucha, P.E. Williams and M.G.Raizen, Phys. Rev. Lett. **73**, 2974 (1994).

[25] P.J. Bardoff, I.Bialynicki-Birula, D.S.Krähmer, G.Kurizki, E.Mayr, P. Stifter and W.P. Schleich, Phys. Rev. Lett. **74**, 3959 (1995).

[26] R. B. Diener, G. A. Georgakis, Jianxin Zhong, M.G.Raizen, Qian Niu, Physical Review A. **64**, 033416-1 (2001).

[27] T.S. Monteiro, S.M. Owen and D.S. Saraga, The Royal Society **357**, 1359 (1999).

[28] D.R. Meacher, Contempory Physics. **39**, 329 (1998).

[29] L. Guidoni and P. Verkerk, J.Opt. B: Quantum Semiclass. **1**, R23 (1999).

[30] Shmuel Fishman, Lecture notes of the Scottish Summer School (1994).

[31] P.S. Jessen and I.H. Deutsch, Advances in Atomic, Molecular and Optical Physics. **37**, (1996).

[32] I.H. Deutsch, P.M. Alsing, J. Grondalski, S. Ghose, D. Laycock and P.S. Jessen, J.Opt. B: Quantum Semiclasss. Opt. **2**, 633, (2000).

[33] Homer, *The Odyssey*, Book xI, Book of the Dead, Penguin Books Inc., Hamonsworth, Middlesex. (1959).

[34] C. Mennerat-Robilliard, D. Lucas, S.Guibal et al, Phys. Rev. Lett. **82**, 851 (1999).

[35] T.S. Monteiro, Contemporary Physics. **35**, 311 (1994).

[36] Giulio Casati, Chaos. **6**, 391 (1996).

[37] F.Julicher, A. Adjari and J.Prost, Rev. Mod. Phys., **69**, 1269 (1997).

[38] J.L. Mateos Phys. Rev. Lett. **84**, 258 (1999).

[39] P. Reimann, Phys. Rep. **361**,57 (2002).

[40] P. Reimann, M. Grifoni, and P. Hänggi, Phys. Rev. Lett. **79**, 10 (1997).

[41] P. Reimann, Phys. Rev. Lett. **86**, 4992 (2001).

[42] R. Eichhorn, P. Reimann, and P. Hänggi, Phys. Rev. Lett. **88**, 190601-1 (2002).

[43] R. Bartussek, P. Reimann, and P. Hänggi, Phys. Rev. Lett. **76**, 1166 (1996).

[44] P. Reimann, C. Van den Broeck, H. Linke, P. Hänggi, J.M. Rubi and A. Perez-Madrid Phys. Rev. Lett. **87**, 010602-1 (2001).

[45] P. Hänggi, P. Reimann, Phys. World, **21** 12 (1999).

[46] T. R. Kelly, I. Tellitu, J. P. Sestelo, J. Org. Chem. **63** 3655 (1998).

[47] M. Brooks, Quantum Clockwork, New Scientist **29** 2222 (2000).

[48] M. V. Berry, N. L. Balazs, M. Tabor and A. Voros, Annals of Physics, **122** 26 (1979).

[49] P. Reimann and P. Hänggi, Chaos, **8**, 629 (1998).

[50] R. D. Astumian, Science, **276**, 917 (1997).

[51] R. D. Astumian and M. Bier, Phys. Rev. Lett. **72** 1766 (1994).

[52] S. Flach, O. Yevtushenko, Y. Zolotaryuk, Phys. Rev. Lett. **84**, 2358 (2000).

[53] T. Dittrich, R. Ketzmerick, M.-F.Otto, and H. Schanz, Ann. Phys. (Leipzig) **9**,1 (2000).

[54] H. Schanz, M.-F.Otto, R. Ketzmerick T. Dittrich, Phys. Rev. Lett. **87**, 070601 (2001).

[55] T. Cheon, P. Exner, P. Seba, preprint, cond-mat/0203241, 12 March 2002.

[56] N. Hutchings *et al*, in preparation.

[57] M Oberthaler, M.B.d'Arcy, R M Godun, G S Summy and K. Burnett. Phys. Rev. Lett. **83**, 4447 (1999).

[58] M.B.d'Arcy, R M Godun, M Oberthaler, D Cassetari, and G S Summy. Phys. Rev. Lett. **87**, 741021 (2001).

[59] R M Godun, M.B.d'Arcy, M Oberthaler and G S Summy, Physics Review A. **62**, 013411-1(2000).

[60] M.B.d'Arcy, R M Godun, M Oberthaler, G S Summy, K. Burnett and S. A. Gardiner. Physics Review E. **64**, 056233-1 (2001).

[61] S. Schlank, M.B.d'Arcy, R M Godun, D Cassetari, and G S Summy, Phys. Rev. Lett. **90**, 054101 (2003).

[62] A.J. Lichtenberg and M.A. Lieberman, *Regular and Chaotic Dynamics*, Springer-Verlag, New York (1992).

[63] D. Ł. Shepelyansky Phys. Rev. Lett. **56**, 577 (1986).

[64] L.A. Caron, H. Króger, X.Q. Luo, G. Melkonyan and K.J.M Moriarty, preprint, Physics/0203022, March 5,2002.

[65] M.Latka and B.J. West, Phys. Rev. Lett. **75**, 4202 (1995).

[66] R. Graham, M. Schlautmann and P.Zoller, Physics Review A, **45**, 1, (1992)

[67] D.A. Steck, Atomic Motion in a Standing Wave of Far-Detuned Light, Lecture Notes (1998).

[68] D.A. Steck, Lecture Notes for Los Alamos Summer School (2002).

[69] T. Jonckheere, M.R. Isherwood and T.S. Monteiro, preprint, Physics/0304036v1, April 17, 2003.

[70] R. Ketzmerick, K.Kruse, T.Geisel, Physica D. **131**, 247 (1999).

[71] A. I. Saichev and G.M. Zaslavsky, Chaos **7**, 753 (1997).

[72] J. Gong and P. Brumer, Journal of Chemical Physics **115**, 3590 (2001).

[73] L. P. Faucheux, L. S. Bourdieu, P. D. Kaplan and A. J. Libchaber, Phys. Rev. Lett.**74** 1504 (1995).

[74] A.B. Rechester and R.B White, Phys. Rev. Lett. **44**, 1586 (1980).

[75] A.B. Rechester, M.N. Rosenbluth and R.B White, Physiscs Review. A. **23**, 2664 (1981).

[76] J.M. Greene, J. Math Physics **20**, 1183 (1979).

[77] J.C.A. Barata and D.A. Cortez, preprint, Physics/0201008, Jan 3, 2001.

[78] R. del Rio, S. Jitomirskaya, Y. Last and B. Simon, Phys. Rev. Lett. **75**, 117 (1995).

[79] A. Mouchet, C. Miniature, R. Kaiser, B. Gremaud and D. Delande, preprint, Physics/0012013, Dec 7, 2000.

[80] S. Kohler, R. Utermann, P. Hánggi and T.Dittrich, Physics Review. E. **58**, 7219 (1998).

[81] C. Mennerat-Robilliard, D. Lucas, S. Guibal, J. Tabosa, C. Jurczak, J. Courtois and G. Grynberg, Phys. Rev. Lett. **82**, 851 (1999).

[82] F. Falo, P. J. Martinez, J. J. Mazo and S. Cilla, Europhys. Lett., **45** 700 (1999).

[83] P.Jung, J. G. Kissner and P. Hänggi, Phys. Rev. Lett. **76**, 3436 (1996).

[84] M. Bier, Contemporary Physics. **38**, 371 (1997).

[85] J. Maddox, Nature. **365** 203 (1993).

[86] J. Maddox, Nature. **368** 287 (1994).

[87] J. Maddox, Nature. **369** 181 (1994).

[88] S. Leibler, Nature. **370** 412 (1994).

[89] J. Spudich, Nature. **372** 515 (1994).

[90] H. Linke, Science **299** 841 (2003).

[91] H.Linke, Appl. Phys. A. **2** 75 (2002).

[92] T. E. Humphrey, R. Newbury, R. P. Taylor and H. Linke, Phys. Rev. Lett. **89** 116801 (2002).

[93] H. Linke, T. E. Humphrey, P. E. Lindelof, A. Löfgren, R. Newbury, P. Omling, A. O. Sushkov, R. P. Taylor, Hongqi Xu, Appl. Phys. A. **74** 237 (2002).

[94] H. Linke, T. E. Humphrey, R. P. Taylor, R. Newbury, Physica Scripta, **T90** 54 (2001).

[95] H. Linke, T. E. Humphrey, A. Löfgren, R. Newbury, P. Omling, A. O. Sushkov, R. P. Taylor, Science **286** 2314 (1999).

[96] H. Linke, W. Sheng, P. E. Lindelof, A. Löfgren, P. Omling, Hongqi Xu, Europhys. Lett. **44** 341 (1998).

[97] P. Hänggi, I. Goychuk, Stochastic Processes in Physics, Chemistry and Biology, Lecture notes in Physics, Springer, Berlin, (2002).

[98] Z. Farkas, PhD dissertation in Physics, Eötvös University, Hungary, (2001).

[99] A. Riegler, Cybernetics and Systems, **32** 411 (2001).

[100] S.Scheidl, V. M Vinokur, Physics Review B, **65** 195305-1 (2002).

[101] M. O. Magnasco and G. Stolovitzky, Journal of Statistical Physics, **93** 615 (1998).

[102] M. O. Magnasco, Phys. Rev. Lett., **71** 1477 (1993).

[103] J. Lehmann, S. Kohler, P. Hänggi and A. Nitzan, Phys. Rev. Lett. **88** 228305-1 (2002).

[104] C. S. Lee, B. Janko, I. Derenyl and A. L. Barabasl, Nature, **400** 337 (1999).

[105] M. Abramowitz and I. A. Stegun, Handbook of Mathematical Functions: with formulas graphs and mathematical tables, Constable, London, (1965).

[106] R. Feynman, R. B. Leighton and M.Sands, The Feynman Lectures in Physics, 1 44-46, Addison-Wesley Publishing Company, Inc., London (1963).

[107] C. Cohen-Tannoudji, B. Dui and F. Laloë, Quantum Mechanics, Whiley, New York (1977).

[108] W. H. Press et al., Numerical Recipes in FORTRAN: the art of scientific computing, Cambridge University Press, (1992).

[109] W. D. Heiss, Chaos and Quantum Chaos, Springer-Verlag, London, (1992).

[110] M.C. Gutzwiller, Chaos in classical and quantum mechanics, Springer-Verlag, London (1990).

[111] T. S. Monteiro, P. A. Dando, N. A. C. Hutchings, M.R. Isherwood, Phys. Rev. Lett. **88** 228305-1 (2002).

[112] P. H. Jones, M. Goonasekera, H. E. Saunders-Singer and D. R. Meacher, Preprint, arXiViquant-ph/0309149. (2003).

[113] E. A. Hinds, C. J. Vale and M. G. Boshier, Phys, Rev, Lett, 86, 1462 (2001).

[114] W. Hänsel, P. Hommelhoff, T. W. Hänsch and J. Reichel, Nature 413, 498 (2001).